UNIVERSITY OF WEST BOHEMIA
FACULTY OF MECHANICAL ENGINEERING

Study programme: Theory and Construction of Machines (P0715D270024)

DISSERTATION THESIS

Analysis of Flow Induced Instabilities in a Centrifugal Compressor
Stage with Radial Inlet Guide Vanes

Author: **Ing. Lukáš HURDA**
Supervisor: **Ing. Richard Matas, Ph.D.**

Academic year 2022/2023

Prohlášení o autorství

Předkládám tímto k posouzení a obhajobě disertační práci zpracovanou na závěr studia na Fakultě strojní Západočeské univerzity v Plzni.

Prohlašuji, že jsem tuto disertační práci vypracoval samostatně, s použitím odborné literatury a pramenů uvedených v seznamu, který je součástí této disertační práce.

V Plzni dne 31. srpna 2023.

Declaration of authorship

I hereby submit for examination and defence my dissertation prepared at the end of my studies at the Faculty of Mechanical Engineering of the University of West Bohemia in Pilsen.

I declare that I have prepared this dissertation independently, using the literature and sources listed in the list that is part of this dissertation.

Date: 31st August 2023.

Acknowledgements

I am grateful to my colleagues at the New Technologies - Research Centre, who have not only given me the freedom to complete this thesis but substantially helped along the way of its creation. Their inspiring knowledge, willingness and patience are invaluable to me. Special thanks are deserved for providing the computational resources at the Orfeus and Viper compute clusters.

I thank Richard Matas for being my supervisor, colleague, mentor and a friend for all his care and advice, which has never been limited to the thesis, studies, or research work only.

I am expressing my gratitude for the permission of Howden ČKD to use the measurement data and other relevant knowledge.

I value the support provided by the staff of the Department of Power Systems Engineering and the entire Faculty of Mechanical Engineering.

I thank my sister for her bold and prompt solutions to problems I did not know existed.

Last but not least, I express my gratitude to my beloved life partner Magdalena, who does not ever cease to support me, trust me, believe in me, and fuel my passions whether these are common to both of us or not. I am incredibly happy and honoured to be a part of her life.

ANOTACE DISERTAČNÍ PRÁCE

Akademický rok odevzdání: 2022/2023.

AUTOR	*Příjmení (včetně titulů)*		*Jméno*
	Ing. Hurda		Lukáš
STUDIJNÍ PROGRAM	P0715D270024 – Teorie a stavba strojů		
VEDOUCÍ PRÁCE	*Příjmení (včetně titulů)*		*Jméno*
	Ing. Matas, Ph.D.		*Richard*
PRACOVIŠTĚ VEDOUCÍHO	Katedra energetických stojů a zařízení		
NÁZEV PRÁCE	Analýza proudových nestabilit ve stupni odstředivého kompresoru s radiálními naváděcími lopatkami		

Počet stránek (A4 a ekvivalentů A4)

Celkem	132		Textová část	128		Grafická část (přílohy)	4

STRUČNÝ POPIS ZAMĚŘENÍ, TÉMA, CÍL POZNATKY A PŘÍNOSY	Je rozebráno nestandartní chování odstředivého kompresoru vybaveného radiálními naváděcími lopatkami při měření na vývojové zkušebně. Problém je identifikován a popsán pomocí podrobného vyhodnocení měřených dat, rozměrové analýzy, výpočtů středního proudu a následného matematického modelování proudění. Je sestaven univerzální program pro vyhodnocení měření uvažující chování reálných plynů. Odtržení mezní vrstvy ve vstupním kanálu způsobeného odstředivými silami v rotujícím proudu tekutiny a jeho vliv na provoz kompresorů je popsáno zobecněným způsobem. Provedené parametrické studie mají také za cíl zobecnění poznatků. CFD výpočty na zjednodušených modelech i geometriích skutečných strojů pomáhají prokázat a upřesnit dosažené výsledky. Závěrem jsou vyvozena doporučení pro návrh stupňů odolnějších nestabilitám ve vstupním kanále včetně realizace a CFD výpočtů na modifikovaném oběžném kole kompresoru s integrovaným záběrníkem.
KLÍČOVÁ SLOVA	Proudové stroje, odstředivé kompresory, naváděcí lopatky, vyhodnocení měření, rozměrová analýza, parametrická studie, výpočetní mechanika tekutin, CFD, nenávrhové režimy, návrh proudového stroje

DISSERATATION THESIS ANNOTATION

Academic year of submission: 2022/2023.

AUTOR	*Příjmení (včetně titulů)*		*Jméno*
	Ing. Hurda		Lukáš
STUDIJNÍ PROGRAM	P0715D270024 – Theory and Construction of Machines		
VEDOUCÍ PRÁCE	*Příjmení (včetně titulů)*		*Jméno*
	Ing. Matas, Ph.D.		*Richard*
PRACOVIŠTĚ VEDOUCÍHO	Department of Power Machines and Equipment		
NÁZEV PRÁCE	Analysis of Flow Induced Instabilities in a Centrifugal Compressor Stage with Radial Inlet Guide Vanes		

Numer of pages (A4 format and the equivalents of it)

Total	132		**Text part**	128		**Graphical part ()**	4

BRIEF DESCRIPTION OF THE TOPIC, FINDINGS AND CONTRI-BUTIONS	The non-standard behaviour of a centrifugal compressor equipped with inlet radial guide vanes during measurements on a development test bench is discussed. The problem is identified and described by means of a detailed evaluation of measurement data, dimensional analysis, mean flow calculations and mathematical modelling of the flow. A general-purpose program for the evaluation of measurements considering the real gas behaviour is written. Boundary layer detachment in the inlet channel caused by centrifugal forces in the rotating fluid flow and its effect on compressor operation is described in a generalized manner. Parametric studies are also performed to generalize the findings. CFD calculations on simplified models and geometries of real machines help to prove and refine the results obtained. Recommendations for the design of stages more resistant to instabilities in the inlet channel are derived, including the implementation and CFD calculations of a modified compressor impeller with an integrated inducer.
KEYWORDS	Turbomachinery, centrifugal compressors, inlet guide vanes, measurement evaluation, dimensional analysis, parametric study, computational fluid dynamics (CFD), off-design conditions, tubomachinery design

Contents

List of Figures

9

List of Tables

Nomenclature

A	Flow area	$\mathrm{m^2}$
C	Power law regression dimensionless coefficient	1
D	Diameter	m
F_2	Turbulence model blending function	1
F_r	Total temperature probe restitution factor	1
G	Mass flow rate	$\mathrm{kg\,s^{-1}}$
M	Gas molar weight	$\mathrm{kg\,mol^{-1}}$
N	Power	$\mathrm{J\,s^{-1} = kg\,m^2\,s^{-3}}$
Q	Volumetric flow rate	$\mathrm{m^3\,s^{-1}}$
R	Universal gas constant	$8.3145\,\mathrm{J\,kg^{-1}\,K^{-1}}$
S	Invariant measure of the strain rate tensor	$\mathrm{s^{-1}}$
S_{ij}	Strain rate tensor	$\mathrm{s^{-1}}$
T	Temperature	K
X	Normalized meridional curvilinear coordinate	m
Y	Normalized transversal curvilinear coordinate	m
a	Sonic speed (speed of sound)	$\mathrm{m\,s^{-1}}$
a_1	Turbulence model calibration constant	1
b	Channel width	m
c	Flow absolute speed	$\mathrm{m\,s^{-1}}$
c_V	Volume fraction	1
c_h, c_ρ	Abs. flow velocity from total-to-static enthalpy/density	$\mathrm{m\,s^{-1}}$
c_p	Isobaric specific heat capacity	$\mathrm{J\,kg^{-1}\,K^{-1} = m^2\,s^{-2}\,K^{-1}}$
c_v	Isochoric specific heat capacity	$\mathrm{J\,kg^{-1}\,K^{-1} = m^2\,s^{-2}\,K^{-1}}$
$e_{1,2,3}$	Power law regression exponents	1
f_i	External volumetric forces	$\mathrm{N\,kg^{-1} = m\,s^{-2}}$
h	Specific enthalpy	$\mathrm{J\,kg^{-1} = m^2\,s^{-2}}$
h'	Specific enthalpy fluctuation	$\mathrm{J\,kg^{-1} = m^2\,s^{-2}}$
i	Angle of incidence	rad
k	Specific turbulent kinetic energy	$\mathrm{J\,kg^{-1} = m^2\,s^{-2}}$
n	Polytropic exponent	1
n'	Coefficient of radial elongations	1
p	Pressure	$\mathrm{Pa = kg\,m^{-1}\,s^{-2}}$

p_{pV}	Partial pressure of water vapour	$\mathrm{Pa} = \mathrm{kg\,m^{-1}\,s^{-2}}$
p_{sat}	Saturation pressure of water vapour	$\mathrm{Pa} = \mathrm{kg\,m^{-1}\,s^{-2}}$
r	Specific gas constant	$\mathrm{J\,kg^{-1}\,K^{-1}} = \mathrm{m^2\,s^{-2}\,K^{-1}}$
r_a	Simplified channel axial bend radius	m
r_m	Station mean radius	m
r_p	IGVs pivot pitch circle radius	m
r_t	Simplified channel tangential bend radius	m
t	Time	s
u	Impeller circumferential speed	$\mathrm{m\,s^{-1}}$
v	Flow velocity	$\mathrm{m\,s^{-1}}$
v'	Flow velocity fluctuation	$\mathrm{m\,s^{-1}}$
w	Flow speed relative to impeller	$\mathrm{m\,s^{-1}}$
x	Cartesian system spatial coordinates (indexed)	m
Θ	Cylindrical coordinate - angle	rad
Ω	Angular speed of rotation	rad/s
α	Absolute flow angle	rad
α'	Blade/vane metal angle in an absolute frame of reference	rad
β	Flow angle relative to impeller	rad
γ	Transverse angle of local flow velocity	rad
δ	Flow deviation angle	rad
δ_{ij}	Kroenecker unity tensor	1
ε	Turbulent dissipation rate	$\mathrm{J\,kg^{-1}\,s^{-1}} = \mathrm{m^2\,s^{-3}}$
ζ	Local wall normal distance	m
ϑ	Inlet guide vanes stagger angle	rad
λ	Thermal conductivity	$\mathrm{J\,m^{-1}\,s^{-1}\,K^{-1}} = \mathrm{kg\,m^{-1}\,s^{-3}\,K^{-1}}$
μ	Dynamic viscosity	$\mathrm{Pa\,s} = \mathrm{kg\,m^{-1}\,s^{-1}}$
ν	Kinematic viscosity	$\mathrm{m^2\,s^{-1}}$
ξ	Pressure loss coefficient	1
ρ	Gas density (specific weight)	$\mathrm{kg\,m^{-3}}$
τ_{ij}^t	Reynolds turbulent stress tensor	$\mathrm{m^2\,s^{-2}}$
τ_w	Wall shear stress	$\mathrm{Pa} = \mathrm{kg\,m^{-1}\,s^{-2}}$
τ_{ij}	Shear stress tensor	$\mathrm{Pa} = \mathrm{kg\,m^{-1}\,s^{-2}}$
φ	Gas relative humidity	1
ω	Turbulent specific dissipation rate	$\mathrm{s^{-1}}$

Dimensionless Numbers

Ce	Centrifugal force criterion
C_f	Coefficient of friction
C_p	Coefficient of pressure

I	Turbulence intensity
Ma	Mach number
Pr	Prandtl number
Re	Reynolds number
R_a	Geometric simplex for the simplified channel axial bend
R_t	Geometric simplex for the simplified channel tangential bend
Sh	Strouhal number
f_{corr}	Schultz polytropic correction factor
y^+	Boundary-layer-normalized dimensionless distance from a wall
η	Thermodynamic efficiency
κ	Ratio of specific heats, i.e. adiabatic exponent
Φ	Flow coefficient
Ψ	Power/loading coefficient

Subscripts and modifiers

$\bar{\bullet}$	Reynolds-averaged variable
$\tilde{\bullet}$	Favre-averaged (mass-weighted averaged) variable
0	Station upstream of IGVs
$0b$	Station downstream of IGVs
$0c$	Station in the inlet channel bend apex
1	Station at rotor leading edge
2	Station at rotor trailing edge
3	Station at diffuser inlet
4	Station at diffuser outlet
5	Station at de-swirl channel inlet
6	Station at de-swirl channel outlet
7	Station at stage outlet
D	Discharge
I	Inlet/intake
LE	Leading edge
N	Normalized
O	Outlet
TE	Trailing edge
c	Corrected for rotational speed discrepancy
d	Dynamic (gas state parameter)
i	Cartesian coordinate index
id	Ideal polytropic
ise	Isentropic
j, k	Summation indices

m	Measured quantity or meridional direction/component
nom	Nominal
pol	Polythropic
r	Rescaled by intake state and machine size
s	Static (gas state parameter) or spanwise (i.e. transverse) direction/component
t	Total, turbulent or tangential direction/component

Abbreviations

2D, 3D	Two or three dimensional
AC	Alternating current
BC(s)	Boundary condition(s)
BWR	Benedict-Webb-Rubin equation of state for real gases
CFD	Computational fluid dynamics
ČKD	Českomoravská Kolben-Daněk (Czech machinery producer brand)
ČSN EN ISO	Harmonized Czech-European-International technical standard
EoS	Equation of state
GGI/GTI	Generalized grid/turbo interface
IGV(s)	Inlet guide vane(s)
LES	Large eddy simulation
MRF	Moving reference frame
NACA	National Advisory Committee for Aeronautics
NTC	New Technologies - Research Centre (of UWB)
PDE(s)	Partial differential equation(s)
R&D	Research and development
RANS	Reynolds-averaged Navier-Stokes equations
RSM	Reynolds stress model
SST	Shear stress transport
TMF	Target mass flow rate, normalized
UWB	University of West Bohemia
$v2\text{-}f$	Turbulent viscosity 2-equation model with anisotropy measure

1   Introduction

Turbomachines are the driving force of human society, even though they are often invisible to many. Along with positive displacement machines, they carry out one of the most important and challenging energy conversions possible - the conversion of heat to the energy of motion. But besides the production of so-called primary energy, they also act on the side of its consumption. Compressors, pumps, boosters, blowers and fans enable us to move and/or pressurize whatever fluid we want. Speaking of almost any field of human activity, the processes where energized fluid is necessary are countless and it would be rather hard to find one that does *not* need it.

Even throughout history, a moving fluid was the pillar on which civilizations were built. Earlier only natural forces were utilized wherever it was possible, so settlements arose where a sustained supply of fresh water for irrigation was present. Later wind and water mills or forging hammers were built as the distant ancestors of modern day powerhouses. That was at the time when humanity had already tamed heat and light in the form of fire, which was easily portable. It took centuries to be able to provide a similar portability to the energy of motion. Electricity and utilization of pipelines and pressure vessels of all types enabled this.

Since we can transport energy almost anywhere we need it, energy consuming appliances including turbomachines can be found everywhere. Such machines are therefore designed and manufactured in all sizes imaginable, each with a different purpose and with different goals. In the larger ones, the design is all about the balance between robustness and efficiency, while the demand for the lowest possible cost of the machine is omnipresent, of course. In the field of energy consuming turbomachinery, one phenomenon stands against all of these desires - the need to make the fluid flow in the direction of increasing pressure. Transacting motion from solid parts to fluid has more degrees of freedom and is much more unstable than the opposite process taking place in turbines.

1.1   Motivation

Centrifugal compressors are commonly used in a wide range of industrial applications where high volume and high compression of gases is required. They fit between low-flow high-compression positive displacement compressors and high-flow low-compression axial turbocompressors.

Some common applications of centrifugal compressors include:

- Gas turbines in power generation or aerospace propulsion (mid to low scale power generation and low speed jet aircrafts and turboprops; often in combination with preceding axial stages)

- Refrigeration and air conditioning systems

- Petrochemical and chemical plants for compressing and transporting gases (ranging in molecular weight between hydrogen or helium to natural gas and more complex organic compounds and mixtures)

- Compressed air systems for industrial and manufacturing processes (high flow rate applications)

- Gas pipelines for transporting natural gas over long distances

Applications where there are large variations in the flow rates or pressures of the gas being compressed are quite common. One of the reasons for this kind of robustness is that centrifugal force drives the fluid in the right direction even in the most unfavourable aerodynamic conditions inside the machine. There are multiple ways to achieve control of the compressor output. The most widely used methods include discharge throttling, variable rotational speed control or adjustable inlet guide vanes (IGVs). Although these are often combined for efficient, reliable, and responsive control systems, they have their own advantages and disadvantages.

Adjustable IGVs work by altering the angle of the vanes at the inlet of the compressor, which affects the energy transfer process in the impeller. This effectively reduces power consumption at the same rotational speed rather than waste it in the discharge throttle valve. In addition, IGV control is often faster and more responsive than variable speed control, which can take longer to adjust to the changes in the process demand. However, it should be noted that variable speed control can provide a wider range of control and can be more precise in certain applications. Modern power electronics are required for speed control of AC power driven machines. For a multistage machine, often only the first stage needs to be equipped with a rather complex mechanism of IGVs.

The vanes have two possible types of arrangement:

- Axial - commonly used in single stage machines, possibly with an overhang rotor and open air intake from the atmosphere.

- Radial - with centripetal flow through vanes, which later reaches the channel bend to an axial direction to enter the impeller. Indisputably proficient for single-shaft multistage machines with complex rotor dynamics and large dimensions of high pressure casings, where the shortest possible total shaft length is desirable. Despite the advantages, in many cases designers choose to avoid it without a clear documentation of the reason.

The superiority of the radial IGV arrangement in the context of the whole machine architecture drives efforts to achieve stable and reliable operation of such a control system.

University of West Bohemia, Faculty of Mech. Engineering   Dissertation thesis 2022/23

Department of Power Systems Engineering   Ing. Lukáš Hurda

The problems of such a system described in the following section are the main motivation for the research carried out in this thesis.

1.2   Problem description

The author was confronted with a specific adverse phenomenon occurring during measurement on a centrifugal compressor development test bed. This test bed constituted a single stage centrifugal compressor, where the impeller and channel walls could be completely replaced while keeping the electric drive and transmission, compressor outer casing parts and all the other equipment. This facility was set to determine the operational characteristics of a newly developed family of stages designated for multi-stage industrial compressors - or rather to confirm the expectations of the design process and CFD analyses while providing physical verification. This is why it had featured a radial (centripetal) inlet channel and a return channel equipped with de-swirl vanes in spite of being a single stage machine.
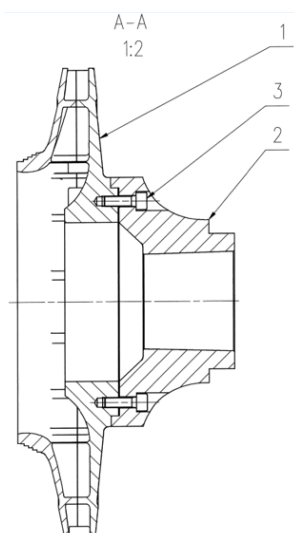
Figure 1.1: 1- Low-to-mid flow capacity prismatic blade brazed impeller of the "s4" stage. (2- impeller carrier, 3- bolts).
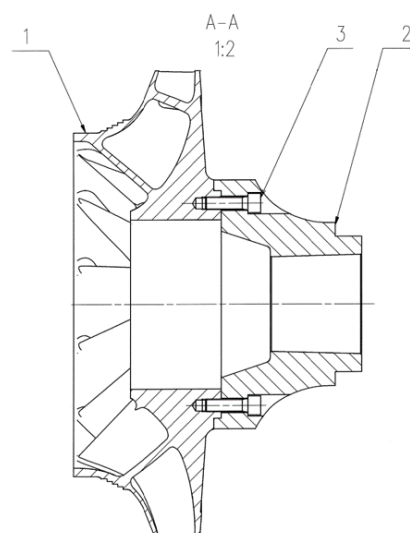
Figure 1.2: 1- High flow capacity 3D blade impeller of the "s2" stage, machined in one piece. (2- impeller carrier, 3- bolts).

All of the analysed stages shared an identical impeller outer diameter and they were developed for a wide range of flow capacity. All the impellers were designed as shrouded, so the low flow capacity stages with shorter blade span needed to be machined in two parts and then joined by welding or brazing, unlike high capacity impellers, which can be machined in one piece.

The low capacity stages have a quite specific design altogether. They have prismatic blades and the rotor blade row inlet is purely radial. The axial length of the impeller is as
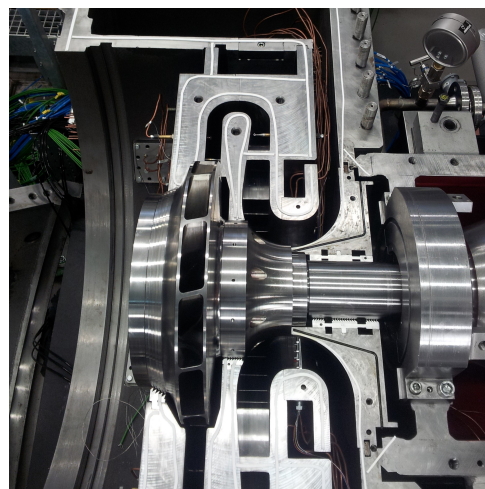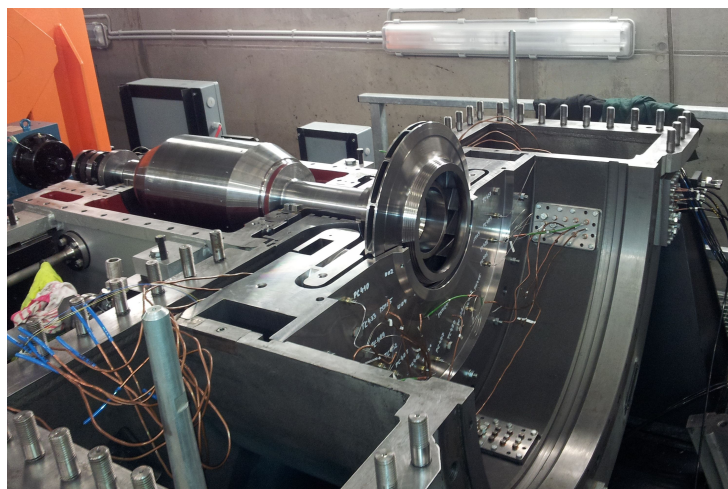
Figure 1.3: Photo of the "u4" stage (slightly narrower version of "s4") during assembly at the test bed.

Figure 1.4: Photo of the "s2" stage during assembly at the test bed.

short as possible, making the channel turns rather sharp. A detailed description is given in section 2.2.

After testing the individual stages with axial impeller intake flow, radial inlet guide vanes (IGVs) were mounted. For some of the tested stages, excessive noise and performance loss occurred at certain operating conditions. These were caused by an unstable flow in the stage during conditions far from both surge and choke limits. The mass flow rate set by the discharge throttling control system was still more or less predictable, but large drops in discharge pressure occurred during a traverse over the speedline. The pressure drop diminished after a large mass flow rate change, but reversing the traverse direction showed significant hysteresis. An example is given in Figure 1.5.
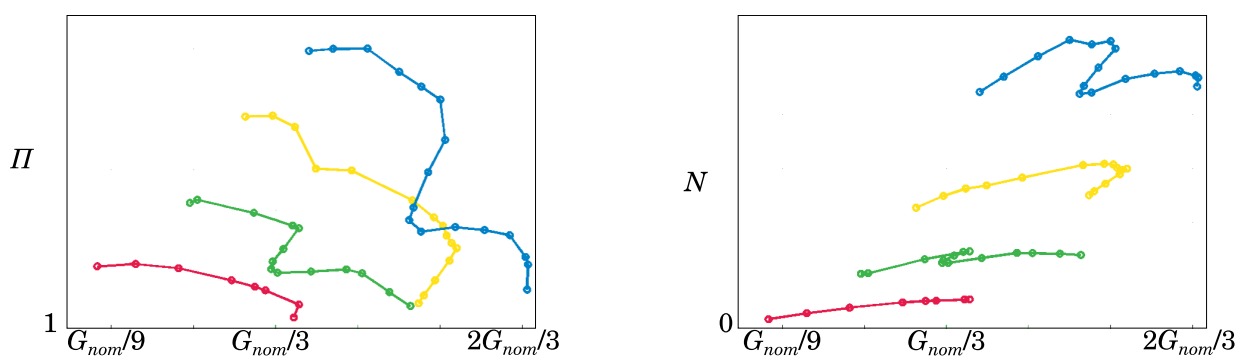
Figure 1.5: An example of measured defective pressure ratio (left) and power (right) characteristics for 4 different rotational speeds at 60° IGVs angle. Yellow curves are for the nominal speed.

University of West Bohemia, Faculty of Mech. Engineering   Dissertation thesis 2022/23

Department of Power Systems Engineering   Ing. Lukáš Hurda

The R&D teams of Howden ČKD and UWB NTC discussed the instabilities and suspected a boundary layer separation in front of the impeller inlet to be causing the problems. The presented work is focused mainly on this phenomenon; identifying it, describing it, predicting its occurrence and preventing it. However, it is not proved in advance, that other problems in the flow field do not play a role in the exhibited unwanted behaviour of the test compressor.

1.3   Related research

Besides the research directly connected to this thesis, various other topics were covered, including analysis of the reliability and optimization of the measuring equipment by [1] and [2], influence of nuances in geometry for different impeller manufacturing technologies by [3], impeller cover disc seal performance assessment by [4].

1.4   Goals

- Describe the emerging flow instability in order to predict its origination within the analysed stages. Generalize to other centrifugal compressors if possible.

- Write and use a computer program for universal measurement evaluation at the compressor test bed facility. Keep it organised and modular for the possibility of a future expansion to general turbocompressor testing tasks. Use real gas equation of state for the measurement evaluation and incorporate rescaling and correcting the measurement data to the reference intake state and the impeller rotational speed.

- Perform a parametric study to determine or predict the unstable operating regimes. Use methods of Computational Fluid Dynamics for numerical flow simulations supplied by preceding dimensional analysis of the problem.

- Simulate the flow in the test bed compressor to confirm the conclusions of the parametric study.

- Suggest possible design improvements to the test bed compressor geometry to alleviate the effects of the unstable flow. Verify the influence of the design recommendations if possible.

1.5   Thesis outline

These paragraphs give the reader an insight into the logical arrangement of the thesis, which may not be clear from just going through the table of contents.

University of West Bohemia, Faculty of Mech. Engineering   Dissertation thesis 2022/23

Department of Power Systems Engineering   Ing. Lukáš Hurda

First, the theory and methods will be described in chapter 2. In section 2.1, dimensional analysis is presented as a versatile tool used in many parts of the whole analysis, including applications directly described later in other parts of chapter 2.

The working principles of centrifugal compressors are explained in more detail alongside with methodology of the impeller design, which is attempted later in pursuit of increasing the operational stability of a selected stage in subsection 3.6.4. In fact, the original impeller geometry retrieval for subsection 3.6.1 also relies on this design methodology.

In section 2.3, measured data processing is treated in a quite universal way, so this chapter can also serve as a standalone part. The software was initially developed for routine use during standard measurement campaigns on the test bed. Although it was necessary to develop such a methodology to obtain the results presented in section 3.3, the outcomes would not be significantly different if the software was far less sophisticated. For example, real gas behaviour could be neglected or the software architecture would not need to be as modular as it is. The measurement analysis code could be easily repurposed, including functions of re-scaling the measured data to compressor stages of different sizes, rotational speeds or working gases.

Section 2.4 summarizes the general theory of computational fluid dynamics (CFD) methods used throughout the thesis, including the specifics of turbomachinery simulations.

The methodology is then applied to a set of various models, discussed in chronological order - which also means going from the simple to the more complex. Every section of this chapter has its own conclusion, allowing for a more concise discussion of the whole analysis.

The first application of the dimensional analysis is the description of the flow in the toroidal inlet channel, ignoring the impeller (section 3.1). After that, simple 0D models are built to clarify the expectations of the compressor duty at a full range of the operating conditions based on the impeller intake state (section 3.2).

Measurement data are presented in section 3.3 to identify the unstable operating parameters of the compressor and evaluate the absolute flow velocity angle, which could help discover the origin of the problems.

Afterwards, numerical simulations are utilized to get an insight into the flow field in critical areas and operating regimes identified in the previous chapter. The models are put together using the methods given in section 2.4.

The subsections deal with the parametric study of an inlet channel flow (section 3.4) linked to the theory from section 3.1, a verification of the operation of the sole inlet guide vanes in section 3.5 and finally a whole compressor stage models in section 3.6. This subsection describes the design of the compressor stages, the computational models and the results.

First, the original s4 impeller substitute is designed and modelled using two approaches of inlet flow swirl generation (subsections 3.6.1 to 3.6.3).

The new, hopefully more stable, impeller design is dealt with in subsection 3.6.4 and it is modelled in one variant only - including the IGVs (subsection 3.6.3).

After presenting and discussing all the approaches to the problem using different models, generalized conclusions are drawn in chapter 4. This chapter begins with a discussion of the results of the particular models. Then it features the compressor design recommendations, reveals the outlook for future work, highlights the contributions to the field and gives a final conclusion. The last section 4.4 reflects on the achievement of the objectives set in section 1.4.

University of West Bohemia, Faculty of Mech. Engineering   Dissertation thesis 2022/23

Department of Power Systems Engineering   Ing. Lukáš Hurda

2   Theoretical background and methodology

2.1   Dimensional analysis

Dimensional analysis is applicable in all disciplines of physics, but it has the strongest tradition in fluid dynamics and heat and mass transfer. Almost every fundamental textbook in this field explains it in some of its forms. Most of the time, it is presented as a tool to interpret and reduce the data collected on experimental or computational models, such as in [5]. In spite of that, it can serve various other purposes, one of which is the turbomachinery design or type selection. Such approaches can be found in [6, 7].

It relies on the premise, that physical phenomena exhibiting similarities in geometry and distributions and transfers of governing physical quantities will also show similar behaviour. It is deducted from the fact that the laws of physics are not influenced by the choice of units used to express the involved quantities. The whole analytical work is then concentrated on finding the dimensionless products (criteria) of characteristic geometric, fluid, operational and performance parameters to correctly express this similarity. In such a way, a universal reduced model is obtained. In many scenarios, an experienced engineer or physicist can find the relations intuitively, but general approaches exist, like the Buckingham's Π-theorem, whose use is thoroughly explained in [5].

The theorem basically says that the number of independent dimensionless quantities (criteria) describing a problem is lower than the number of involved variables by up to the number of the physical dimensions of these variables - these could be taken from any consistent system and the SI basic units set is the most obvious choice. From such a set, only mass, length, time and temperature are relevant for common problems in fluid dynamics. It is worth noting, that angles are already dimensionless (radians giving the proper scaling of *arc length/radius length*) and they can also play role of a geometric parameter. There are often no reasons not to take an important angle as a criterion straight away.

This reduction rule is quite powerful in simple setups, but with complexity, especially geometrical, it loses its charm. However, one can take advantage of it in complex geometries while freezing the shape and only studying the influence of the operational parameters and/or the physical scale of the system. In some canonical tasks like water turbine type selection, one can also neglect the smaller nuances between machines of certain types and just work with a basic length characteristic like the diameter of the impeller.

University of West Bohemia, Faculty of Mech. Engineering   Dissertation thesis 2022/23

Department of Power Systems Engineering   Ing. Lukáš Hurda

The Π-theorem is applied in section 3.1, but there are many non-dimensional quantities used in fluid mechanics, whose use is rather general and the underlying analysis is taken for granted, as it has been published along with the fundamental principles.

These include coefficients of pressure (C_p) and friction (C_f) on the walls or especially blades, the ratio of ideal gas heat capacities (κ), non-dimensional wall distance (y^+) characterizing velocity boundary layer behaviour and used to assess its proper spatial discretization in numerical simulations. Besides the physical criteria, the Courant number for assessing and setting up time discretization numerical schemes is worth mentioning.

From the many repeated dives into similar problems, some classical criteria have been established the most notable of which include: the Reynolds number (Re - ratio of viscous to inertial forces), the Mach number (Ma - sonic speed criterion used to decide on the compressibility of the flow) and the Strouhal number (Sh - kinematic criterion for periodical flow effects).

The operation and design of turbomachines has also been subjected to dimensional analysis and the apparatus used to do this is summarized in subsections 2.2.3 and 2.2.4.

The dimensional analysis does not inevitably need to yield a clear and final relation between the criteria, it is also a valuable outcome to just be sure that when looking at a particular experiment or simulation, the flow field and the overall behaviour of the system will be the same in any combination of inputs or scale yielding the same values of all the criteria. In other words, once the phenomenon is described by the set of criteria, one can evaluate any output parameter response ex-post if sufficiently complete data are collected during measurement or simulation.

2.2   Centrifugal compressors

A general discussion on the purpose of the whole range of applications and varieties of centrifugal compressors has been presented in the Introduction.

Section 1.2 states, that all the material presented deals with a single stage of a compressor, or better - a compressor comprising of one single stage. Multistage compressors exist for cases where it is not feasible to design a single stage machine capable of delivering high enough pressure.

2.2.1   Stage layout

A stage is the smallest part of the machine that can perform the desired function on its own. It consists of an impeller as the main functional part of the rotor (15 in Figure 2.1) and a diffuser (19, optionally with vanes - 29; in the same Figure) as the main functional part of the stator.

University of West Bohemia, Faculty of Mech. Engineering   Dissertation thesis 2022/23

Department of Power Systems Engineering   Ing. Lukáš Hurda
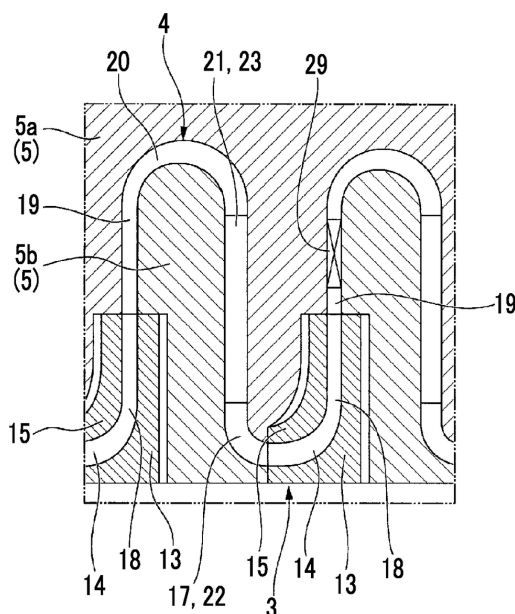
Figure 2.1: A cutout of a meridional section of a centrifugal multistage compressor, taken from [8].

Unlike some radial turbine designs, compressor stages are almost never arranged along the radial direction, but along the axis instead. This requires the return channel (Figure 2.1 - 21), which is usually equipped with de-swirl vanes. These are designed to provide no kinetic to pressure energy transfer but just the turning of the flow to the axial direction at the inlet of the forthcoming stage - ideally with a zero change in meridional velocity magnitude.

Industrial multistage machines have two design concepts: a barrel casing and a conventional split casing. The barrel type is preferred for simplicity and lower cost while achieving superior characteristics to survive very high internal pressure. Both types usually feature a toroidal inlet chamber with a central radial inlet pipe. Therefore it is best to shape the first stage inlet in a similar way to the return channels in between the stages and keep the shortest possible axial length of the machine. This has a direct influence on the distance between the shaft bearings and the complexity of the rotor dynamics design.

2.2.2 Shrouded impellers

Besides the shaping of the blades, there is one key design feature which distinguishes different kinds of impellers - the shroud disc. Free blade tip impellers are much simpler to manufacture and they are a popular choice in small diameter impellers and many single-stage machines thanks to their low inertia - a significant benefit for unsteady working

University of West Bohemia, Faculty of Mech. Engineering   Dissertation thesis 2022/23

Department of Power Systems Engineering   Ing. Lukáš Hurda

conditions. However, due to the tip leakage losses[1], they are less efficient. They could also be more fragile in comparison with their counterpart.

Shrouded impellers incorporating rotor seals at the shroud disc are more efficient due to the better flow guidance and absent tip leakages, but they are challenging to manufacture. Even modern 5-axis milling machines are often incapable of reaching all the spots of the interblade channel, especially in lower flow capacity stages with narrow impeller channel. For conventional metal parts manufacturing, there is no other option than to make the rotor in two pieces and then join them using welding or brazing (possibly also bolted or nipple joints might be feasible in some designs).

Shrouded impellers are common in industrial multistage machines, where their structural robustness and high efficiency is valued. In fact, omitting a shroud is out of question in such machines. The design is heavily constrained by the constant diameter of all the impellers in one casing to keep a high enough circumferential speed of the blades at the impeller outer diameter for all the stages mounted on a single shaft, rotating at a uniform speed. Given the mass flow rate through the stages is constant and the gas density increases geometrically stage after stage, only a few of the stages can have a near optimal channel width while maintaining a reasonable meridional speed of flow. The later stages can have an impeller exit diameter to width ratio well over 20 - without a shroud, the efficiency of these stages would be unacceptably low.

The sometimes necessary two piece impeller concept introduces even more design constraints and some trade-offs are inevitable. The impeller geometry presented in section 3.6 has a purely radial entrance with prismatic blades due to its brazed two-piece design limits. The brazing can only be done on a planar joint surface. While finding such a surface in a complex 3D shaped blading need not be impossible, the structural stresses were found to be below the limits of the joint for prismatic blades only. This impeller was chosen to be the optimum by the manufacturer, even though it has no inducer part[2] and the axial to radial bending of the flow along the shroud is rather sharp. [9]

---

[1]Tip leakage is one of the mechanisms of secondary flow losses developed in the free blade tip impeller. Due to the finite size of the blade tip to casing clearance and the pressure difference across the blade tip created by the rotating blade, part of the flow rate trips over the tip from the pressure side to the suction side. This amount of gas fails to absorb all the kinetic energy and partially fouls the channel with adverse vortex flows.

[2]The inducer is the entrance part of an impeller with an axial or mixed inlet. Historically, it used to be a well-distinguished part of the blading, where the axial part of the stagger curvature is concentrated. This allows reasonable incidence angles even for otherwise purely radial (planar) blades. Modern blading designs feature integrated inducers, where blade leading edge twist is combined with the wrap and radial stagger of the blade to form a 3D blade shape. Radial inlet impeller flows lack the axial velocity component, so they do not need an inducer.

2.2.3   Compressor duty

2.2.3.1   Dimensional similitude

As mentioned in section 2.1, the operation of a turbocompressor is defined by geometric, fluid, operational and performance parameters.

Lets concentrate first on the analysis rather than the design tasks and fix the geometry.

The most important parameters describe the **performance**: the *flow rate* (in terms of mass, to be universal) and *discharge pressure*. Right after that, the user would be interested in how much *power* the machine requires.

Speaking of the **fluid parameters** - in the aerospace or turbocharger industries, one is typically never confronted with gases other than air and flue gas, but in industrial compressors, the range of substances having different *viscosity*, *specific heats* and *other thermophysical properties* is quite wide. It might be rare to have a single machine compress completely different substances at different times, but it is not uncommon to use geometrically similar designs for a multitude of compressors with various working fluids or to process a gas mixture which changes its composition and properties up to a certain degree - even during the operation of the machine.

The **operational parameters** are the results and the rather immutable inputs of the compression process: *the discharge temperature* could be questioned and of course, the machine operation is dependent on *the working fluid state at its inlet*. Then there are also the quantities, whose values are purposely changed in order to control the process (in the machine design stage at the very least). *Rotational speed* of the impeller, *angle of the IGVs* and the *resistance of the suction or discharge tracts* correspond to the means of control briefly assessed in section 1.1.

The above summary calls for a clear definition of the characteristic *stations*, at which the localized quantities mentioned are evaluated throughout the design process, followed by experimental or computational analyses. In Figure 2.2 the stations are labeled. Some of the quantities are not localized to a station, but they describe a process taking place in between the start and finish stations. A pair of stations outlines a *section*.

The mentioned quantities are effectively reduced by means of the dimensional analysis to a set of standard criteria used generally in compressors. Their definitions are presented with respect to conventions, but the localized values can be sensibly and consistently substituted with the same quantities at an arbitrary station. The process-related criteria rely on the selection of section inlet and outlet and therefore their definitions use "I" and "O" subscripts respectively.

The standard compressor operation analysis uses 4 of them as controlled inputs:

1. Working gas specific heat ratio $\kappa = \dfrac{c_p}{c_v}$

University of West Bohemia, Faculty of Mech. Engineering   Dissertation thesis 2022/23

Department of Power Systems Engineering   Ing. Lukáš Hurda
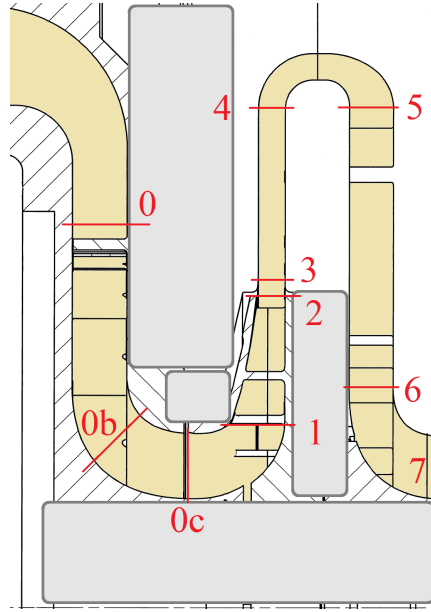
Figure 2.2: Meridional section through a test bed compressor. Confidential parts greyed-out. Adapted from [10].

2. Blade exit Mach number $Ma = \dfrac{u_2}{a_{tI}} = \dfrac{D_2\Omega}{2a_{tI}}$

   - controlled by the rotational speed

3. Inlet flow swirl angle α_1

   - controlled by IGVs and their stagger angle ϑ

4. Flow coefficient $\Phi = \dfrac{Q_{tI}}{A_0 u_2} = \dfrac{G}{\rho_{tI} A_O u_2}$

   - controlled by varying discharge (and/or intake) tract flow resistance - this is often the primary variable (can be redefined using arbitrary convenient flow area A and blade circumferential speed different from u_2)

The 3 remaining criteria can be perceived as the outcomes of the machine's response to the inputs:

6. Total to total pressure ratio $\Pi = \dfrac{p_{tO}}{p_{tI}}$

7. Power or loading coefficient $\Psi = \dfrac{h_{tO} - h_{tI}}{u_2^2}$; for perfect gas $\Psi_{PG} = \dfrac{c_p(T_{tO} - T_{tI})}{u_2^2}$

8. Relevant type of thermodynamic efficiency $\eta_{ise}, \eta_{pol}, ...$

The type of thermodynamic efficiency is distinguished by the various ideal process definitions. The isentropic efficiency η_{ise} feels the most natural to assess the quality of energy

transfer during the compression - the assumption of an adiabatic process is often close to reality in compact high speed machines. However, for comparisons of operating points or stages which work with significantly differing pressure ratios, polytropic efficiency η_{pol} is a more accurate measure, as it introduces no penalty to high Π cases. A detailed explanation is given in [6].

It is worth noting, that it is standard to neglect the Reynolds number effects, because very high values are expected - inertia dominated flows with intense turbulence. This is usually valid in the impeller and diffuser in near nominal operating conditions, but not necessarily in the intake channel.

2.2.3.2   Compressor maps

The set of performance curves usually provided by a compressor manufacturer is called a compressor map. Absolute, not dimensionless, parameters are usually presented for one specific machine of fixed dimensions. The basic curves are obtained for a multitude of constant rotational speeds. The most important is the pressure-flow rate map, often with efficiency contours laid over. See Figure 2.3. It is valid for one single specified gas composition with a reference intake state (dry air in this case). The flow rate can be specified in terms of mass or volume and the parameters can incorporate the corrections for the actual intake state, like the temperature correction shown in Figure 2.3. The Figure uses volumetric flowrate Q evaluated at the inlet. The indices used in the Figure are: r for the reference state, 0 for the total state, 1 and 2 for the inlet and discharge stations. The required power curves are provided when necessary (not in the Figure).

The natural limits of the compressor map are: the choke limit at the maximum possible flow rate and the surge limit on the opposite side of low flow rate:

Choking means reaching the sonic speed at a certain place in the machine, usually near the impeller inlet. The channel geometry does not allow supersonic expansion, so the critical flow velocity, which cannot be further increased, is the sonic speed. The flow rate is therefore limited too. It is a steady and stable state, but with a significant efficiency penalty.

Pressure surge is an unsteady phenomenon caused by a pressure on the compressor discharge side which is too high (even when created by the compressor itself). This leads to periodic flow reversal backwards through the impeller. The whole volume of fluid at the discharge side acts as a spring, so the action reaches high pressure pulse amplitudes with low frequency (in the order of $1\,\mathrm{Hz}$ for industrial- or aerospace-scale machines). In axial compressors, it can lead to immediate irreversible damage to the machine. In robust centrifugal industrial compressors, an immediate counteraction of the machine control (manual or automatic) is enough to prevent significant persistent adverse effects.

Nevertheless, a safety margin is often created to offset the practical compressor operating points presented in the compressor maps from the surge limit. Another practical reason for this is that near surge, the slope of the pressure-flow rate curves is positive unlike the
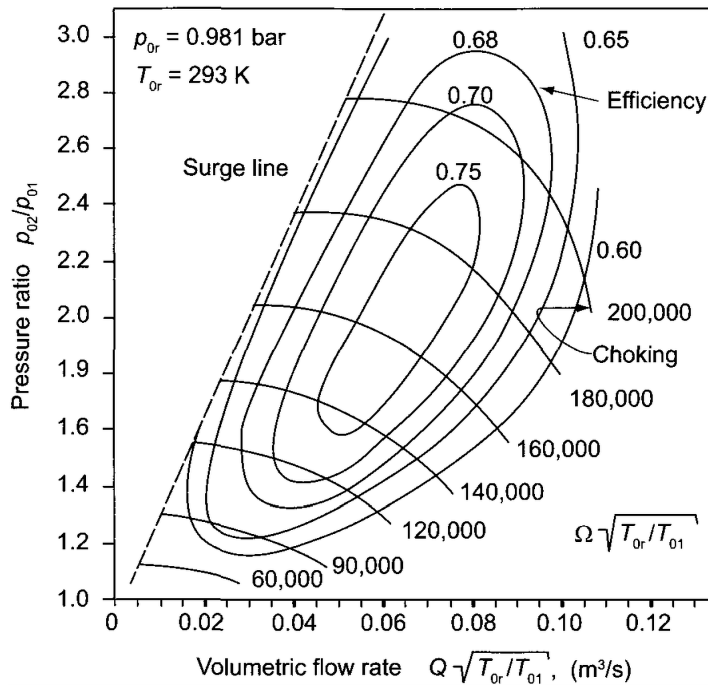
Figure 2.3: Example of a compressor map from [7].

rest of the characteristic. Using the pressure curve across the whole flow rate interval would yield ambiguous results of the inverted "flow rate from pressure" evaluation, which is necessary in machine control. Even when the offset from the surge is safely large, the curves are often trimmed from the left-hand-side at the pressure maximum.

2.2.3.3   Velocity triangles

The flow velocity vectors can be observed in the absolute frame of reference and in the impeller; it also makes sense to observe the flow in the rotating frame of reference connected to it.

At the impeller inlet station it is crucial for the optimal performance to align the flow along the blades or vice versa. At the impeller outlet station, the deviation of the flow from the direction of the blade at the trailing edge determines the quality of the energy exchange inside the rotor.

Velocity triangles are a great tool to picture the relations of absolute ($\vec{c}$) and relative ($\vec{w}$) velocities and the carrying rotational velocity ($\vec{u}$), which has a tangential direction and a magnitude respective of the given radius from the machine axis and the impeller angular speed. It is a graphical representation of the vector equation $\vec{c} = \vec{u} + \vec{w}$.

2.2.4 Impeller design

In this thesis, a full design of a stage is not performed. As the full test bed compressor geometry was not available in any live digital format, partial reverse engineering was used. This, in fact, just adds a few constraints to the full design process, taking away the necessity of a few of the designer-made decisions. The general approach is commented on here and the specific tasks of original impeller re-design and new impeller design are ascribed in section 3.6 and subsection 3.6.5.

A powerful software tool developed by Prof. John Denton, retired, from the Whittle Laboratory based at the University of Cambridge, `mulltall-open` is used for the generation of the compressor geometry. This software package also includes a 3D turbulent flow Navier-Stokes solver, but only the meanline design tool `meangen` and the stage geometry generator `stagen` are used here. The software was published in [11] and is available from [12].

After consulting the `meangen` manual, the procedure of defining the stage was outlined. For mixed flow or radial machines, it was necessary to input the design stream surface radial and axial coordinates. Since the channel geometry was known, a digitized curve of the hub was used and selected as the design surface. The locations of the impeller blade leading and trailing edges measured from a blueprint were input and blade metal angles were noted.

There is no explicit way to define the other channel limiting surface - the shroud. The distribution of meridional velocity magnitude along the design surface is provided in a form of a coefficient value for every single point of the design surface. The set of coefficient values was iterated several times to conform to the real compressor shroud contour.

The design operating point is specified by $\kappa, r, T_{tI}, p_{tI}, \Omega, G$. Dry air ambient air parameters were entered, as during the original real stage design. The blading geometry definition strategy is based on the whole stage (impeller and diffuser, no IGVs or OGVs), absolute inlet and exit angles together with flow and power coefficients. These coefficients had to be evaluated at the leading edge of the rotor blades, so they differ in values from the most common definitions presented in paragraph 2.2.3.1.

There is no option for designing a bladeless diffuser in `meangen`, one can only omit the stator blading in further procedures. The other option of operating point specification by all 4 flow angles (inlet and exit relative and absolute flow angle for rotor and stator respectively) proved to be less practical for the presented cases.

A real world operating point was carefully selected and evaluated from one of the test bed measured operating points with the knowledge of the design rotational speed. Theoretically, the design point should reach peak efficiency - such a point is found and used. The isentropic efficiency value itself is also used as an input. Incidence and deviation angles of the rotor blades need to be guessed.

University of West Bohemia, Faculty of Mech. Engineering   Dissertation thesis 2022/23

Department of Power Systems Engineering   Ing. Lukáš Hurda

Incidence can be evaluated relatively simply - the design is carried out with zero inlet flow swirl and known leading edge circumferential speed, so the relative flow angle at the leading edge is only dependent on the static density, which is iterated to reach the desired metal angle. The final value is expected to be between -5° to 0° as one of the signs, that the selected design point is not vastly different from the original one.

An estimate of the trailing edge deviation angle is finally used as the main degree of freedom of the design process. Similarly to the LE incidence, it is an offset of the angle of the designed blade from the computed relative flow angle. It can reach well above 10° even on the design point for a centrifugal impeller with a relatively low number of blades and no splitter blades [13].

Blade number and thickness was approximated to the real compressor. A cut-off trailing edge was set up, but it required corrections. These were administered by the author's program script used primarily to convert the cylindrical coordinates to Cartesian and output the characteristic curve files for the channel surfaces and blade profiles, to be read by `TurboGrid`. More to the geometry manipulation leading to the computational model can be found in paragraph 2.4.2.3.

2.3 Measurements

2.3.1 Description

A complete computer program for the measurement evaluation of centrifugal compressor tests is presented.

The development was motivated by the needs of the concerned compressor test bed. The outputs were to be used as an input for the commercial radial compressor design process. A few of the final parts of the evaluation were handled manually. These were the semi-empirical modelling of the rotor seals to cancel out their influence on the evaluated compressor maps and the final polynomial curve fitting of the data.

There are intentions to use the same code to analyse the measured data from the commercial machines in factory testing or on-site to have a consistent methodology. Some functionality is missing for this purpose, but the architecture allows various add-ins.

2.3.1.1 Calculation outputs

The most important outputs are the integral performance curves of the compressor. Typically, this involves the discharge total pressure p_D, the shaft power N and the efficiency η versus the gas mass flow rate G for a given rotational speed Ω. Discharge temperature T_D may also be useful. These parameters can also be expressed in a dimensionless manner (the efficiency is dimensionless already): the pressure ratio Π and the power coefficient Ψ versus the flow coefficient Φ for the given reference (blade) Mach number Ma_{2u}. There

are two useful types of efficiency - polytropic and isentropic - based on what is considered to be the theoretical ideal of the required power. The isothermal efficiency is not usually suitable for turbomachinery.

Besides the integral quantities, one may be interested in local state variables at various measuring stations. It is generally possible to measure the (wall) static and total pressures and the total temperature anywhere in the compressor excluding the impeller interior. To obtain complete information about the gas thermodynamic state, pressure and temperature needs to be measured in a single profile perpendicular to the meridional component of flow velocity in order to be able to precisely correct the measurements and evaluate static parameters, density and flow velocities. This applies to the stations where high flow velocities occur, the flow is compressible and sources of heat and momentum are close. It is not always possible or feasible to equip such a station completely, so corrections, simplifying assumptions or extrapolation may be applied. Flow criteria such as the Reynolds or Mach numbers may also be expressed.

2.3.2   Measured data evaluation

2.3.2.1   Real gas parameters

The implementation of the gas state properties along with some important thermophysical properties dependent on them is universal. The limitation is that the input parameters for the equation of state (EoS) are always pressure and temperature. This is the way most general equations of state used for real gases are explicitly written.

Current code includes perfect gas along with the Sutherland formula for viscosity and the Benedict-Webb-Rubin (BWR) real gas equation. The variant with 11 substance constants is used. This equation is commonly used for hydrocarbon gases and their mixtures. The mixture is simple to account for with BWR. As long as constants for all its components are known, new constants for the mixture of a given composition can be evaluated easily. This also allows incorporating the humidity of air or any other gas. Calculations near the critical point may fail or lead to invalid results. In practice this has only caused problems with some individual carbon dioxide compressors [14].

The nature of the EoS explicit for pressure and temperature asks for iterative procedures at many instances in the program. This includes mainly the need to calculate the theoretical isentropic compression and another isentropic phenomenon - the static and total parameters of a working fluid are constrained by an isentropic process. In this case, the iteration becomes nested, e.g. the static pressure is quantified based on the current estimate of static temperature and total specific entropy, which remains constant and then the static temperature may change for the next outer loop iteration as the estimation of flow velocity gets adjusted.

2.3.2.2 Workflow

The calculation takes place after data loading and averaging the spatial multiples of measured quantities. The averaging itself is not trivial. Cases are handled when total pressure and temperature is sensed by a number of multi-sensor rake probes or a set of single sensor probes in a single measuring station. It balances the averaging weights of single values to cancel the influence of a sensor which was turned off due to a defect causing irregular spatial distribution of the remaining sensors. For static pressure wall taps, it is able to distinguish whether the tap is on the impeller hub- or shroud-side wall. Then the program offers two averaging weights distribution options for cases where the numbers of taps on both sides of the flow channel are not equal – equal weight for all taps or equal weight for both sides, where taps are averaged a priori.

The calculation itself is split into five main parts:

1. The first part is the calculation of gas streams involving every configured orifice flowmeter. At the beginning of this procedure, the correct humidity sensors are found for every orifice and the gas composition of the whole stream is determined, the BWR constants are loaded. The humid gas mass flow rate can then be determined from the orifice plate differential pressure sensor using also the temperature and the absolute pressure in front of the flowmeter. The process is not commented on later because the real gas EoS causes no difficulties here. The routine is built according to a technical standard on flat plate orifice flowmeters [15].

2. The second part is the determination of gas thermodynamic state in all configured measuring stations. A paragraph is devoted to the details of the procedure. The top level ensures using the data from the correct gas stream - the composition of gas and already determined mass flow rate.

3. The third part is the assessment of power loss in the rotor bearings. It is the only influence on the power measured by the torquemeter which can be relatively reliably quantified and then subtracted from such a gross measured shaft power. Then the result can be later compared to the power resulting from thermodynamic calculations. The procedure is a straightforward use of a calorimetric equation applied on the oil flow rate and the temperature difference between the injection piping and the drain basin of the bearings box. Surprisingly, the compulsory thermophysical data of the oil are not fully supplied by the manufacturer and it is not easy to find a relevant source. The book [16] was used as a source, but the original source can be tracked back to the 1920's, before the existence of synthetic oils [17]. The reliability of such data is questionable without the relevant measured values of the temperature dependent properties. The bearings loss routine can be theoretically launched independent of the first two parts, but it has to be finished before starting the last part.

4. The key step of data processing is the calculation of the compression process for all the configured sections. The sections are defined by a pair of intake and discharge stations and can be sequential, overlapping or any possible arrangement as the section

University of West Bohemia, Faculty of Mech. Engineering   Dissertation thesis 2022/23

Department of Power Systems Engineering   Ing. Lukáš Hurda

results can also be a useful standalone output. It can be specified which sequence of sections forms a complete machine, so their parameters add up.

5. After the calculation of the actual measured process, its parameters are scaled to standardized intake gas parameters and also a correction to standardized impeller rotational speed. A single paragraph is dedicated to both of these sub-steps of section data processing.

2.3.2.3 General concepts

When an iterative procedure is employed to express state variables implicitly, an initial estimate of pressure, temperature or both is made depending on whether any of them is fixed or not. An arbitrarily wide interval around those approximate values is generated and its boundary values are used both for the expression of the state variable which is known to remain constant (usually specific enthalpy or entropy). Using linear interpolation, the pressure or temperature value is corrected. A residual of the constant quantity can be evaluated and if it has dropped since the last iteration, the new interval around the new value of pressure or temperature is narrowed. Fast convergence is usually experienced.

The wide range of extreme operating conditions of the experimental compressor was a driver for some robust implementation features. The conditions can involve problematic compression processes where very low compression occurs, low flow rates causing the adiabatic premise to be false, low efficiency causing the polytropic exponent to be very large or even negative, and so on.

At some points in the code, limiting functions of minima and maxima were applied to the interpolated values. Also, every while-loop break is triggered when every convergence condition defined is met. The set usually includes relative residual and absolute residual and, in some cases, more trigger quantities are chosen.

2.3.2.4 Humid gas mixtures

The BWR EoS constants for mixtures of gases are expressed based on volume fractions of its components. This is a user input for a dry mixture or mixture with known humidity, but when the humidity is variable, it needs to be measured and the constants of the user-input mixture need to be adjusted to incorporate the right amount of water vapour. Relative humidity is measured. It is necessary to calculate the water volume fraction from the relative humidity. The water vapour saturation pressure is stated using Antoine equation for temperatures below $276\,\mathrm{K}$ [18] and for higher temperatures a proprietary equation of similar exponential type is used. The transition between those two expressions is step-free and practically smooth, although not mathematically smooth. The vapour partial pressure $p_{pV} = \varphi p_{sat}$ from saturation pressure p_{sat} and relative humidity φ is used to get the vapour volume fraction $c_V = p_{pV}/p$. The user-supplied vector of dry mixture volume fractions is then normalized and new BWR constants are calculated for a humid mixture.

2.3.2.5 Gas state in the measuring station

The primary purpose of this routine is to state the flow velocity in the station and fix static and pressure parameters by doing so. Considering high velocity in a station, there are three possible types of gas state analysis.

1. Non-swirling flow is assumed, total pressure and temperature is used.

2. Non-swirling flow is assumed, static pressure and total temperature is used.

3. Swirling flow, both static and total pressure and total temperature need to be used. Tangential velocity component is determined.

For non-swirling flow the absolute flow velocity equals the velocity normal to the station surface (meridional velocity component), which can be evaluated from mass flow rate, fluid density and surface area as $c_m = c_\rho = G/(A\rho)$. The density is a static parameter and in all the calculation types, the static state is not fully defined.

Specific enthalpy h is converted to kinetic energy when increasing gas velocity c isentropically $h_s = h_t - c^2/2$. No further derivation of explicit expressions for dynamic pressure or temperature is possible in real gas. Expressions valid for compressible flow of perfect gas like $T_s = T_t - c^2/(2c_p)$ or $p_s = p_t(T_s/T_t)^{\kappa/(\kappa-1)}$ are not valid for real gas. The specific heat c_p and isentropic exponent κ are not constant during the adiabatic process and mean value usage is neither always feasible nor accurate enough.

Therefore the missing total or static parameters (based on the type of algorithm enumerated above) need to be iterated when the p, T explicit EoS is used. The loop is stopped when the velocity evaluated from dynamic enthalpy c_h matches the velocity evaluated from flow rate c_ρ: $(c_\rho - c_h) <$ tolerance.

Another phenomenon playing a role here is the restitution factor of the total temperature probe. The thermocouple sensor together with specifically designed deflector bring the fluid to stagnation at the sensing location with only partial success. The recorded value of temperature T_{tm} needs to be corrected and the correction based on restitution factor F_r is dependent on the unknown velocity of the flow. The corrected total temperature T_t has an effect on the quantification of the velocity, so the equation equation (2.1) needs to be a part of the iteration loop mentioned above.

$$T_t = T_{tm} + (1 - F_r)(T_t - T_s); \qquad F_r = f(c) \tag{2.1}$$

Values from well-designed static pressure wall taps can be used directly as well as total pressure values if the probe deflector is directed to face the flow perpendicularly. The angle setting for the used probes has a relatively large insensitivity margin of around $\pm 15°$.

The swirling flow procedure is similar, but the absolute velocity defined from dynamic enthalpy $h_t - h_s = c^2/2$ is not comparable to the meridional velocity component c_m defined from mass flow rate. Pressures are fixed from the measurement. The total temperature

is corrected by the restitution factor in the iteration loop whose primary task is to reach the correct static temperature T_s and absolute velocity based on $h_t - h_s$ and meridional velocity based on ρ which, of course, is also adjusted in the loop. The threshold expression for the loop mentioned above is not applicable here, so only the relative change of c between iterations is checked to be below the threshold to stop the loop.

2.3.2.6   Polytropic compression

The compression is considered adiabatic, although both experimental and production machines are not usually insulated. The mass throughput of the compressor is so large compared to the surfaces where heat transfer to the environment occurs, that this assumption is valid for most cases.

The main task of this procedure is to find the ideal isentropic discharge temperature based on the fully determined states at the beginning and end of the irreversible adiabatic process. The theoretical compression is defined by the same starting gas state and identical pressure at the end. The only unknown is the temperature at the end of the process, which is iteratively found based on the constraint of constant entropy. Again, the iterative process is necessary due to the implicit nature of EoS to entropy. The isentropic discharge temperature allows stating the isentropic specific work and later the isentropic efficiency.

Finally, ideal polytropic specific work is expressed algebraically to later state the polytropic efficiency. See [6] for an explanation of the advantages of using polytropic efficiency along with the isentropic efficiency. There are various attempts on how to account for the change of the polytropic exponent during the process in a real gas. One from Schultz, dated 1962, is also supported by the ASME PTC 10 standard [19, 20]. An alternative could be the Mallen-Saville formula from [21], Oldřich's polynomial approximation [14] or finally, the numerical solution of the differential equation he mentions in the cited article.

The first two alternatives are implemented in the measurement evaluation program. Schultz [22] uses parameters of the ideal adiabatic compression, see equations (2.2) to (2.5).

$$n_{ise} = \frac{\log_{10} \frac{p_{tD}}{p_{tI}}}{\log_{10} \frac{\rho_{tDise}}{\rho_{tI}}} \tag{2.2}$$

$$n = \frac{\log_{10} \frac{p_{tD}}{p_{tI}}}{\log_{10} \frac{\rho_{tD}}{\rho_{tI}}} \tag{2.3}$$

$$f_{corr} = \frac{h_{tDise} - h_{tI}}{n_{ise}/(n_{ise} - 1)(p_{tD}/\rho_{tDise} - p_{tI}/\rho_{tI})} \tag{2.4}$$

$$a_{TidSchultz} = f_{corr} n/(n-1)(p_{tD}/\rho_{tD} - p_{tI}/\rho_{tI}) \tag{2.5}$$

Mallen-Saville does not need such data - see equation (2.6).

$$a_{TidM-S} = a_T - (s_D - s_I)\frac{T_{tD} - T_{tI}}{\log_{10} \frac{T_{tD}}{T_{tI}}} \tag{2.6}$$

University of West Bohemia, Faculty of Mech. Engineering   Dissertation thesis 2022/23

Department of Power Systems Engineering   Ing. Lukáš Hurda

The stability of Oldřich's calculation seems questionable at first glance, but it may be interesting to try to implement the method in the future and see the results. The solution of the differential equation is not only tedious to implement, but also has prohibitively high computational costs if the calculation is used for live evaluation and visualization of acquired data.

When computing the regimes of an experimental compressor at a low reference Mach number ($<$ 0.5), the values of polytropic work evaluated from the two presented methods differ significantly. The comparison with the exact solution would be a valuable tool for validation purposes. The low Mach number also occurs in production machines working with low molar mass gases like He and H_2.

2.3.2.7   Intake gas state and composition scaling

Similarity theory in thermodynamics provides tools for rescaling the results obtained from the measured compression process in the machine section to any other state and composition of the gas in the section intake and possibly also different impeller outer diameters. Dimensionless criteria listed in paragraph 2.3.1.1 are kept constant. The influence of the Reynolds number is neglected, as noted in paragraph 2.2.3.1.

When the gas composition is not fixed, this is only an approximation, since κ was also introduced as a criterion, but it cannot be kept constant. In fact, it is not perfectly constant even for a gas of an unchanged composition, but an altered state, when the real gas description is employed. The ratio of sonic speeds incorporates the influences of κ, r and T, even for a real gas, where the relation $a = \sqrt{\kappa r T}$ is not generally applicable. The discrepancies in κ between the considered two gas states and/or compositions is further ignored besides the effects its changes have on other criteria via the ratio of sonic speeds.

It is necessary to process the measured data in this way to be able to compare the characteristics measured for variable ambient intake air conditions. These include humidity besides the pressure and temperature, hence technically giving different gas compositions (changing water vapour to dry air volumetric ratio).

A reverse process is applied to the datasets when designing a new machine for a specific application. Only in these cases, large differences in κ can occur.

The absolute scaled quantities can be expressed as below (indices: r - rescaled, m - measured; D - section discharge, I - section intake):

- Discharge total pressure   from constant π: $p_{tDr} = p_{tDr}\dfrac{p_{tIr}}{p_{tIm}}$

- Impeller rotational speed   from constant Ma: $\Omega_r = \Omega_m\dfrac{a_{tIr}}{a_{tIm}}\left(\dfrac{D_{2r}}{D_{2m}}\right)^{-1}$

- Mass flow rate   from constant Φ: $G_r = G_m\dfrac{\rho_{tIr}}{\rho_{tIm}}\dfrac{a_{tIr}}{a_{tIm}}\left(\dfrac{D_{2r}}{D_{2m}}\right)^{2}$

- Section specific work   from constant Ψ: $a_{Tr} = a_{Tm}\left(\dfrac{a_{tIr}}{a_{tIm}}\right)^{2}$

In the above equations, a_t, ρ_t denotes speed of sound and density evaluated from gas stagnation state and a_T stands for specific technical work done on the gas in the section.

The rescaled discharge total temperature T_{tDr} needs to be searched for based on the enthalpy change in the section. An initial estimate is made using working fluid heat-up criterion valid only for perfect gas - equation (2.7).

$$\frac{\Delta T_{tr}}{T_{Ir}} = \frac{\Delta T_{tm}}{T_{Im}} \quad \Rightarrow \quad T_{tDr} = \frac{(T_{tDm} - T_{tIm})}{T_{tIm}}T_{tIr} + T_{tIr} \tag{2.7}$$

The routine described above for polytropic compression is reused in an iteration loop to correct the initial estimate of T_{tDr} to conform to real gas behaviour. Discharge enthalpy reached with reference intake gas state is defined in equation (2.8).

$$h_{tDr} = h_{tIr} + a_{Tr} \tag{2.8}$$

Inside the iteration loop, T_{cDr} is adjusted till it yields the correct discharge specific enthalpy h_{tDr}. All the parameters of the fictional *reference intake state compression* are determined in the process by the polytropic compression routine – besides T_{tDr} and back-checked h_{tDr} these are the isentropic and ideal polytropic specific work a_{Tiser} and a_{Tidr} respectively. These are needed for evaluation of the rescaled efficiencies.

When there are more sections in a sequence, they need to be evaluated streamwise. The user prescribed reference intake state is applied to the intake of the first section and the scaled discharge parameters apply to the next station.

2.3.2.8   Rotational speed correction

An estimation is used to correct the discrepancies in the setting of impeller rotational speed to reach the correct reference Mach number during measurement. It could also ease the machine design process when data for exact required Mach number are not available and the designer needs to use the closest available performance curve.

Again, the process is based on the similarity theory, but the assumptions are more simplifying here and the procedure is correct and accurate only for slight changes in Mach number. One should view it as a type of extrapolation.

The subscript c denotes parameters corrected to reach the exact desired reference Mach number. The subscript r denotes parameters resulting from the intake gas state rescaling routine described in the previous paragraph.

The algorithm assumes the compression parameters do not change for both the real compression and the theoretical isentropic compression when there is a slight change in impeller rotational speed i. e. the blade Mach number. This yields the corrected polytropic and isentropic specific work (a_{Tc}, a_{Tisec}) and corrected mass flow rate (G_c) based on the ratio of the corrected and reference intake-rescaled impeller rotational speed (Ω_c/Ω_r), see equations (2.9) to (2.11). The gas intake state here is the same as for the rescaled quantities, so the density ratio is equal to unity and is not further mentioned. Possible geometrical scaling was also carried out in the previous step.

$$a_{Tc} = a_{Tr} \left(\frac{\Omega_c}{\Omega_r} \right)^2 \tag{2.9}$$

$$a_{Tisec} = a_{Tiser} \left(\frac{\Omega_c}{\Omega_r} \right)^2 \tag{2.10}$$

$$G_c = G_r \frac{\Omega_c}{\Omega_r} \tag{2.11}$$

Once the specific work is determined, discharge pressure and temperature can be searched for iteratively. Loop break threshold is the close approach to a_{Tisec}. The initial estimates of the corrected discharge total pressure and temperature are derived again from the perfect gas theory, see equations (2.12) and (2.13). The total discharge pressure p_{tDr} is received from an adjustment of rescaled rotational speed p_{tDr} with respect to the ratio of rotational speeds (Ω_c/Ω_r). The expression assumes $p_{tIr} = p_{tIc}$ and $p_{tIr} = p_{tIc}$, which is valid within this workflow. Starting with equation (2.10), taking advantage of trivial perfect gas expression for $a_T = c_p \Delta T$ and later eliminating temperatures by substituting $T_D/T_I = (p_D/p_I)^{(\kappa-1/\kappa)}$, the corrected pressure p_{tDc} can be expressed, as in equation (2.12).

The adiabatic exponent κ and specific heat c_p are evaluated from real gas EoS at an arbitrary suitable pressure and temperature as accuracy can be limited in the initialization process.

$$p_{tDc} = p_{tIc} \left\{ \left[\left(\frac{p_{tDr}}{p_{tIc}} \right)^{\frac{\kappa-1}{\kappa}} - 1 \right] \left(\frac{\Omega_c}{\Omega_r} \right)^2 + 1 \right\}^{\frac{\kappa}{\kappa-1}} \tag{2.12}$$

$$T_{tDisec} = T_{tIr} + \frac{a_{Tisec}}{c_p} \tag{2.13}$$

Both state parameters are adjusted in the loop while ensuring constant entropy at the intake and virtual discharge states at every iteration of the approach to the desired enthalpy rise a_{Tisec}. Similar procedures have already been described.

After the isentropic state change is defined, the corrected polytropic compression can be accounted for, yielding the same discharge pressure as the isentropic compression and the enthalpy change equal to a_{Tr}. The initial estimate of the temperature in equation (2.14) is analogical to the isentropic case above:

$$T_{cDc} = T_{cIc} + \frac{a_{tc}}{c_p}. \tag{2.14}$$

Ideal polytropic work for the corrected compression can be stated according to the approximative approaches mentioned in paragraph 2.3.2.6.

2.3.2.9 Determination of additional inlet channel flow parameters

Various additional quantities can be readily evaluated from the established station gas states or machine sections. As well as this, some more complicated, mostly approximative processes were developed for cases where station measurement is either incomplete or the temperature and pressure probe sets are offset from each other in a streamwise direction.

Simplifying assumptions then apply - such as adiabatic process allowing stagnation state extrapolation or approximating total pressure loss by static pressure differences between two streamwise locations. The most problematic part of such approaches is the influence of the flow swirl to the evaluation of absolute flow velocity magnitude. Only the meridional velocity component is readily obtained from mass flow rate and the flow area of the surface normal to the meridional direction. Density can be refined iteratively in such a process, as presented in paragraph 2.3.2.5.

These rather special and one-purpose routines are described in chapter 3 dealing with the specific models used - namely in section 3.3.

Extensive work would be required to carry out the research to find the best approach to express the ideal polytropic work with the use of a real gas. It is a problem which needs to be tackled very often and, in the author's opinion, the investment would pay off. Nevertheless, it is beyond the scope of this thesis.

A common approach to handling turbomachinery performance curves is polynomial fitting. This would be easy to implement, but it was not done due to the intended use of this program. The production of universal dimensionless performance curves for stage-by-stage multistage machine design requires one extra step before the polynomial regression: a proprietary empirical model to cancel out the influence of the rotor seals on the experimental machine needed to be applied to the data. The stages being part of the designed machine would then have their respective rotor seal performance approximated by a similar model fed with altered inputs and added back to the computed parameters of the stage.

2.4   Computational fluid dynamics

Commonly abbreviated as CFD, computational fluid dynamics is the tool of choice of turbomachinery engineers for both design and analysis. This scientific field was born and developed throughout the second half of the twentieth century along with the concurrent advancements in turbomachinery design. Along with aerospace, various turbomachinery industries have been the main sources of problems to be solved by numerical simulations of flow fields.

Nowadays the scope of commercial or open-source CFD solvers and engineering software tools is much broader and ever-expanding. While the solvers and mathematical models are becoming more universal and capable of handling unpredictable complex flows in and around complicated geometries, the tools to handle turbomachinery models are still here in all their beauty.

CFD is the final step in the machine design to prove that the simplistic design procedure (full of empirical models and neglected influences) is not totally off-reality. Besides that, it is now an optimization processor, a tool to analyse off-design conditions and whole operational maps and may detect adverse phenomena which the designer could have never thought of.

All of this thanks to improvements in turbulence modelling allowing us to predict boundary flow separation at a certain degree of accuracy, more realistic approaches to rotor-stator interfaces and robust solver architectures.

One cannot neglect that the increase in the computational power of modern computers is the second important part of such evolution - employing all of the demanding models and allowing either a few (possibly transient) simulations involving more interblade channels, more consecutive blade rows and finer meshes or a large quantity of simpler simulations.

In this thesis, both incompressible and compressible simulations were performed, in 2 or 3 dimensions. All of the flows were considered turbulent and were modelled using *Reynolds-averaged Navier-Stokes equations* (RANS) using the 2-equation k-ω SST turbulence model.

This rather traditional approach was selected due to the multi-parameter analysis concept which yielded a large number of computational cases. These required time steady simulations not only because of the lower demand of computational resources, but also the production of a manageably low amount of data to process. Any scale-resolving approach like *large eddy simulation* (LES) and its derivatives requires transient simulation. The few transient simulations undertaken were kept as k-ω SST unsteady-RANS for the sake of consistency.

The system of equations which was solved numerically using the established CFD software `OpenFOAM` and `ANSYS Fluent` is presented below. The types of boundary conditions, mesh interfaces and specific features used for the turbomachinery simulations are presented too.

University of West Bohemia, Faculty of Mech. Engineering   Dissertation thesis 2022/23

Department of Power Systems Engineering   Ing. Lukáš Hurda

2.4.1 Governing equations

Compressible fluid flow is described by a closed system of partial differential equations (PDE) called the Navier-Stokes equations and algebraic constitutive relations for fluid thermodynamic properties. The PDEs have a physical meaning of the conservation laws of mass (equation (2.15)), momentum (equation (2.16)) and energy (equation (2.17)).

$$\frac{\partial \rho}{\partial t} + \frac{\partial (\rho v_j)}{\partial x_j} = 0 \tag{2.15}$$

$$\frac{\partial \rho v_i}{\partial t} + \frac{\partial (\rho v_i v_j)}{\partial x_j} = f_i - \frac{\partial p}{\partial x_i} + \frac{\partial}{\partial x_j} \underbrace{\mu \left(\overbrace{\left(\frac{\partial v_i}{\partial x_j} + \frac{\partial v_j}{\partial x_i} \right)}^{s_{ij}} - \frac{2}{3} \frac{\partial v_k}{\partial x_k} \delta_{ij} \right)}_{\tau_{ij}} \tag{2.16}$$

$$\frac{\partial \rho h}{\partial t} + \frac{\partial (\rho h v_j)}{\partial x_j} = \frac{\partial p}{\partial t} - v_j \frac{\partial p}{\partial x_j} + \tau_{kj} \frac{\partial v_k}{\partial x_j} + \frac{\partial}{\partial x_j} \left(\frac{\mu}{Pr} \frac{\partial h}{\partial x_j} \right) \tag{2.17}$$

This uses Einstein summation with the j and also k as indices. Obviously, equation (2.16) is a vector equation and can be expressed as a set of equations for every Cartesian direction i of the required solution.

The PDEs above are written to suit the analysed problem - the momentum equation involves f_i as the body forces acting on the fluid, which is less common in general aerodynamics but is needed for the moving reference frame cases. The influence of volumetric viscosity on momentum is neglected, the respective term is not presented at all.

It is also common in further manipulations, that the terms containing pressure p in the energy equation are omitted because of their low impact on the temperature field in flows dominated by convective, inertial and heat diffusion effects. The third term on the right hand side - the viscous heating source - is also dropped for all the simulations presented in this work.

The ideal gas law $p = \rho r T$ and the expression of specific enthalpy $h = c_p T$ and Prandtl number $Pr = c_p \mu / \lambda$ are some of the constitutive relations closing the system of equations. There are various valid ways to express c_p, λ, μ, which are influenced mostly by gas temperature, but they can also be modelled as constants under the conditions appearing in this work.

2.4.1.1 Incompressible flow

For incompressible flow, the ρ is constant and could be factored out of the partial derivatives and cancelled out by dividing both sides of the equations by it. The energy equation then becomes obsolete for adiabatic system analyses and the time partial derivatives of density in equations (2.15) and (2.16) equal zero, even for transient cases. Also, the second part of the viscous term (the last one) of the equation (2.16) diminishes as a consequence of zero deviation of the velocity flow field in incompressible flows.

2.4.2 Solution methods

The exact governing PDEs were presented above, but it is not possible to achieve analytical or numerical solution of these equations for any practical problem except a very few simplistic canonical flow examples. The problem is that the temporal and spatial scales of the fluid movements are so small and detailed, that an analytical solution is impossible and direct numerical simulation is not feasible at best, even using the top-tier supercomputers of today.

There are more workarounds available in numerical simulation methodology - all involve modelling the smaller scales of turbulent motion to account for the turbulent transport of momentum and energy.

The briefly mentioned LES filters out the small scales from the basic equations and adds the contribution of the filtered part via the sub-grid scale turbulence model.

A more simplifying statistical approach is to solve for time-averaged dependent quantities from the PDEs [23]. The remaining fluctuating parts of these quantities form additional terms in momentum and energy equations.

2.4.2.1 Reynolds-averaged Navier-Stokes equations and turbulence modelling

For compressible flow, the averaging is not trivial, as some quantities are averaged according to Favre's method of mass weighted averaging to eliminate the terms involving density fluctuations. Some more terms can be neglected if they contain a product of three fluctuation variables rather than two, or are generally safe to be assumed to be of a few orders of magnitude lower than the others.

In the **momentum conservation equation**, the remaining fluctuation term is the *Reynolds stress tensor*, which can be modelled directly or it can be first simplified by the Boussinesq assumption of isotropy, which reduces the unknown from a symmetrical tensor to a scalar and uses this scalar analogically to molecular viscosity - creating *the turbulent (or eddy) viscosity* μ_t, see equation (2.18) [23].

$$\tau_{ij}^t = -\overline{\rho v_i' v_j'} = \mu_t \left(\frac{\partial \overline{v_i}}{\partial x_j} + \frac{\partial \overline{v_j}}{\partial x_i} \right) - \frac{2}{3} \overline{\rho} \delta_{ij} k \tag{2.18}$$

Using dimensional similitude, it was concluded that it would make sense to express it as a function of turbulent time and length scales - in fact, the product of these two. The scales can then be modelled using algebraic equations using mean flow variables as input and/or using one or more transport PDEs for turbulent quantities. The eddy viscosity models with two-PDE construction became the most applied method for reasonably accurate and feasibly demanding engineering flow simulations including turbomachinery flows.

The pinnacle of the development of such models is the k-ω SST (shear stress transport) turbulence model, which is further described in paragraph 2.4.2.2 [24, 25].

University of West Bohemia, Faculty of Mech. Engineering   Dissertation thesis 2022/23

Department of Power Systems Engineering   Ing. Lukáš Hurda

The averaged **energy conservation equation** requires modelling of the turbulent heat transfer. A hypothesis similar to the Bousinesq approximation of μ_t is used:

$$-\overline{\rho v_i' h'} = \frac{\mu_t}{Pr_t}\frac{\partial \widetilde{h}}{\partial x_i} \tag{2.19}$$

Most often, the turbulent Prandtl number is modeled as a constant, $Pr_t \in \langle 0.85, 0.9 \rangle$. This simple assumption is sufficient even in conjunction with complex turbulent viscosity or Reynolds stress models. The relation for the turbulent heat transfer also involves μ_t, so the quality of the turbulent heat transfer model is usually as good as the specific model for turbulent viscosity.

2.4.2.2 k-ω SST **turbulence model**

This model, together with proper time and space discretization, is capable of capturing most of the important features of complex 3-dimensional flows including massive boundary layer separations, unlike the algebraic and the 1-eq. models, and without some drawbacks in the accuracy of earlier 2-eq. models.

When looking into more subtle nuances of turbulence influenced features such as near wall heat transfer or other phenomena, where the anisotropy of the turbulence plays a role, the non-linear eddy viscosity models such as the $v2$-f model can be more precise and if proven otherwise, only the Reynolds stress models (RSM) or the LES could be more useful.

The original k-ω of Wilcox was modified numerous times to enhance performance and a major revision by the original author of the SST variant, Menter, was made in 2003 [26]. This version is the current one used by most CFD codes including the ones used by the author and it is presented here. The specific turbulent viscosity is formulated as

$$\nu_t = \frac{a_1 k}{\max\left(a_1 \omega, SF_2\right)}, \tag{2.20}$$

where $S = \sqrt{S_{ij}S_{ij}}$ is the invariant measure of strain rate, F_2 is the blending factor and a_1 the calibrated constant.

The transport quantities are here the *turbulent kinetic energy* $k = 1/2\overline{\rho v_i' v_i'}/\overline{\rho}$ and the *specific turbulent dissipation rate* $\omega = \varepsilon/k$. Here, the turbulent dissipation rate ε is defined from equation (2.21)

$$\overline{\rho}\varepsilon = \mu\overline{\frac{\partial v_i}{\partial x_j}\frac{\partial v_i}{\partial x_j}} \tag{2.21}$$

The transport equations for turbulent quantities involve another blending factor, a production rate limiter and a large number of calibrated constants. The blending allows "switching" of the approach between k-ω in the wall boundary layers and k-ε in the freestream. This is to avoid the initial condition sensitivity of the original k-ω model invented by Wilcox.

University of West Bohemia, Faculty of Mech. Engineering   Dissertation thesis 2022/23

Department of Power Systems Engineering   Ing. Lukáš Hurda

In engineering practice, it is quite common to employ *wall functions* allowing for coarse meshes in the boundary layers (see the concept of the mesh in paragraph 2.4.2.3). Wall adjacent cell height[3] at $y^+ \in \langle 30, 200 \rangle$ is then low enough. On the contrary, the small size and low geometrical complexity of the presented cases allowed the author to take advantage of the increased boundary layer modelling accuracy of the low turbulent *Re* variants of the discussed turbulence model. Then, one should keep the viscous sublayer discretized, which tightens the y^+ requirement to optimally < 1 or < 10 while using `Fluent` hybrid wall functions.

2.4.2.3   Time and space discretization

Finite volume method (FVM): All the used solvers follow the FVM. It is based on the Eulerian convention of tracking the moving fluid relative to the discreet computational cells of a continuous mesh, which occupies the whole volume of the fluid domain. The mesh has a frame of reference, which may be static or in a predefined movement. All the solved physical quantities are stored in the cell centroids in the presented simulations. This is called the *collocated* arrangement.

Computational mesh: Although it has become common to use highly automated unstructured meshing algorithms using methods such as polyhedral, hex-core or different meshing including sophisticated methods of boundary layer discretization, in turbomachinery, *hexahedral block-structured meshing* remains the most effective method of dividing the computational domain into finite volume cells.

It is undoubtedly superior, especially in the presented cases of centrifugal compressors including shrouded impellers with no tip clearance, no rotor seals or other secondary flow paths and also no bevels or chamfers in the hub/shroud-to-blade joints. Even the blades of rather uniform thickness and short span with curvature mainly directed along the meridional direction (typical for radial machines) make for an easy job of the meshing programs with predefined sets of blocking topology. The degree of automation is also very high, and due to the logical simplicity of block-structured meshes, the computer programs generate the outputs very fast and are therefore convenient to work with. Two approaches using two different programs were used:

- The bladeless channel presented in section 3.4 was meshed using general purpose program `gmsh`. This software tool is easily controlled by user scripts. Unlike most modern programs, the process of meshing is preceded by geometry definition within the program itself. As the cases are topologically identical and very simple, the whole process of defining the channel contour, constructing the blocks and dividing them into cells of desired distribution was automated from the user side. The procedure is very similar for both axisymmetric 2D and 3D.

---

[3]$y^+ = \sqrt{\tau_w \rho} \zeta / \mu$, where ζ is the wall-normal coordinate and τ_w is the wall shear stress magnitude. When estimating the required first mesh cell layer height, ζ is equal to half of the height - the wall distance of the cell centre - and τ_w needs to be estimated with appropriate empirical relation with respect to the expected flow velocity of the flow core away from the wall. It is common to use the relation for fully developed turbulent flow along a flat plate [27]: $\tau_w = 1/2(2 \log_{10} Re - 0.65)^{-2.3} \rho v^2$

- The `Ansys TurboGrid` program is a specialized tool for turbomachinery CFD meshing. It takes hub, shroud and blade profile curves as geometry input. The fineness of the mesh can be defined by setting the estimate of the Reynolds number of the flow inside the domain and the dimensionless height of the first wall-adjacent cell y^+ for boundary layer discretizations. Together with the setting of desired expansion factors (the coefficients of geometric series of cell dimension increment in the direction from the wall outwards) an appropriately fine mesh can be generated. This procedure was carried out to generate meshes presented in sections 3.5 and 3.6 and subsection 3.6.5.

The spatial numerical schemes are needed for cell-to-face interpolations and integration of the spatial and temporal derivatives in the solved PDEs.
Cell-to-face interpolation is carried out with a simple linear scheme in `OpenFOAM` and in `Fluent`, the least squares cell based scheme is used.
All the advective terms, which present the largest challenge for the schemes to balance accuracy and stability, are discretized by second order accurate upwind biased or central schemes. Bounding and limiting of the schemes to prevent instability due to mesh non-orthogonality is employed.

Pressure and velocity coupling in the pressure-based solvers means the method of expressing the pressure field from the appropriately modified continuum equation and ensuring the pressure field satisfies the momentum equation. As the equations are linearized over the dimension of the finite volume cell, they are then solved by a chosen type of linear system solver, for example, the algebraic or geometric multigrid methods.
`OpenFOAM` only implements segregated solvers, so a classical *SIMPLE (Semi-Implicit Method for Pressure-Linked Equations)* involving predictor and corrector steps is utilized. It uses the Poisson equation explicit for pressure as a form of continuum equation. The linear system solver treats the linearized equations separately during the mentioned steps within every iteration.
`Fluent` implements a very stable and well converging *Coupled* pressure based solver. The implicit expression of the pressure gradient in the continuum equation allows the construction of a compact set of 4 linearized equations (3 components of the vector momentum equation plus the continuity equation), which can be solved together by the linear system solver.

Time discretization differs between `OpenFOAM` true steady state, where time derivatives vanish [28], and pseudo-time method for steady state selected in `Fluent` [29]. It is used in the form with a global timestep size. It is practically an under-relaxation technique [30].
Only true time discretization was needed for the transient simulations carried out. An implicit scheme was selected.

2.4.3   Boundary conditions

The solution of a PDE system of Navier-Stokes equations requires a proper set of boundary conditions (BCs) for all of the bounding surfaces of the fluid domain - solid walls (hub, shroud, IGVs, rotor blades), a pair of tangential periodic surfaces, inlet and outlet. There, all of the variables of the PDEs need to be defined - pressure, velocity, temperature (to express enthalpy in compressible cases) and turbulent variables k and ω. The basic types are explained below. The special treatment of multi-domain compressible simulations with a moving impeller required for models from section 3.6 and subsection 3.6.5 is further explained in subsection 2.4.5. These cases also require special care with the combination of inlet and outlet boundary conditions because of the impeller, which acts as a momentum source interacting with these BCs. This issue is addressed in subsection 2.4.4.

Solid walls allow *no slip* of the fluid along the surface and, of course, no penetration. Velocity BC is then defined such that the wall-face value of the wall-adjacent cell is equal to zero in all 3 vector components, relative to the solid wall (while minding the moving walls).
With such a strong constraint on the velocity, the pressure can be defined as having a zero gradient in a wall-normal direction.
Turbulent quantities k and ω can be expressed algebraically in the viscous and inertial sublayers using only constants and easily obtained local values like the molecular viscosity and wall distance. Having a cell spanning above the log-layer threshold is unlikely for the presented cases, but even such a case is no problem for the boundary condition supplementing near-wall treatment algorithms implemented in both `OpenFOAM` and `Fluent`. In such case, zero wall-normal gradient for k is applied and the transport equation is solved down to the wall-adjacent cell. Values are obtained at the cell centre and extrapolated to the wall-adjacent face of this cell in all cases.
All the wall heat transfer is suppressed by the adiabatic wall condition as the machine operation is considered adiabatic and the heat transfer has a very low chance of affecting the flow pattern and momentum transfer in the inertia dominated flow inside a turbomachine. The adiabatic effect is achieved by the zero wall-normal gradient of temperature.

Rotational periodic surfaces are constructed at the tangential limits of the 3D computational domains as only one or a few interblade channels are simulated most of the time. The remaining channels can be often considered to have nearly identical flow patterns. This BC is principally very simple - it consists of two sides of an identically shaped surface offset by a certain angle, for one interblade channel equal to $2\pi/(blade\ count)$. The cells adjacent to one side of this surface become the neighbours of the cells in the tangentially shifted location on the other side of the periodic surface. This surface then acts as a virtually continuous mesh and requires no special treatment of any variable.
Throughout this thesis, only conformal periodics are constructed. These introduce no errors thanks to the absence of the otherwise necessary interpolations between non-conformal faces on either side of the periodic. Such an approach is practically reserved for cases where

difficulties in the meshing process occur and one is not able to define the mesh on both sides as identical. This is not the case for the used meshing techniques - in `gmsh`, one of the surfaces is meshed in 2D and the 3D mesh (including the one-layer mesh for the axisymmetrical 2D) is constructed by rotational extrusion of the cell layers. `Turbogrid` follows the traditional turbomachinery meshing techniques and its predefined block topologies are all created as conformally periodic. The program even shapes the periodic surface not only to wrap the mesh around the blades but also to optimize the shape of the domain for minimum possible mesh skewness.

`OpenFOAM`'s **wedge** type BC is a special case of the periodic BC for 2D axisymmetric cases. As this CFD package only works with 3D meshes, 2D cases are solved using one-layer meshes. Axisymmetric simulations allow the third velocity component - the tangential one - to be simulated in a case, which is technically defined in 2 dimensions.

Inlet BC is, generally speaking, the surface at which the flow is expected to enter the domain. At such a surface, all variables are prescribed by their absolute value (Type 1/Dirichlet BC) with the exception of either the pressure or the velocity. In the compressible flow, it is also necessary to consider the dynamic component of pressure and temperature - total state parameters are prescribed. Also, with a variable density, it is not usual to prescribe the velocity field, but to calculate it from the desired mass flow rate. Inlet types used:

- Velocity inlet - the only option for incompressible simulations, see subsection 2.4.4. Normal to boundary or with components specified in cylindrical coordinates to introduce IGV swirl effect into simulations where IGVs are not present in the model.

- Mass flow inlet - the modified velocity inlet for compressible cases. The total mass flow rate is prescribed and the uniformly distributed mass flux is kept constant across the inlet surface along with the velocity vector direction. The magnitude of the velocity is adjusted based on the solved value of density inside the domain to match the mass flux.

- Pressure inlet - the total pressure along with flow direction is set. There is no direct control of the mass flow rate. As the inward direction of the flow is not guaranteed by this BC, it is possible to employ an algorithm to prevent the reverse flow by locally switching the boundary mesh faces to wall BC.

Outlet BC does not need the quantities prescribed as long as the flow is leaving the domain, extrapolation to the boundary faces is performed by the zero boundary-normal gradient condition. Again, one of the pressure-velocity pair needs to be an exception to this statement.

- Pressure outlet - the more typical BC sets a fixed value to the static pressure at the outlet surface.
  As backflow can occur, a few different options are available to deal with it. It can be blocked by local face switching to a wall or the inflow conditions have to be specified. In the case of an unknown backflow velocity direction, computing it from the

University of West Bohemia, Faculty of Mech. Engineering　　Dissertation thesis 2022/23

Department of Power Systems Engineering　　　　　　　　　　Ing. Lukáš Hurda

boundary neighbouring cell seems to introduce the smallest error possible.
`Fluent`'s implementation of this condition also allows relaxation of the pressure value
requirement and enables the algorithm to adjust it in between steady solution itera-
tions to obtain the *target mass flow rate.*

- Mass flow outlet - only the boundary normal velocity component gets set by the
  prescribed mass flow rate, other components are extrapolated from the inside of the
  domain.

2.4.4　Inlet and outlet setup in turbomachinery

Compressible turbomachinery CFD simulations - the scope of this chapter - are somewhat
special cases due to the fact the domain always involves massive momentum source/sink
and most, if not all, of the fluid passing the domain flows through this region - the rotor.
It is also often not practicable to place the inlet and outlet boundaries far enough from
the regions of most interest to cancel their influence on the results. A few combinations of
the inlet and outlet boundaries introduced in subsection 2.4.3 are offered:

- Pressure inlet - mass flow outlet: The most convenient combination as the inlet gas
  state is usually known. The desired operational point is defined precisely by the mass
  flow rate at the outlet, where other parameters are not easily evaluated a priori. The
  enforcement of mass flow rate at the outlet is however far away from the physical
  reality as the direction of the velocity vector gets adjusted artificially. This may
  present a deterioration of the results in the proximity of the boundary. It naturally
  prohibits the occurrence of backflow through the outlet.

- Mass flow inlet - pressure outlet: Imposing the flow direction at the inlet is much
  more favourable than adjusting it at the outlet. The downside of this approach is
  that the fluid state at the inlet is not guaranteed and if it goes too far off, it might be
  unrealistic or worse - cause a solver crash. It proves to work well in regions close to
  the choking limit of the compressor - at higher flow rates. The outlet pressure needs
  to be estimated and the target mass flow rate algorithm is not easily applicable as
  such a strongly constrained system tends to be unstable - the outlet pressure often
  fails to stabilize.

- Pressure inlet - pressure outlet: The most natural conditioning of a compressor - the
  flowrate is the result of balancing the energy input and the fluid energetic potential
  increase specified by the pressure rise. There is no direct control over the flowrate
  unless the target mass flow rate through the outlet is specified.

The pressure outlets have some more detailed settings to discuss. First, there is an option of
specifying total pressure instead of the static one. `Fluent` always internally prescribes the
static pressure at outlets, but when total pressure is specified, the approach is effectively
switched from uniform value to a profile computed from the supplied total pressure and
the velocity magnitude and density fields at the outlet.

2.4.5   Moving reference frame and mesh interfaces

The insides or even some close surroundings of moving solid parts in CFD simulations are usually discretized by a sub-domain separate from the static mesh in the adjacent surroundings. *Moving reference frame* (MRF) is applied in these sub-domains to cancel the round-off errors of floating point numbers stored in the computer memory when the absolute velocity of solid part movement is large compared to the relative velocity of the fluid to the solid part. Rotational MRF is convenient for turbomachinery. The movement is not prescribed explicitly so in a steady state simulation, the coordinates of the mesh nodes remain constant, velocity is stored in the MRF and the wall boundary velocities are most typically set to also be relative to the MRF.

Interfaces are needed to connect two sub-domains which have a different frame of reference. Turbomachinery-specific types of mesh interfaces have been developed over the years since there are some more specialities to this field such as periodic treatment of interblade channels, non-conforming numbers of blades/vanes and/or number of simulated interblade channels in the adjacent rotor and stator parts of the machine. Such an interface is called a generalized turbo interface (GTI), generalized grid interface (GGI) or similar.

All generalized interfaces are non-conformal and therefore it is preferable to avoid them whenever it is feasible to construct a conformal interface. This is usually possible for the rotor to vaneless diffuser interface or an inlet channel with no vanes to rotor interface. In other cases, the use of a generalized interface is mostly inevitable.

There are several options to treat the non-conformal interface:

- The **mixing plane** applies tangential averaging of flow variables across a finite number of bands spread along the meridional span of the interface. This effectively reduces the interface to one dimensional field, which can be spread over the receiving side of the interface of any pitch.

- The **no-pitch-scale interface**, as named in `Fluent` is similar to the better known *frozen rotor* implemented in `ANSYS CFX`. It interpolates the fields from one side of the interface to the other with respect to their current relative position in space (which is constant in steady state simulations). When the sides are not overlapping completely, it creates a virtual copy of the periodic segment at the next pitch instance and continues the process described earlier.

- The **pitch-scale interface** uses the tangential bands as a mixing plane, but it does not apply averaging, but rather stretches and spreads the flow fields to the required pitch of the receiving side of the interface.

As using the mixing plane leads to a loss of information about IGV wakes and other flow features, which are not pitchwise-uniform, it was excluded from the presented analyses.

The performance of the two remaining generalized interfaces is discussed in section 3.6.

3 Modelling and results

3.1 Inlet channel flow dimensional analysis

The goal of this model is to construct the simplest description of the geometry and flow with the least parameters possible. This model, later analysed using CFD (see section 3.4), should still be capable of reproducing the expected phenomenon of flow separation at the inner side of the annulus (the side closer to the machine axis). The dimensional analysis serves to delineate the geometric and flow parameters for parametric study design and resulting data generalization.
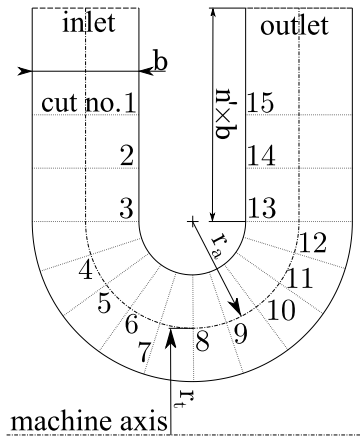
Figure 3.1: Bladeless channel geometry (meridional section). Shown including meridian-normal profile surfaces (stations) used for CFD post-processing.

The simplification of the geometry consists, in addition to omitting the IGVs and rotor blades, in substituting the often complex curves defining the toroidal channel profile of real compressors with parallel lines and concentric circles, as shown in Figure 3.1. The number of geometric parameters of the channel can thus be reduced, for example in one of the following ways by one characteristic length to project into the flow criteria and two geometric simplexes:

- b Constant channel width

- $R_t = r_t/b$ Ratio of the channel meanline tangential (pitchwise) radius at bend apex to the channel width

- $R_a = r_a/b$ Ratio of the axial channel bend radius to the channel width

Furthermore, the hub and shroud wall rotations are neglected. The channel is prolonged in the radial direction for the purpose of proper definition of CFD BCs, but the prolongation length does not affect the analytical approach presented in this chapter.

The geometrical similitude is guaranteed by R_a and R_t and the length scale b is, when necessary, used as the only one dimensional parameter to let the dimensionless system of criterion values give real values to all the dimensioned parameters. The analysis can continue step by step - when new influences and physical quantities are added to the considerations, one can work with the already defined parameters and apply the Π-theorem again. The only extra rule to this procedure is that dimensions, which have already been used for reduction cannot be subtracted from the number of variables again.

3.1.1 Incompressible flow in the inlet channel

Flow through the given geometry (R_a, R_t) is fully characterized by the absolute velocity magnitude $c \ [m/s]$ (evaluated in the channel bend apex), the swirl angle $\alpha \ [1]$, the kinematic viscosity $\nu \ [m^2/s^2]$ and possibly the turbulence intensity of the inlet flow $I \ [1]$. As the description of incompressible flow is fully kinematic, the influence of the fluid density is zero.

This constellation of the 6 variables only has 2 dimensions: length and time, but the length was already used in the geometric similarity reduction, so only time can be subtracted from the number of variables. The flow could be described using 5 dimensionless parameters. R_a, R_t, α^4, I are already dimensionless. Let the classical $Re = cb/\nu$ as the fifth dimensionless group be introduced.

It is questionable whether criteria of the centrifugal forces [31] ought to be considered or not. The trigger of the boundary layer separation clearly lies in the balance of two inertial forces of this kind. One of them arises from the turning of the flow observable in the meridional plane and therefore directed to the machine axis. The other one is created by the tangential swirl and points away from the machine axis. The criteria specific for the two superimposed rotations are constructed in equations (3.1) and (3.2). They are not further considered for the determination of a similar flow state, as they are dependent on the previously listed criteria only.

$$Ce_a = \frac{\Omega_a r_a b}{c^2} = \frac{c_a^2 b}{r_a c^2} = \frac{b}{r_a} \frac{c_a^2}{c^2} = \frac{\cos^2 \alpha}{R_a} \tag{3.1}$$

$$Ce_t = \frac{\Omega_t r_t b}{c^2} = \frac{c_t^2 b}{r_t c^2} = \frac{b}{r_t} \frac{c_t^2}{c^2} = \frac{\sin^2 \alpha}{R_t} \tag{3.2}$$

---

[4]Under ideal conditions, considering no disturbances to the flow field, the swirl angle α should remain constant throughout the channel. This could be derived from the continuity equation for the incompressible flow.

A similar procedure with the same results is undertaken with the Strouhal number for the kinematic similarity. The frequency is expressed for both types of rotation around machine axis and annular bend axis. Both criteria are again dependent on those previously listed and do not need to be considered.

$$Sh_a = \frac{t}{c}f_a = \frac{t}{c}\frac{c_a}{\pi R_a t} = \frac{\cos\alpha}{\pi R_a}, \qquad Sh_t = \frac{\sin\alpha}{\pi R_t} \tag{3.3}$$

Centrifugal force criteria can be used to express the critical flow swirl angle for a given channel geometry. The critical value is reached when the centrifugal forces are balanced, i.e. the two $Ce_a = Ce_t$ are equal. At that point, the dominance of the two centrifugal forces is reversed. The cosine dependent Ce_a is dominant at $\alpha < \alpha_{crit}$, Ce_t takes over at higher swirl angles. The relation of the critical swirl angle to the possible occurrence of boundary layer separation in the channel will probably be indirect, but it can still be used to assess the properties of the respective channel geometries. Putting the right hand sides of equations (3.1) and (3.2) into equality and substituting α_{crit} for α yields

$$\alpha_{crit} = \tan^{-1}\sqrt{\frac{R_t}{R_a}}. \tag{3.4}$$

The results of equation (3.4) on selected intervals of R_a, R_t are shown in Figure 3.2.

The geometric simplexes of all the geometries analysed later are summarized here (approximate for real compressor geometry):

- Simplified channel initial analysis: $R_a = 1.00; R_t = 1.00; \alpha_{crit} = 45.00°$

- s2 stage: $R_a = 0.76; R_t = 1.49; \alpha_{crit} = 54.47°$

- s4 stage: $R_a = 1.80; R_t = 2.53; \alpha_{crit} = 49.85°$

- u4 stage: $R_a = 1.50; R_t = 2.50; \alpha_{crit} = 52.24°$
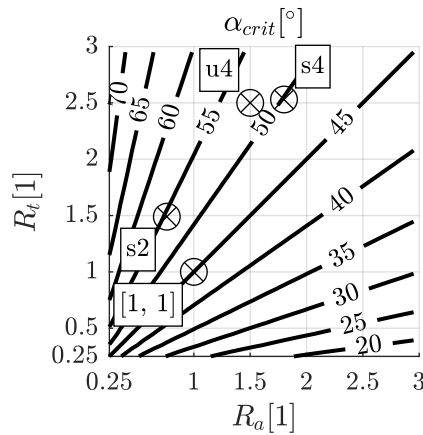
Figure 3.2: Critical flow swirl angle.

University of West Bohemia, Faculty of Mech. Engineering   Dissertation thesis 2022/23

Department of Power Systems Engineering   Ing. Lukáš Hurda

3.1.2   Compressible flow in the inlet channel

When compressibility is introduced into the model outlined in subsection 3.1.1, the number of variables increases. For reasonable simplicity, a perfect gas is considered - the thermodynamic behaviour of such a gas is determined by:

- specific heat ratio $\kappa = $ const. [1],

- specific gas constant $r = R/M = const.$ $[J/kg/K = ms^{-2}K^{-1}]$.

The specific state of the gas is fixed by two independent state parameters, lets select:

- density ρ $[kgm^{-3}]$,

- temperature T $[K]$.

In perfect gas theory, adopting no empirical models, thermophysical properties are mostly defined using the above mentioned variables, with the exception of the already involved ν and

- thermal conductivity λ $[J/s/m/K = kgs^{-3}K^{-1}]$.

The other important, but **dependent** parameters are then expressed:

- pressure $p = \rho r T$ from the perfect gas equation,

- isobaric heat capacity $c_p = \kappa r/(\kappa - 1)$ from Meyer's relation and κ definition,

- dynamic viscosity $\mu = \nu \rho$.

5 new independent variables were found on top of the 5 parameters of the incompressible flow, which are already dimensionless. 2 new dimensions, mass and temperature, were introduced to the system. $5 - 2 = 3$ new dimensionless groups should be found to close the system.

- κ is already dimensionless.

- $Ma = c/a = c/\sqrt{\kappa r T}$, the Mach number is a traditional criterion for flow compressibility justification via comparison of the flow velocity to the speed of sound a.

- $Pr = c_p/(\mu \lambda)$, the established Prandtl number bounds the thermophysical properties.

The Prandtl number is clearly a material property. It is nearly constant across a wide range of states of certain gases and also it might not gain significantly different values for many gases similar to air. It is common to use a constant value of the Prandtl number as a model to evaluate λ, given κ, r, T, μ.

It is a ratio of the diffusion of thermal energy to the diffusion of momentum. As thermal diffusion effects are mostly negligible in turbo-compressor flow, the Prandtl number is considered to have no significant influence on the parametric study and it is not treated further as an independent parameter for which a range of values would need to be analysed.

A much more important fluid property for a turbomachine is the κ. The value of r is significant but less important, plus it is loosely bound with κ.

3.1.3 Conclusions of inlet channel flow dimensional analysis

Dimensional analysis was used to provide the most generalized description of the compressor inlet channel model possible. It is not defined on an exact real life geometry, so it should be applicable to any compressor with a similar inlet channel arrangement. Care needs to be taken when approximating the geometrical parameters - one has to be aware that the most suitable location to take the measurements is the compressor inlet eye - the bend apex.

This strong point of geometrical simplicity is also the largest pitfall of this method: the description does not account for sophisticated meridional velocity magnitude development along the channel length, which real machines usually feature. The streamwise pressure gradient distribution due to flow area changes can differ significantly between designs seeming similar at first glance. However, while it is typical that the channel width decreases in the streamwise direction, further modelling of the simplified geometry should be on the safe side, as the constant width will always have stronger diffusive effects in the aft part.

This method completely ignores the presence of the impeller so the operational parameters are not dependent on its rotational speed or any other property. It was developed for the analysis of the interaction of the inlet channel and IGVs with the impeller with the most simplifying assumptions. It allows later comparisons with measurements and calculations.

This system of criteria was used to define CFD parametric studies discussed in section 3.4. The compressible case already has many parameters, so the question arises if valuable results cannot be obtained with just the incompressible model. The answer is given in subsection 3.3.2.

3.2 Expected relative flow angle at rotor leading edge

Before looking into the results of measurements and constructing numerical simulation cases, an insight into what results could be expected is provided by much simpler approaches, with limited accuracy. A zero dimensional numerical experiment is constructed to evaluate the relative flow angle at the rotor leading edge (LE). The test bed compressor geometry is considered by using the respective station flow area, leading edge coordinates and the parameters of IGVs. The whole apparatus was scripted within `MATLAB`.

3.2.1   Inlet guide vane stagger angle versus outlet angle

For a symmetrical aerofoil, i.e. for a profile with a straight camber line, in a planar space, the stagger angle ϑ is equal to both incidence i_{IGV} and outlet (α'_{2IGV}) angles. This applies to an isolated wing as well as to circumferentially arranged cascades with axial throughflow (always measuring stagger angle from incoming flow direction). In radial arrangement, however, the angles are not the same anymore, as seen in Figure 3.3.

When the profile is rotated about a pivot arbitrarily placed somewhere along the camber line, the resulting shift in the angular coordinates of the leading and trailing edges implicates the need to measure the incidence and outlet angles from different radial rays as opposed to the ray going through the pivot used for profile manipulation. Unless the pitch circle of the cascade is not very large compared to the chord length of the airfoil, the difference in these angles is significant.

Radial IGVs are made of a set of symmetrical, prismatic airfoils in a portion of a radial channel of uniform width. Each one is mounted on a pivot linked together with all the others to always turn the same angle all at once. This is valid for the discussed test bed compressor and there are not many sensible modifications to this arrangement. The vanes are relatively thick and large in number. This is to provide robust flow guidance even in the case of large incidence angles. IGVs owe this to the properties of the airfoil profile and the fact that as the stagger angle increases, the pitch to (radial) chord ratio increases, making the cascade effectively denser. As a side effect, the channel blockage increases gradually up to the extreme point where the neighbouring vanes touch each other and the channel is practically closed.

The difference in inlet angle is expressed using trigonometry in Cartesian 2D coordinates established in a plane normal to the machine axis displayed in Figure 3.3. c_{TE} is the part of the chord from the pivot point to TE and r_p is the pivot pitch circle radius (shown dash-dotted).

$$\Delta x_{TE} = c_{TE} \sin \vartheta \tag{3.5}$$

$$\Delta y_{TE} = c_{TE}(1 - \cos \vartheta) \tag{3.6}$$

$$\Delta \alpha_{IGV} = \tan^{-1} \left(\frac{\Delta x_{TE}}{r_p - c_{TE} + \Delta y_{TE}} \right) \tag{3.7}$$

The actual values of α'_{2IGV} for a set of stagger angles, given the analysed compressor geometry, can be found in Table 1.

3.2.2   Parametric numerical experiment and similitude

The desired output is the LE incidence angle dependent on the inlet flow swirl angle, impeller rotational speed and mass flow rate. Air at atmospheric conditions is taken as the

Figure 3.3: Radial IGVs cascade geometry

Table 1: IGVs outlet metal angle.

IGV stager angle	ϑ	15°	30°	45°	60°	75°
IGV outlet metal angle	α'_{2IGV}	19.876°	39.065	57.120°	73.900°	89.477°

inlet fluid stagnation state. The flow Mach number at LE can be evaluated as a secondary output.

Considering the previously discussed dimensional similitude topics (paragraph 2.2.3.1 and section 3.1), it is clear that the flow rate can be substituted with the flow coefficient and it also contains information about rotational speed. However the later ascribed model of the flow from IGVs to the rotor is dependent on the absolute flowrate, so the blade Mach number needs to be added for completeness. While it is defined by the inlet gas total state, it allows us to distinguish the behaviour of the flow incoming to rotor LE at different flowrates, but gives the same flow coefficient values due to reciprocally shifted rotational speed.

This connects the description of the bladeless inlet channel with the compressor duty, but only the impeller inlet state, so no description of the compression itself is involved.

The flow is assumed to be compressible with presumed approximations applied of IGV flow deviation angle and total pressure losses. The first is defined in absolute values increasing with the stagger angle and the latter is defined by constant loss coefficient multiplied by the resulting dynamic pressure.

Using the rotor LE flow coefficient as an input to later evaluate mass flow would generally be beneficial as it takes away the necessity of iterating over the reciprocal dependence of the fluid static state and flow velocity in that station. A range of mass flow rates and a set of rotational speeds has to be used in this case, because the iterative approach is necessary - two stations need to be considered.

First, the static state at the IGV outlet ($2IGV$) is examined, and then the static state at the impeller inlet (1) is assessed. These stations are assumed to be cylindrical or frustum-conical, so their flow areas are expressed generally as $A = 2\pi r_m b$, where r_m is the station mean radius and b the channel width measured perpendicular to the flow direction. Besides the effects of density decrease due to flow area reduction/velocity increase, the conservation of angular momentum is addressed.

The swirl angle is dependent on the channel width development and density change between stations, as derived from the following observations:

The meridional velocity component depends on the flow area ratio between the two stations and the density ratio, while the tangential component changes just with the ratio of the mean radii in the same two stations (equation (3.10)). For the meridional component:

$$G = \rho A c_m = \text{const.} \Rightarrow \quad \frac{c_{m1}}{c_{m2IGV}} = \frac{\rho_{2IGV}}{\rho_1} \frac{A_{2IGV}}{A_{m1}} = \frac{\rho_{2IGV}}{\rho_1} \frac{r_{2IGV}}{r_1} \frac{b_{2IGV}}{b_1}. \quad (3.8)$$

The tangential component is derived considering a control volume bounded by the channel walls and the two stations in question. Assuming no torque acting on the fluid (including no friction torque), a form of the Euler turbomachinery equation [6] can be written as in equation (3.9), where $dG = \rho c_m dA$. Equation (3.10) gives c_{t1} after substituting for the

ratio of meridional velocities from (3.8) into (3.9).

$$\int\limits_{\{A_{2IGV},A_1\}} rc_t dG = 0 \Rightarrow \frac{c_{t1}}{c_{t2IGV}} = \frac{r_{2IGV}}{r_1} \frac{\rho_{2IGV}}{\rho_1} \frac{c_{m2IGV}}{c_{m1}} \frac{A_{2IGV}}{A_1} \tag{3.9}$$

$$c_{t1} = c_{t2IGV} \frac{r_{2IGV}}{r_{m1}} \tag{3.10}$$

$$\alpha_1 = \tan^{-1} \frac{c_{t1}}{c_{m1}} = \tan^{-1}\left(\tan \alpha_{2IGV} \frac{\rho_1}{\rho_{2IGV}} \frac{b_1}{b_{2IGV}}\right) \tag{3.11}$$

The throughflow of the axial bending of the channel and the momentum associated with it is neglected in this part.

In the uniform width channel from section 3.4, the swirl would remain unchanged throughout the channel for an incompressible flow.

It is also possible to take advantage of the simple perfect gas description and calculate fluid absolute velocity from a quadratic equation (3.13). This starts with the explicit expression for density from the total state parameters and the absolute flow velocity (applicable generally, therefore written without station subscripts):

$$\rho = \frac{p_s}{rT_s} = \frac{p_t - \rho c^2/2}{r(T_t - c^2/2/c_p)} = \frac{p_t}{rT_t + c^2 \frac{c_p - r}{2c_p}}. \tag{3.12}$$

Then it is possible to put the final expression of ρ from equation (3.12) into the expression of flowrate dependent on the meridional velocity component. Finally, the polynomial coefficients of c can be separated:

$$G = \rho A c_m \quad \Rightarrow \quad c = \frac{G}{\rho A \cos \alpha} \quad \Rightarrow \quad c^2 \frac{G(r + c_p)}{2c_p p_t A \cos \alpha} + c - \frac{GrT_t}{p_t A \cos \alpha} = 0. \tag{3.13}$$

The solution of the equation (3.13) usually yields two real roots, of which only one is positive, so the equation has one physically valid solution, as expected. Unfortunately, when the resulting velocity and density were used to evaluate meridional velocity, the cross-check of the resulting swirl angle failed. For large angles, but especially for large velocities (even in terms of the station $2IGV$), the calculation is not accurate - the meridional velocity computed as the cosine projection of the absolute vector does not satisfy the flowrate when using the computed density. This is believed to be a problem of the mathematical properties of the relations of velocity to state parameters and their evaluation using numbers in floating point notation within `MATLAB` program script. Further optimization is not worked since an iterative approach is necessary for station 1, but it might be very useful to have such an explicit relation in general 0D calculations of the compressible flow of perfect gas.

An attempt was also made to construct a general criterion equation in a power law form:

$$\beta_1 = C\alpha'^{e_1}_{2IGV} \Phi^{e_2} Ma^{e_3}_{1u}. \tag{3.14}$$

The coefficient and exponent values were to be found based on a regression of the numerical experiment results. The values of the input criteria are covered in a very wide range. It would be rare to find a machine operating in conditions lying outside of the analysed bounds.

However, as the data are produced on a single geometry case, the experiment would need to be administered again and new values of criterion equation constants will need to be found. As the simulation is zero-dimensional, only the basic geometry parameters need to be fixed: hub radius at LE, ratio of LE span to hub radius and quasi-orthogonal angle of the LE (180° for fully radial blade, 90° for fully axial impeller inlet). Theoretically, these geometrical criteria could be used to complete the equation (3.14) to be universal.

The results show, that the fitting of the data with the power law model usual for criterion equations might be applicable, but certainly not with a single set of fitted exponents and a coefficient. It would have to be divided into intervals to cover the response surface accurately. This would not only make the process quite laborious but also render the result less practical.

3.2.3   Results of the numerical experiment

Results are shown for the following ranges of operational parameters of the s4 stage:

- 2/6 to 3/2 of nominal mass flow rate G. This is close to the real operating range, but of course, it is not rectangular.

- Rotational speed of the impeller corresponding to s4 impeller outlet blade Mach number Ma_{2u} ranging from 0.5 to 1.1. Mach number at the rotor leading edge Ma_{1u} is evaluated too to keep this part of the analysis independent of the impeller parameters except for the inlet eye.

- Range of α_{2IGV} with respect to IGV stagger angle ϑ ranging from 0° to 60° - the deviation angle was subtracted from metal angle values outlined in Table 1. It was approximated as $\delta_{IGV} = -0.1\,\vartheta$. As the model presented in subsection 3.2.1 is not dependent on the channel flow as well as the deviation estimate, α_{2IGV} is chosen as a data display parameter to abstract from the specific IGVs design.

- Total pressure loss between the two stations is estimated by a loss coefficient $\xi = 0.1$ [1]. It was referenced to the dynamic pressure in station $2IGV$ and yielded values between few Pa to around $3.3\,\mathrm{kPa}$.

The results can be discussed using Figure 3.4. It cannot be safely said, which incidence angle is too high for the impeller to deal with, but it is a consistent criterion to assess an operating point.

The upper limit of the Φ values left of the global maximum would form the curve of constant maximum flowrate. It is curved upwards where flow compressibility and total
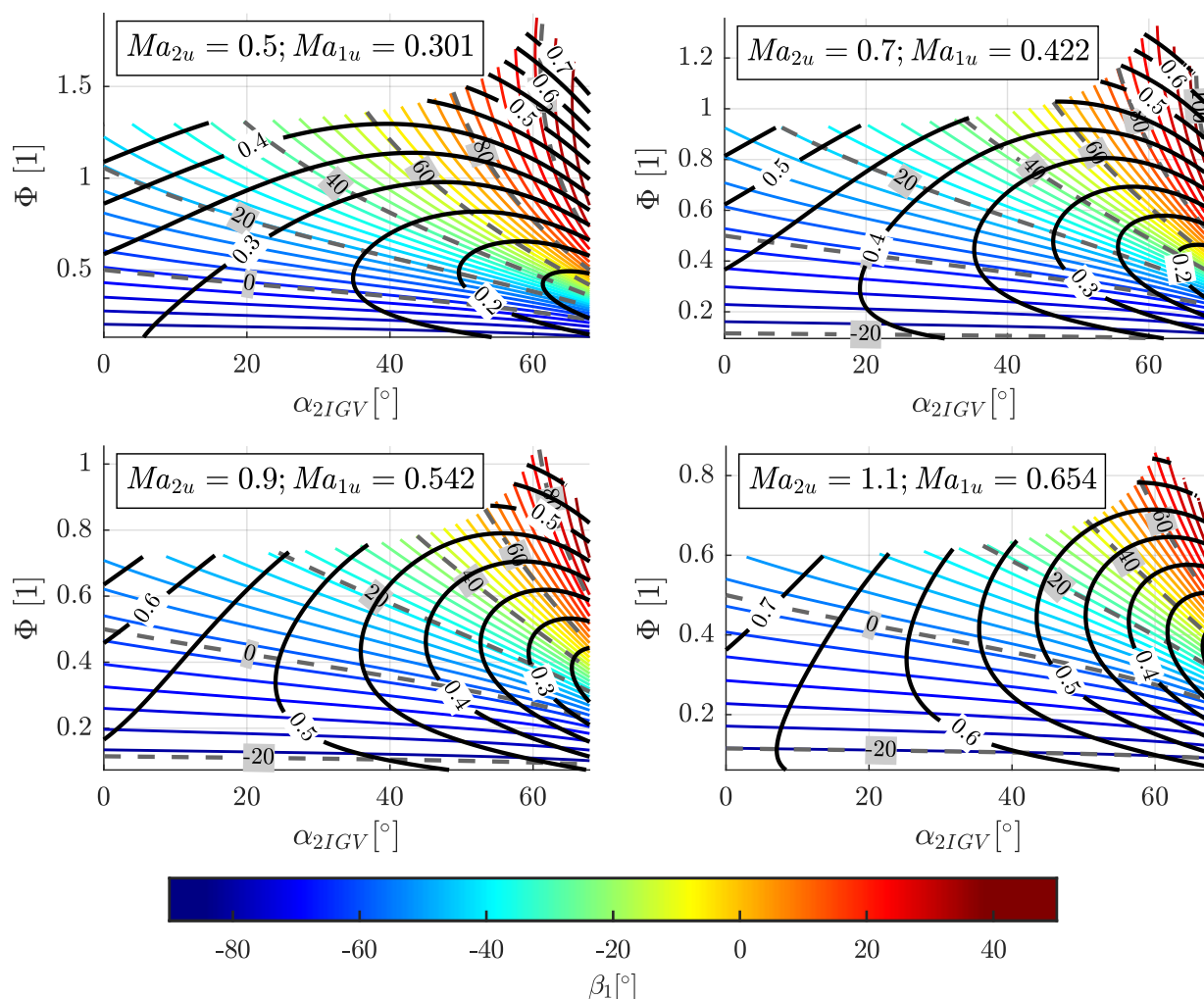
Figure 3.4: Relative flow angle at rotor leading edge (coloured isocurves). Negative incidence angle [°] (grey dashed isocurves) and relative flow Mach number [1] (solid black isocurves) for the s4 impeller.

pressure losses start to significantly enlarge the meridional velocity at the LE for the very same flowrate. The limiting curve on the right of the maximum is determined by reaching sonic speed at station 1.

A relatively low influence of the blade Mach number on the resulting relative flow angle can be observed. The four graphs have different ranges of Φ, but the β_1 values at the same coordinates differ very little and they start to significantly differ only in the region of intermediate flowrates and maximum swirl angles. Such a region is outside the range of useful operation points. This confirms that the influence of flow static state change is not crucial, but one has to observe flow coefficient values rather than absolute flowrates.

On the other hand, the collocated values of relative flow Mach number are far apart amongst the presented four impeller speed cases. Also, the shape of the isolines allows very different behaviour: When following compressor map speedlines (vertical lines in the presented graphs for constant Ma_{2u}, α_{2IGV} and flowrate typically varied from high to low), for some of them the relative Mach number evolution is monotonous, while for others it can decrease and later increase again. [6] presents a value of 0.7 as a practical limit of the efficient and reliable operation of a subsonic compressor and states, that at low relative Mach numbers the tolerance of the blade to higher absolute incidence should increase.

It is not trivial to tell when the speedline-minimum of Ma_{1w} separates from the surge limit and is moved somewhere midway through the speedline. Let the data presented in the lower-right graph in Figure 3.4 be trimmed by a presumed viable interval of incidence angles, say $i \in \langle -20°, 20° \rangle$. It is possible that the trend of Ma_{1w} along the speedlines can be monotonically decreasing together with the flowrate for low swirl angles and monotonically increasing for high swirl angles. At intermediate swirl, a minimum of Ma_{1w} is found within the mentioned interval of i.

3.2.4 Conclusion of the leading edge state preliminary analysis

It was shown that IGVs in radial arrangement do not create a swirl angle equal to their stagger angle. The vane exit metal angle is higher, see Table 1. Other properties of the cascade were briefly discussed.

The outcomes of the latter part of this analysis state, that the relative flow angle on the impeller LE is safely and predictably dependent on the adiabatic expansion in the swirling flow in the inlet channel behind the IGVs. For the same flow coefficient values and inlet gas total state, it is practically independent of impeller rotational speed.

An interesting relationship of relative Mach number at LE is discovered. Without this analysis, the value of this important parameter would seem rather unpredictable. As for many compressor map speedlines the course of Ma_{1w} would not be monotonous, it can point to the reason why there is a real possibility of inducing instability in the middle of the speedline which diminishes later on. The occurrence of a minimum of Ma_{1w} mid-speedline mostly occurs at intermediate swirl angles.

The attempts to generalize the experiment results by expressing a criterion equation were ceased as it would be geometry-specific and the coefficients would need to be validated for several intervals of the solution. Therefore the practicality of the equation is questionable.

3.3   Measurement results

All the results presented here were obtained using the BWR EoS. Humid air with a known, measured, relative humidity at the compressor inlet was considered for the measured data. Evaluated measured data was scaled to a standardized inlet state of fixed temperature and pressure and a zero humidity. The procedure is described in section 2.3.

3.3.1   Compressor performance maps

Before looking into what extra information could be derived from the measurements, standard compressor maps are shown. The unexpected defects motivating all of this work can be observed. More complete data and a detailed description are presented here, unlike the brief discussion written about Figure 1.5 in section 1.2.

The most interesting data were collected for the u4 stage, which shows extremely unstable behaviour. Some of the characteristic curves feature two or three instability intervals compared to one or no unstable regions for the other tested stages equipped with the radial IGVs.

As the industrial measurement campaigns were concentrated on producing *useful* parts of the compressor map, the defective curves were measured without waiting periods for thermal stabilization. The temperature readings for these measurements may have been influenced by the transition effects between operational points. This influences power, power coefficient and efficiency evaluation.

Unlike the s4 stage, the u4 stage was not equipped with the channel wall static pressure taps between the IGVs and the rotor. Unfortunately, the method for determining the flow angle described in subsection 3.3.2 is not applicable. This is also the reason for the selection of the s4 stage for a detailed analysis. Even for the s4 stage, the states evaluated in the channel between IGVs and the impeller are just estimates, as mentioned in subsection 3.3.2.

It is a general practice in the measurements that the flow coefficient is expressed from the volumetric flow rate at the selected intake station of the machine section and the impeller outlet circumferential speed. It is not equal to the Φ used in Figure 3.4, but it should be close to being directly proportional to it.

The data presented in this subsection are rescaled to a standardized intake gas state and corrected for the rotational speed discrepancies by the algorithms described in section 2.3. The evaluated section is defined by intake station 0 (upstream of IGVs) and discharge station 4 (vaneless diffuser outlet). (Sections are annotated in Figure 2.2.) The discharge pressure, mass flow rate and polytropic efficiency are normalized by the values at an arbitrary reference operating point. This is to avoid publication of confidential data and it is denoted by the N subscript of the respective variable symbol.

The u4 stage was measured at an extended set of IGVs stagger angles and a standard set of four blade Mach number values. The graphs in Figure 3.5 feature just a selection of a few ϑ values. The set of graphs in Figure 3.6 involve speedlines at all of the available positive IGVs stagger angles in groups of constant blade Mach number.

To avoid confusion, the defects themselves are described here first. Most of the well pronounced defective sections of the characteristic curves were revealed as follows: Starting at the maximum flowrate, the compressor operator gradually increased the resistance of the discharge tract of the compressor by adjusting the control valve, producing measured operating points along the way. At a certain moment, the flowrate dropped significantly and instantly. The discharge pressure and the efficiency plummeted too. Due to a decrease in efficiency, the total power curve does not feature substantial shape changes, but the power coefficient proportional to the mass-specific work done on the gas exhibits an inflexion in the curve. Further progress in closing the control valve was met with a less frantic response, till the moment when the current operating point leapt upwards to the initially expected location on the characteristic. During this recovery process, a rather strange response of increasing flow rate with the increase in the controlled discharge resistance was experienced, as seen in the graphs below. Such a phenomenon indicates that a certain flow feature started to decrease the flow blockage it caused with an increase in upstream pressure. The machine was excessively noisy along the whole course of the defective characteristic, even outside the obvious defects themselves.

It is worth mentioning that a step backwards to the original control valve setting did not return the compressor to the same point. Instead, strong hysteresis was observed. However, this is not recorded in the presented data. The hysteresis can explain the possibility of overlapping characteristic curves in some of the presented graphs. Normally, the operating point parameters are unambiguous to the control mechanism setting and characteristic curves never cross.

As [6] describes on an incompressible flow pump, the dynamically similar conditions for a variable speed machine with fixed geometry lie on parabolas in the pressure-flowrate diagram. The dynamic similarity means the shape of the streamlines is the same for the two compared operating states. This is also valid for the compressible flow of air on the test bed, but here the rotational speed bound with the reference Mach number plays a role. For such a compressor stage including IGVs, the swirl angle is another additional parameter.

The influence of the blade Mach number largely diminishes with increasing swirl angle as it shifts the characteristics down the flow coefficient spectrum. At lower flowrates, the local values of flow Mach number are lowered and therefore the compressibility effects weaken rapidly. This can be observed in the Ψ-Φ diagram in the upper part of Figure 3.5. There, curves for a no-swirl inlet are well apart. Away from the choke limits of these characteristics, the power coefficient values for a constant flow coefficient follow the trend of the blade Mach number. In contrast, at just 30° of the IGVs angle, ($\alpha_1 \approx 35.5°$ from

University of West Bohemia, Faculty of Mech. Engineering   Dissertation thesis 2022/23

Department of Power Systems Engineering   Ing. Lukáš Hurda
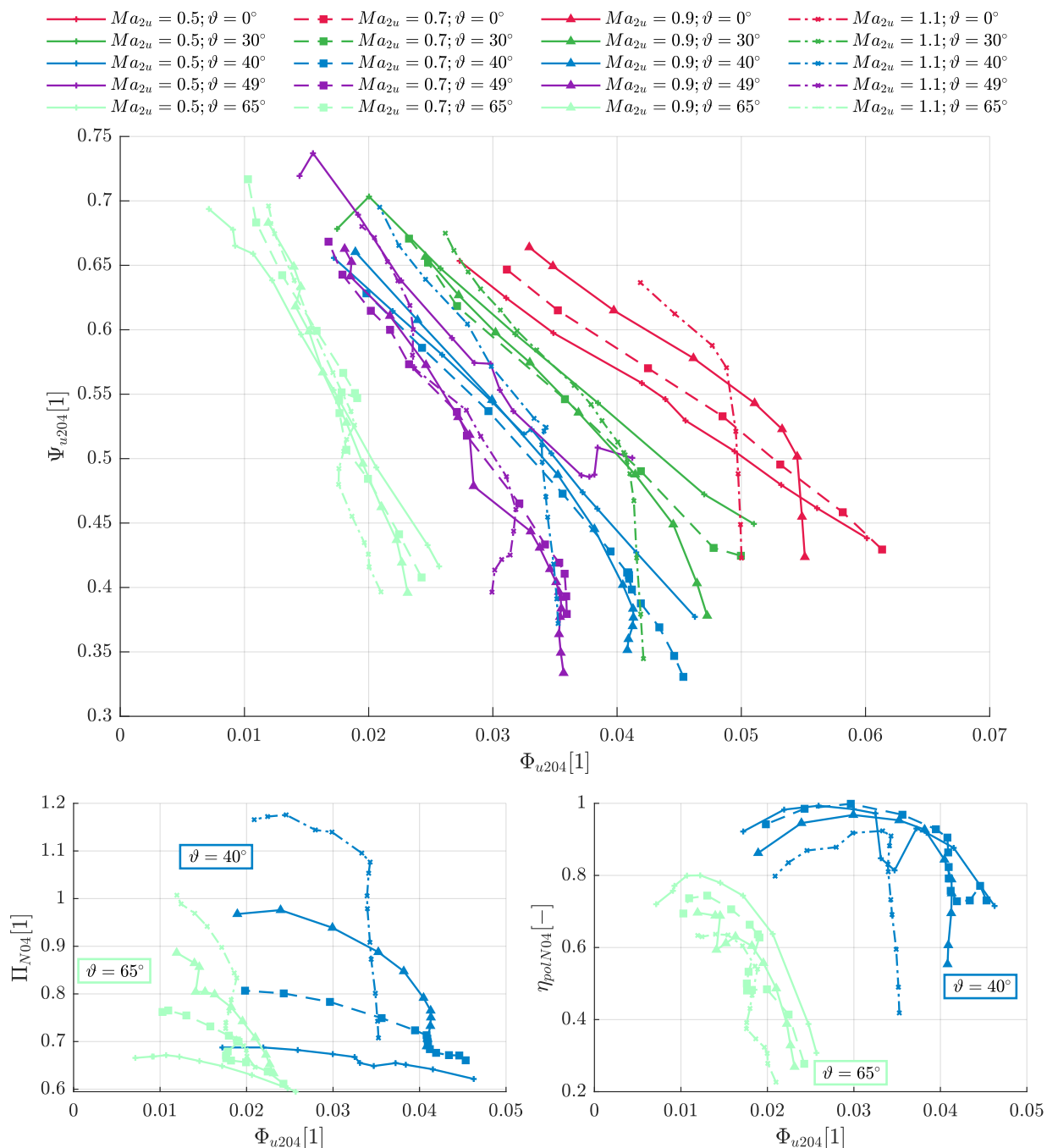
Figure 3.5: Dimensionless characteristics for selected IGVs angles, measured for u4 stage.

the numerical experiment), the curves are much closer to each other and the clear ordering by Mach number is not found.

From the turbomachinery perspective, the data measured at different inlet swirl angles are not dynamically similar for identical values of the flow and power coefficients, even

University of West Bohemia, Faculty of Mech. Engineering   Dissertation thesis 2022/23

Department of Power Systems Engineering   Ing. Lukáš Hurda
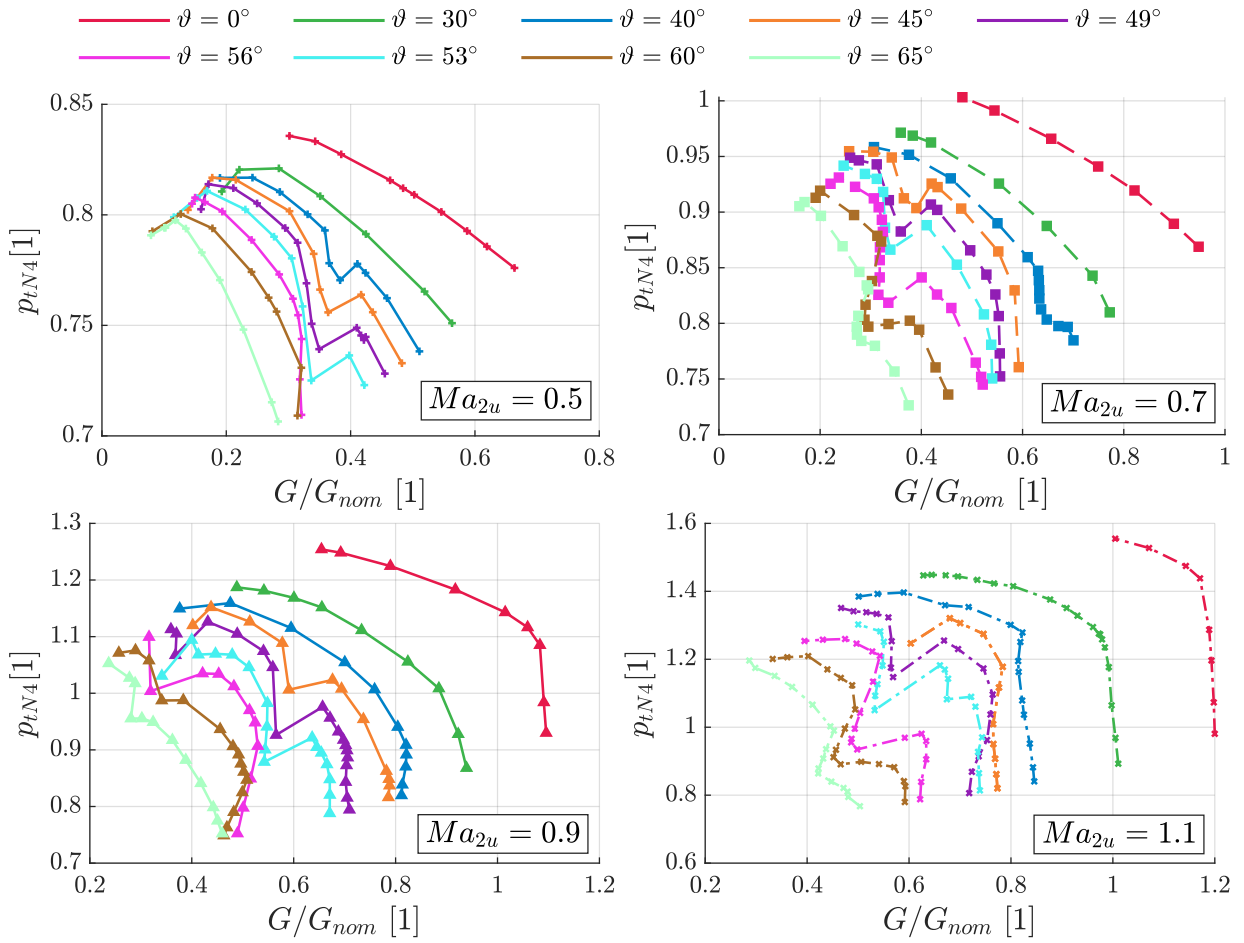
Figure 3.6: Normalized characteristics of absolute discharge total pressure versus absolute flowrate, measured for the u4 stage. Colouring and line styles are kept for the speedlines from the Figure 3.5, new colours are added for additional IGVs angles.

when the Mach number influence is already weak. For a constant angle of IGVs high enough to cause low flow Mach numbers, even the sensible parts of the defective curves lie close to each other in the Ψ-Φ diagram of Figure 3.5, expressing dynamic similarity. As can be seen in this diagram, but more clearly in the Π-Φ or η_{pol}-Φ diagrams shown in the same figure, the defects *do not* occur at the same locations or any recognizable bounded areas.

On the contrary, plotting the results in the absolute coordinates of the mass flow rate shows a clear relation between the locations of the defects, see Figure 3.6. The evolution of the relative flow Mach number examined in subsection 3.2.3 might be one of the suspected causes, suggesting that at a different blade Mach number, the similarity can be deteriorated by fairly different Ma_{1w} at otherwise comparable operating points. This claim is largely negated by the already mentioned collapse of the data to the proximity of a single curve in the Φ-Ψ diagram shown in Figure 3.5. There are also a few possible cases of the

University of West Bohemia, Faculty of Mech. Engineering   Dissertation thesis 2022/23

Department of Power Systems Engineering   Ing. Lukáš Hurda

constellation of the trends in the incidence angle and the flow Mach number: The trend of the flow Mach number might reverse at a moment at which the absolute incidence decreases (from negative to zero) or increases (from zero to positive). This means these two parameters can both act together favourably or adversely or counteract each other.

The most important conclusion made at this point is that the occurrence of instabilities is determined by the absolute flowrate (besides the IGVs swirl angle) and is largely insensitive to impeller rotational speed, i.e. the blade Mach number. Therefore it is probably induced by the flow in the channel behind IGVs and in front of the impeller. The flow in the diffuser is largely influenced by the impeller rotation, as it defines the absolute flow angle at the diffuser inlet. The discussed dynamic similarity therefore applies to the diffuser too, as it is encased between the analysed machine section intake and discharge stations 0 and 4. The cause of the instabilities must be independent of the impeller rotation and the only part of the section without a strong influence from the impeller is the intake channel.

3.3.2   Inlet channel flow criteria evaluation

As the simplified bladeless channel model introduced in section 3.1 and further analysed in section 3.4 was designed to mimic the real compressor in an approximate way, there are no obstacles to evaluating the outlined criteria from the measured data from the real compressor channel.

The challenge of expressing the Re and Ma in the desired location of the flow channel required a sophisticated use of standard measurement data evaluation procedures (shown in section 2.3). A complete measuring station (0) was placed in front of the IGVs (probes of p_t, p_s, T_t), and static pressure taps were present only on the impeller hub side of the channel behind the IGVs, none of them was on the shroud side. These were not located in the bend apex, but at 45° of the channel axial turn (measuring station $0b$).

It was attempted to calculate the actual mean swirl angle of the flow in the station. This required the approximation of total pressure (p_c) and total temperature (T_c) in the measuring station $0b$. First, the possibly significant total pressure loss of the flow through the IGVs was expressed from the static pressures (p_{s0} and p_{s0b}). A concurrent static pressure decrease due to flow area reduction and swirl introduction was considered. The guess of the dynamic pressure (p_d) change is based on the flow area ratio, assuming the rotation of the flow according to Table 1. The resulting expression reads as:

$$\Delta p_{tIGV} = (p_{s0} - p_{s0b}) - (p_{d0} - p_{d0b}) = (p_{s0} - p_{s0b}) - p_{d0}\left(1 - \frac{A_0}{A_{0b}\cos\alpha_{2IGV}}\right). \quad (3.15)$$

This pressure loss was subtracted from the total pressure in front of the IGVs to approximate the total pressure in station $0b$. The total temperature in $0b$ was calculated for an isenthalpic state change from p_{t0} to p_{t0b}.

This approximation is selected to account for the throttling effect of the IGVs, which was already adopted when total pressure loss was admitted. This is different from the isentropic process assumed in subsection 3.2.2. There, it introduces no problem as the static pressure is not fixed by the measured value. When evaluating the measurement, the isentropic process yielded an unrealistic resulting static temperature. A blending of isenthalpic and isentropic static temperatures was prepared, but the isenthalpic throttling seemed to be the most appropriate approximation.

The calculation of the flow angle should be possible from the meridional velocity expressed from a known mass flow rate and the absolute velocity magnitude based on the total to static enthalpy difference. The procedure is iterative due to the reciprocal dependence of the fluid static state on the absolute flow velocity and was briefly explained in paragraph 2.3.2.5. For this case, the algorithm is too sensitive and the limitations of the approximations made earlier render this method of flow angle calculation useless. Besides the approximations, the accuracy of measurement of a relevant static pressure value in station $0b$ is also questionable. Only 4 pressure taps were spaced along the circumference and mainly they were all placed on the same side of the channel. The measured hub wall static pressure might differ from the mean value in the station, especially in the part of the channel where the meridional flow path bends.

Instead, the above described procedure of approximating T_{t0b} was used to calculate the flow velocity with a fixed flow angle evaluated in subsection 3.2.1. This was achieved by using the approximated T_{t0b} and the measured p_{s0b} and setting the station flow area as its projection to the rotating flow direction to comply with the architecture of the station gas state calculation algorithm for non-swirling flow described in paragraph 2.3.2.5. The original algorithm for non-swirling flow was adapted to a known, fixed swirl angle. Hence the calculation of different values of velocity for its absolute magnitude and the meridional component became possible.

The determination of the working fluid state in station $0b$ allowed the expression of the fluid state in the bend apex denoted as station $0c$. It was done by simple extrapolation of the total state of fluid and recalculation of the static state for the respective flow area change - meaning that adiabatic flow approximation is used. Then, the flow velocity, kinematic viscosity and speed of sound are determined in order to express Re and Ma values corresponding to the CFD parametric studies. Without knowledge of the flow pattern, it is only sensible to approximate the swirl angle in the bend apex ($0c$) from the angle in Ob by means of the equation (3.11).

Unlike the previous subsection, the input data here comes from thermally stabilized measurements. The s4 stage was measured earlier than the very unstable u4. The instabilities of the s4 stage were concentrated mostly around 30° of IGVs stagger setting, although most of the speedlines at higher IGVs stagger was also noisy. At that time, the engineers responsible for the measurement decided not to measure the unstable speedlines, as they were useless for production machines. Unfortunately, it was not measured even in the "fast"

University of West Bohemia, Faculty of Mech. Engineering   Dissertation thesis 2022/23

Department of Power Systems Engineering   Ing. Lukáš Hurda
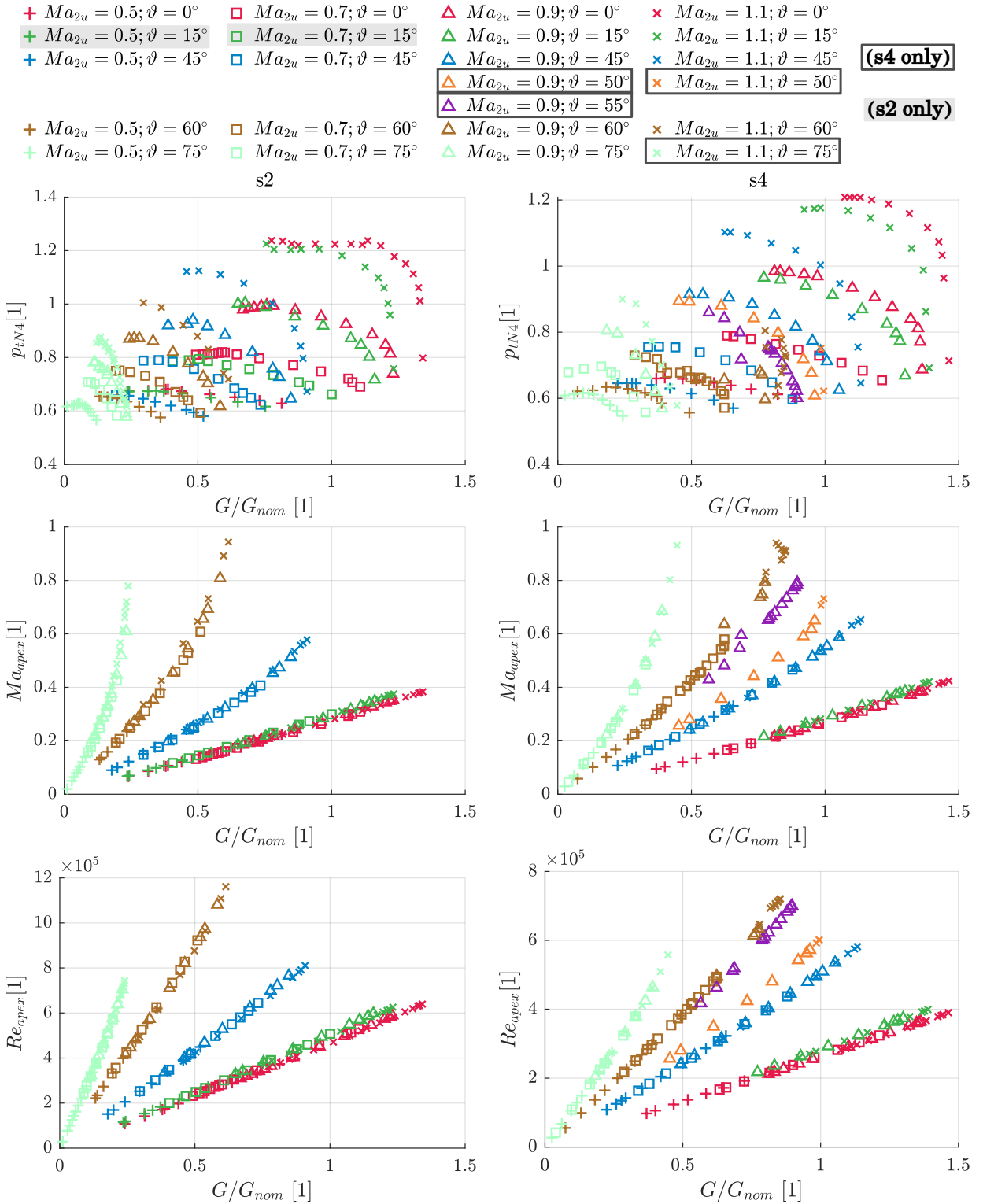
Figure 3.7: Normalized mass flow rate vs. normalized discharge total pressure, Reynolds and Mach numbers in the inlet channel bend apex for s2 (left) and s4 (right) stages.

regime - without thermal stabilization. The s2 stage was not noisy or unstable between surge and choke limits, the 30° speedline is omitted from the results just for conciseness.

The outcomes of the described calculations are shown in Figure 3.7. The only clearly pronounced instability is visible in the top right graph in the speedline of s4: $Ma_{2u} = 0.7, \vartheta = 60°$ (brown squares).

The values of both the flow criteria describing the state of the flow in the intake channel lie along identical curves for every single IGVs setting. They are not dependent on the impeller rotation, but mainly on the flowrate.

The Mach number evaluated from the actual flow static state and the absolute velocity in the bend apex station mostly follows the convex curve of the evolution of the absolute velocity. Its magnitude is obviously dependent on the swirl angle and the flowrate, and in incompressible flow, this relation would be linear.

The density drop in the compressible flow caused by the acceleration along the channel presents positive feedback to the velocity, such that this relation is not linear. The slope of velocity vs. flowrate at constant swirl increases with the flowrate. This effect is further amplified by the decrease of static temperature whose square root appears in the denominator of the Mach number expression. This holds for an ideal gas only, but using the real gas EoS for dry air at moderate conditions does not deteriorate the validity of this explanation.

Also, the fact that an isenthalpic instead of an isentropic process was assumed for the change of the gas state between the stations 0 and 0b does not affect the results: The pressure drop of the IGVs has a fairly lower heating effect on the gas than the cooling due to the increase in absolute velocity by the channel flow area contraction and the introduction of swirl by IGVs.

The high values achieved at a high flowrate and high swirl might be unrealistic. The reason would be the imprecise estimation of the IGVs flow deviation angle. It was assumed to have a linearly increasing absolute value as stated in subsection 3.2.3. At extreme metal angles like 89.5° at 75° stagger, the absolute deviation probably peaks.

For **the Reynolds number**, the relation to the flowrate is visually close to being linear. The length measure - the channel width - is a constant across all the data for a single stage. When using the dynamic viscosity for Re evaluation, the density influence is cancelled out, generally: $Re = cb\rho/\mu = G/(A\rho\cos\alpha) \times b\rho/\mu = CG/\mu$, where C is a constant for a given swirl angle α in a given channel of certain width b. The biggest variation in μ is reached at the highest swirl angle. Amongst all the measured points at $\vartheta = 75°$ (mint green) in the s4 stage, μ consistently drops with increasing flowrate along a concave curve by around 20 %. Therefore there *is* a slight progression in the slope of the Re_{apex} curves. In this case, the rather complex evaluation of the dynamic viscosity in the BWR EoS yields a linear function of the static temperature (with a zero absolute offset).

The instability of the flow in the inlet channel could be linked to the values of the presented Ma_{apex}, Re_{apex}, as already assumed in section 3.1. The values of Reynolds number lie well below 10^7. That means the influence of this criterion cannot be neglected - the flow is clearly fully turbulent, but it is not inertia-dominated, and the friction forces are not negligibly low in comparison. It is not clear what response to alterations in the Reynolds number should be expected. From the set of criteria used for inlet channel flow description, $Re = Re_{apex}$ is the only one bound with the flowrate.

The adverse effects of the Mach number are expected at the high values, as the Ma_{apex} will be related to Ma_{1w} discussed earlier, but only at the same rotational speed of the impeller. A more important conclusion from the absolute flow Mach number figures is that at many operating points, the flow can be considered incompressible ($Ma_{apex} < 0.4$). In the channel bend apex, a maximum absolute flow Mach number in the whole inlet channel is reached. The limiting value is rather arbitrary as compressibility of the flow has various effects and one has to decide, which ones of them need to be considered. It is believed that the flow pattern expressing dynamic similarity will not be altered significantly when incompressible CFD simulation is carried out for the operational points below this limit. At a value of 0.4, static and total gas states would be notably but not substantially different.

It might be crucial to recall here, that the swirl angle itself is expected to be a very important parameter of the instability origination.

To support the theory voiced in the previous subsection, that **the diffuser operation** is directed by the compressor duty similitude criteria rather than absolute flowrate, the results of the diffuser inlet (M) and outlet (4) absolute flow angles are presented in Figure 3.8. It resembles again the dynamic similarity given by the flow coefficient with an influence of the blade Mach number at medium to high flow coefficient values. At highly compressible speedlines (low ϑ, high Ma_{2u}) there is a notable increase in the flow angle along the diffuser due to the density increase. An upstream extrapolation of the total state from station 4 to station M was used to evaluate the state of gas in that station. Only wall static pressure taps measurements are viable in the vicinity of the impeller.

3.3.3   Conclusions of measured data analysis

It was confirmed that the instabilities of the machine operation must originate from the flow in the inlet channel between the IGVs and the impeller inlet. This is supported by the data analysed in subsections 3.3.1 and 3.3.2. The defects are not located in the dynamically similar conditions of compressor operation, they rather follow the criteria derived in section 3.1. The flow through the diffuser is directed by the compressor operation similitude, just like the flow through the impeller.

The values of the flow Mach number in the inlet channel apex show that an incompressible analysis would not be an overly simplified approach in many operational point cases.

University of West Bohemia, Faculty of Mech. Engineering   Dissertation thesis 2022/23

Department of Power Systems Engineering   Ing. Lukáš Hurda

Figure 3.8: Flow coefficient vs. diffuser inlet and outlet absolute flow angle (station M and 4) for the s2 (left) and s4 (right) stages.

The inlet channel flow also features fairly low values of Reynolds number. Such results yield the need to use Re as an independent parameter of further analyses. Low Re also poses relatively low requirements on the CFD modelling in terms of spatial discretization.

3.4   Simplified bladeless channel model

A CFD analysis of the simplified inlet channel is carried out to show the flow behaviour in the most simplistic and isolated way. Only the incompressible analysis justified in section 3.3 is presented. Three different geometries are used. They are parameterized by R_a, R_t, as defined in section 3.1 and Figure 3.1. The first generic model has the geometry set by $R_a = R_t = 1$, the latter are approximations of the s2 and s4 compressor stages.

The geometries are generated with an equal channel width $b = 1\,\mathrm{m}$. The inlet flow velocity is calculated so that the mean velocity in the bend apex is equal to $1\,\mathrm{m\,s^{-1}}$. The Reynolds number is then defined by the setting of the kinematic viscosity value. It is defined based on the velocity in the bend apex. This setup is advantageous for the manipulation in the multi-parametric study and also in the post-processing.

The flow swirl angle α is no more a global value - the flow is deformed and local values across the channel is not a constant even in the incompressible flow. Therefore α_I - the inlet flow angle prescribed in a cylindrical velocity inlet BC and α - the local value are distinguished.

All the production calculations are axisymmetric - the computational domain is defined in 2D (in the radial and axial coordinates). The solved vector quantities are still fully 3D, so the inevitable tangential swirl is possible. A preliminary analysis showed in subsection 3.4.2 verifies the relative equivalence of the results achieved in a 3D simulation of 30° periodic segment of an identical channel. The influence of the length of the inlet and outlet parts of the channel are tested in paragraph 3.4.2.2.

A steady incompressible viscous flow is assumed. The low turbulent Reynolds number version of the k-ω SST turbulence model (paragraph 2.4.2.2) is used according to the relevant methodology described in section 2.4. Most of the meshes are fine enough to allow wall-resolved computations without the employment of wall functions (exceptions are noted). The meshes were tuned for each geometry variant and the y^+ was checked in the results of the first computed cases with no swirl.

Structured meshes were generated in `gmsh`. An extremely coarse version is shown in Figure 3.9. The geometry is split into four blocks - straight inlet and outlet and front and aft parts of the bend.

The distribution of the grid points across the channel width is defined by `gmsh`'s `Bump` function, which allows to refining of the mesh near both channel walls using a single parameter. The point distribution is then very close to a geometrical sequence on either the hub or shroud side. The `Bump` parameter is manually iterated to produce a wall-normal

expansion rate below 1.05. This requirement is relaxed at the inlet and outlet so as not to produce high aspect ratio cells at the wall.

Another refinement is carried out in the inlet and outlet blocks. The cells are refined in the centripetal direction towards the bend blocks. The manual tuning of the mesh parameters aims to keep similar streamwise-dimensions of the cells at both sides of the block interface. The used `Progression` function produces a simple geometric sequence of cell dimensions. The coefficient is again kept below 1.05. An intrinsic property of the structured mesh is that it is denser in the streamwise direction on the shroud wall of the bend. Therefore this tuning results in a compromise of similar cell dimensions at the block interface on both shroud and hub sides. It is not feasible to set even slightly unequal progression on the sides of the straight blocks to alleviate this minor issue.
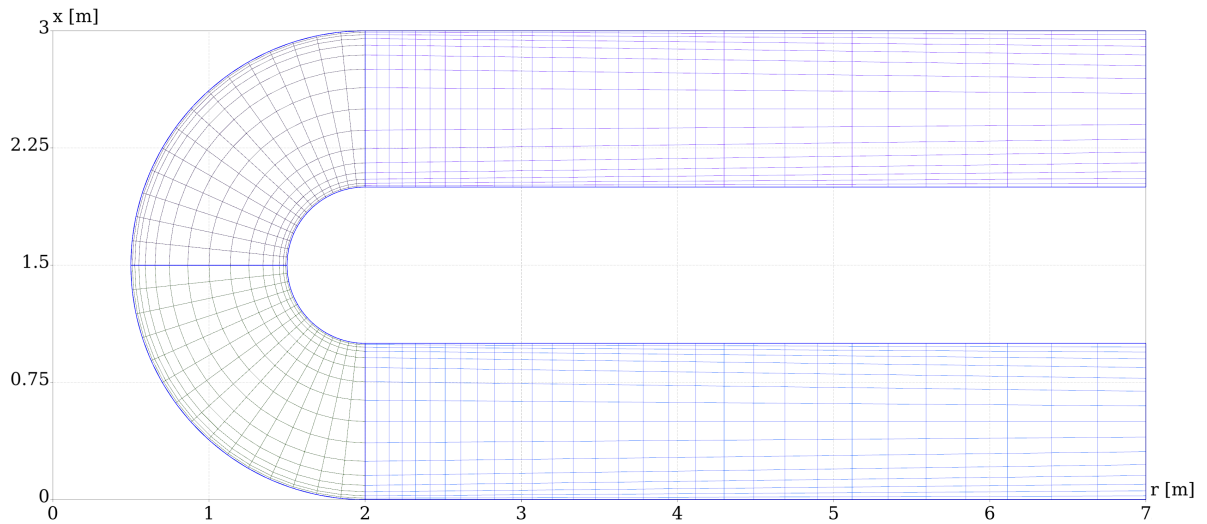
Figure 3.9: Bladeless channel computational mesh for $R_a = r_t = 1, n' = 5$ (coarsened for clarity).

Simulations are carried out in `OpenFOAM` using incompressible solvers, which use the kinematic definition of pressure (and also the post-processed wall shear stress) in $\mathrm{m^2\,s^{-2}}$. To keep the nomenclature simple, the expressions in equation (3.16) contain the standard quantities in Pa divided by the constant density, but the value of ρ is actually defined nowhere within the `OpenFOAM` case descriptions (unity is substituted for ρ in equation (3.16)).

3.4.1   Post-processing techniques

The coefficients of pressure (C_p) and friction (C_f) along both channel walls are expressed in equation (3.16). The Cartesian vector components of wall shear stress (τ_w) were transformed into the curvilinear coordinates of the wall surface and treated separately to produce graphs for the meridional and tangential parts of the coefficient of friction. The dynamic

University of West Bohemia, Faculty of Mech. Engineering   Dissertation thesis 2022/23

Department of Power Systems Engineering   Ing. Lukáš Hurda

pressure in the denominator of these expressions is a constant based on the mean velocity magnitude in the bend apex.

$$C_p = \frac{p}{1/2 \ \rho c^2}[1]; \qquad C_f = \frac{\tau_w}{1/2 \ \rho c^2}[1] \tag{3.16}$$

The pressure coefficient is usually used to assess the force actions of the fluid on the walls, but it also shows the pressure gradient along the wall. To some extent, it provides information about the near wall velocity. The friction coefficient is a more suitable quantity to assess near wall velocities. It is a very sensitive measure as it is dependent on the velocity gradient. The sign change in C_f is a clear and precise indication of the boundary layer separation.

To analyse flow away from the walls, several meridian-normal profile surfaces were sampled (as noted in Figure 3.1). The components of the local velocity vectors and their angles were evaluated within the coordinate system of that sampling surface. The already heavily discussed α describes the desired swirling rotation of the flow and the transverse angle γ represents the disruptions and redistribution of the flow across the channel - this is the deviation of the velocity from the meridional direction measured in the meridional plane. .

The curvilinear coordinates used in the post-processing are normalized. The transversal (spanwise) Y is normalized by b, it originates at the hub side and reaches a value of 1 at the shroud. The case of X is more complicated, for clarification see Figure 3.1. As channels of various lengths are analysed, the approach to expressing X is unified: the absolute locations of $X = 0, X = 1$ are both at the radial coordinate of $r_t + r_a + 2b$. That means the inlet and outlet locations of a bladeless channel generated for $n' = 2$. For larger n', the portions of channel above this radius are excluded from the graphs presented in the upcoming sections. Secondary horizontal axes are placed in the graphs to bind the bent part of the channel. The ticks of the bend angle axes conform with the cuts numbered 3 to 10 as noted in Figure 3.1.

3.4.2 Generic parametric study

Unless stated otherwise, $R_a = R_t = 1, Re = 10^6, I = 5 \ \%$.

3.4.2.1 Preliminary mesh resolution comparison

Three meshes were built for the purpose of these analyses. All meshes are orthogonal, they have low wall-normal and streamwise expansion rates and have a relatively smooth transition between the mesh blocks, as commented on in the introduction to section 3.4. The only concern in terms of mesh quality is the resolution of the wall boundary layer characterised by the first cell layer thickness at the wall. It is assessed by evaluation of the non-dimensional wall distance y^+ of first layer cell centres (Figure 3.10). The maximum aspect ratio of individual cell edges increases as the mesh is refined, but even for the finest

University of West Bohemia, Faculty of Mech. Engineering   Dissertation thesis 2022/23

Department of Power Systems Engineering   Ing. Lukáš Hurda
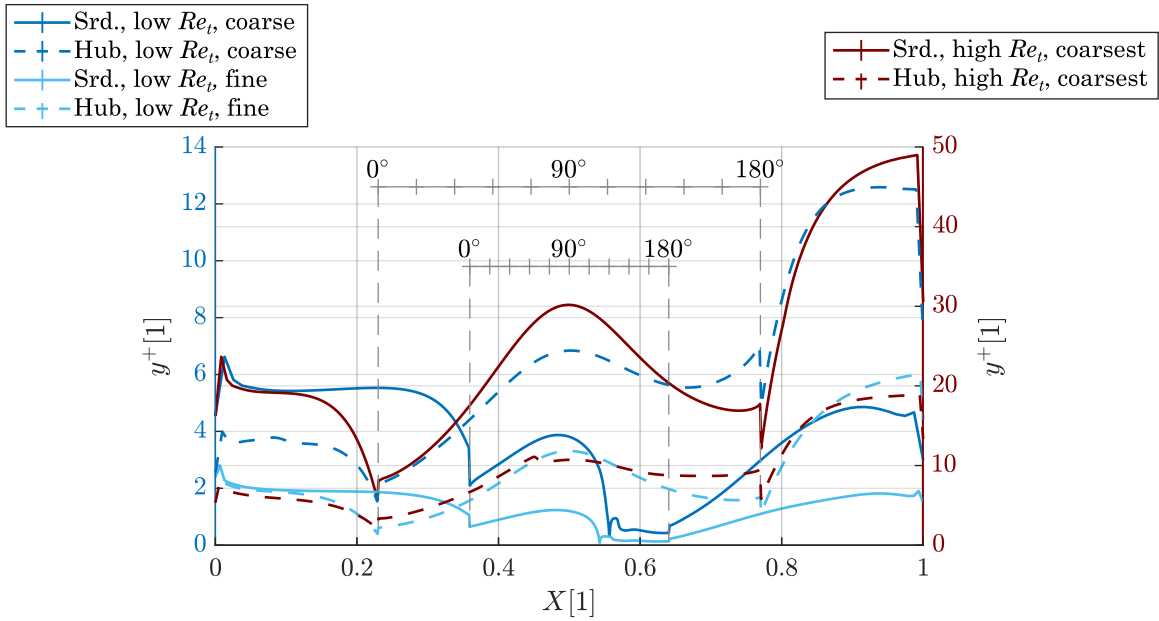
Figure 3.10: Comparison of meshes of finite volume cells via the non-dimensional thickness of wall-adjacent cells.

of meshes, the maximum is still below 100, which is satisfactory. Cells with such maximum aspect ratios are the first layer cells at the hub and shroud walls near the inlet and outlet.

The *coarsest* version is designed for use with high turbulent Reynolds number (Re_t) wall functions of the k-ω SST turbulence model and is used exclusively for the preliminary analyses. The high Re_t wall functions are designed to work with meshes, which have the first wall-adjacent cell reaching into the logarithmic sublayer ($y^+ \in \langle 30, 200 \rangle$). The finer variant (low Re_t, coarse) is a first attempt to reach the viscous sublayer, but the results indicate that for $Re = 10^6$, a finer mesh would achieve this goal more reliably. Therefore the *fine* variant was created. Still, some local y^+ values stand out above ~11, so the hybrid low turbulent Reynolds number wall functions are employed in all the production cases throughout section 3.4. These allow the resolution of the viscous sublayer where the mesh is fine enough and apply the wall function in the regions of coarser mesh or thin boundary layer.

3.4.2.2   Preliminary axisymmetric 2D to 3D comparison

All the details of the compared simulations are identical. The only difference is that the single-layer 2D mesh of the axisymmetrical case is rotationally extruded by creating angularly stacked copies of the original layer to produce the mesh for the 3D case. Then, the 2D specific `wedge` BC is switched to `cyclic` for 3D rotational periodic behaviour.

The 3D mesh forms a 30° periodic segment of 60 cell layers of uniform angular span. In order to keep a reasonable cell count, the source 2D mesh has only 67,200 cells (160

transverse times 420 streamwise, the *coarsest* version as mentioned in paragraph 3.4.2.1). This means the 3D mesh has 4,032,000 cells. It is not suitable for wall-resolved turbulence modelling, so the wall functions are employed within the two compared simulations. The resulting y^+ values fit within the 20 to 60 interval with the exceptions of the inlet and outlet areas and the stagnation regions, where it falls below 10.

As a non-swirling flow probably would not show any instability or 3D-specific behaviour, a case of $\alpha_I = 45°$ is selected for the 2D to 3D comparison.

The first finding is that the solution of the 3D case is not convergent to the same level as the 2D case. Both cases were run for 9,000 iterations of the SIMPLE algorithm. The relative residuals of the solved quantities of the 2D case fall below 10^{-5} with the exception of pressure, which only reaches a residual around 10^{-3}. In the 3D case, the final residuals of around 10^{-3} are common for pressure and velocity components as well as the turbulent quantities.

In Figure 3.11, the 3D flow pattern can be observed in detail, without spatial averaging. The values are significantly uneven along the angular coordinate Θ only at the location of flow separation from the aft part of the shroud wall bend.

The instability of this region is justified by the strong adverse pressure gradient found between circa 120° to 140° of the channel bend angle. As the flow pattern in this region shows structures that barely fit within the simulated 30°, it might also be suspected that the flow is influenced by the periodic BC. For a precise description, a wider wedge or a full torus would need to be simulated.

However, the separation on the shroud side is of lower importance, as it happens in the far aft part of the bend, where the flow in a real machine would be probably influenced by the rotor. The opposite side of the channel shows a very even distribution of velocity and pressure along Θ despite the large recirculation region emerging right in front of the bend apex.

Figures 3.12 and 3.13 show the results of the 2D case along with the circumferential average of the 3D case results. Despite a worse convergence, the flow characteristics averaged across the wedge angle remain very close to the case with just one layer of cells in the tangential direction. For a precise quantitative description of the flow, a 3D unsteady flow simulation would be necessary to address the convergence problem. For other parametric studies below, the 2D axisymmetric cases are utilized.

3.4.2.3   Preliminary analysis of the influence of the channel length

The proximity of the inlet and outlet BCs was tested in 2D, again with $\alpha_I = 45°$. Two variants of $n' = 2$ and $n' = 5$ are compared. (The values of n' are defined in Figure 3.1.)

It is worth noting the type of the outlet BC which is kept throughout section 3.4 - it is the `pressureInletOutletVelocity` type according to `OpenFOAM` terminology which allows
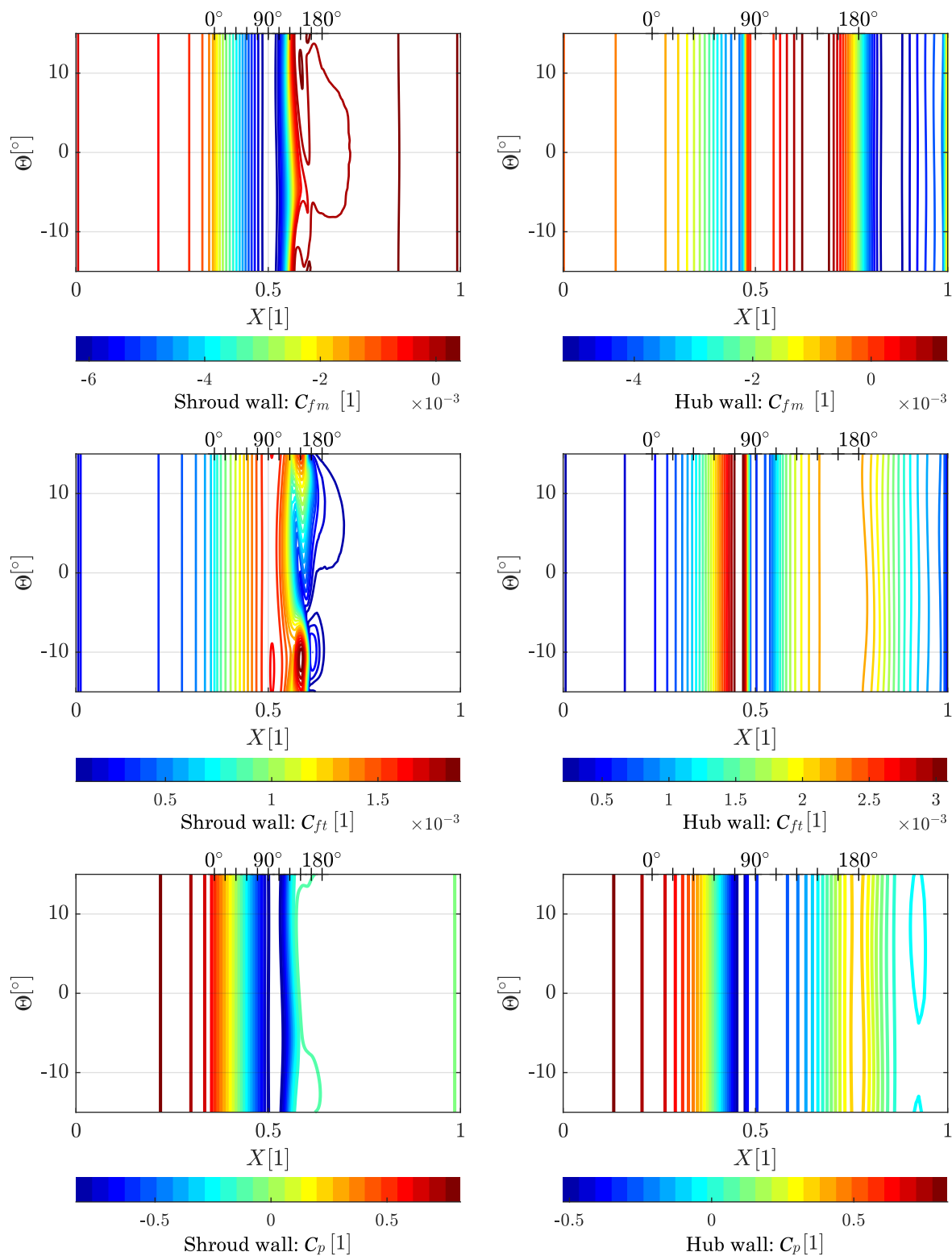
Figure 3.11: Maps of the coefficients of friction (meridional and tangential) and pressure at the channel walls of the 3D case.

University of West Bohemia, Faculty of Mech. Engineering   Dissertation thesis 2022/23

Department of Power Systems Engineering   Ing. Lukáš Hurda
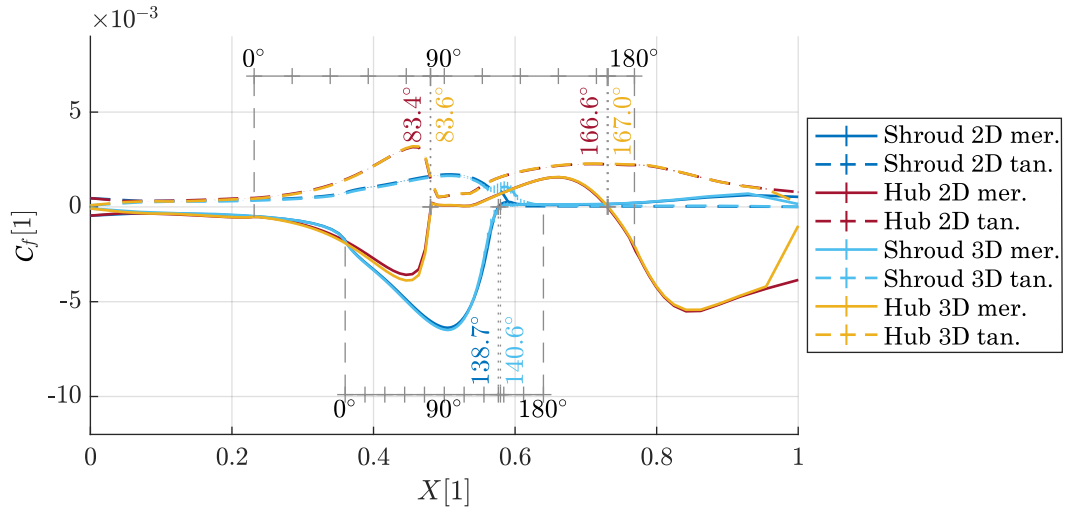
Figure 3.12: Comparison of 2D and 3D cases via coefficients of friction (meridional and tangential) at the channel walls. The 3D data are circumferentially averaged.
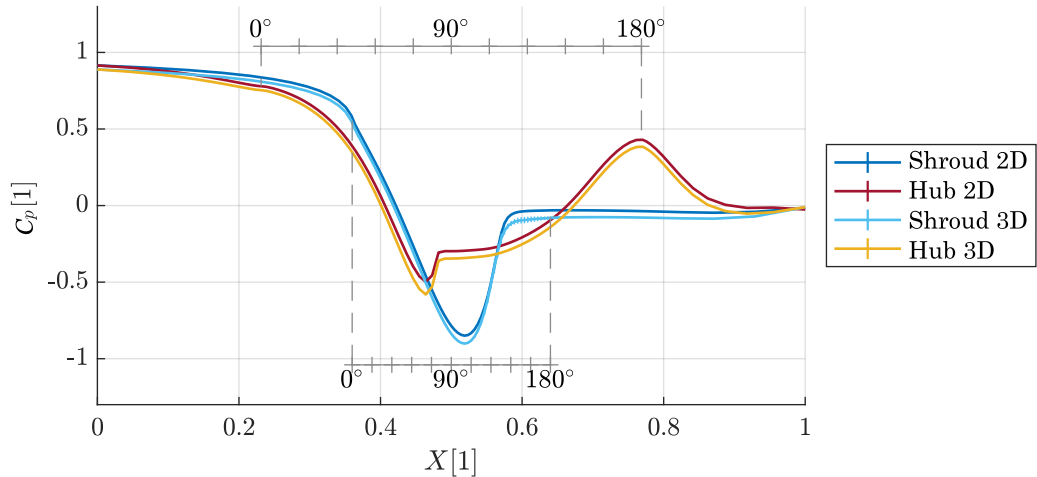
Figure 3.13: Comparison of 2D and 3D cases via coefficient of pressure at the channel walls. The 3D data are circumferentially averaged.

the backflow via the outlet patch computed from the extrapolated flux in a patch-normal direction. It is used together with a fixed uniform total pressure BC for the outlet.

Coarse meshes in conjunction with wall functions are used as in the previous paragraph 3.4.2.2. The longer channel differs only in the streamwise number of cells in the elongated inlet and outlet blocks.

In Figure 3.15, a vertical shift of the curves is visible due to the additional pressure loss in the longer outlet part of the channel. The hub side pressure drop in the bend occurs farther and falls deeper for the long channel. In Figure 3.14, the hub side separation is
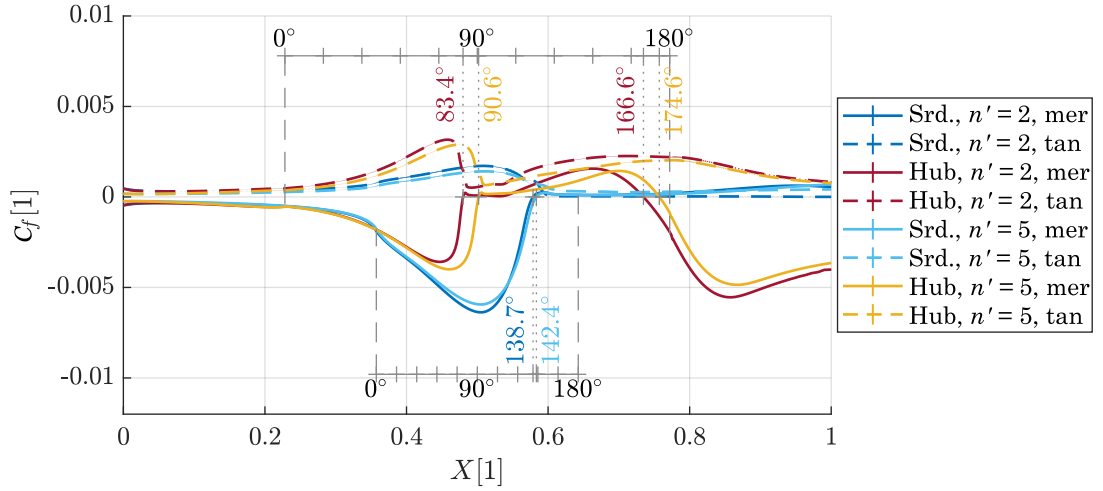
Figure 3.14: Comparison of the long and short channel cases via the coefficients of friction (meridional and tangential) at the channel walls.
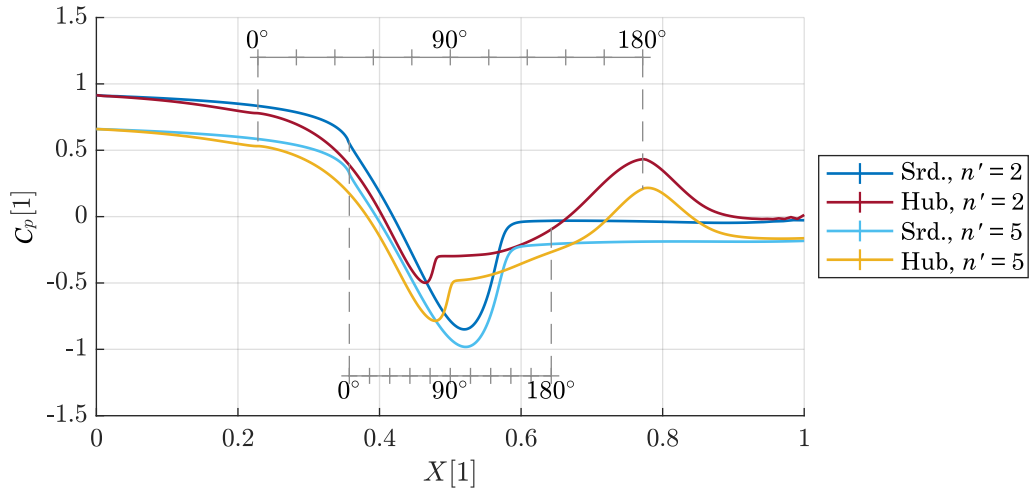
Figure 3.15: Comparison of the long and short channel cases via the coefficient of pressure at the channel walls.

found farther away, even though the shroud side separation is nearly at the same location. Figure 3.16 shows that even in the long channel, outlet backflow happens, i.e. the separated flow never reattaches to the shroud wall in either of the channels.

3.4.2.4   Study of the flow swirl angle influence

The flow angle α_I is varied from 0° to 60° in 5° steps, other parameters are fixed. The most important feature of the flow is the separation of the boundary layer and the adjacent recirculation zone emerging at the hub-side wall. (Already observed in Figure 3.16). The most obvious, but very important, finding derived from Figure 3.17 is that the discussed
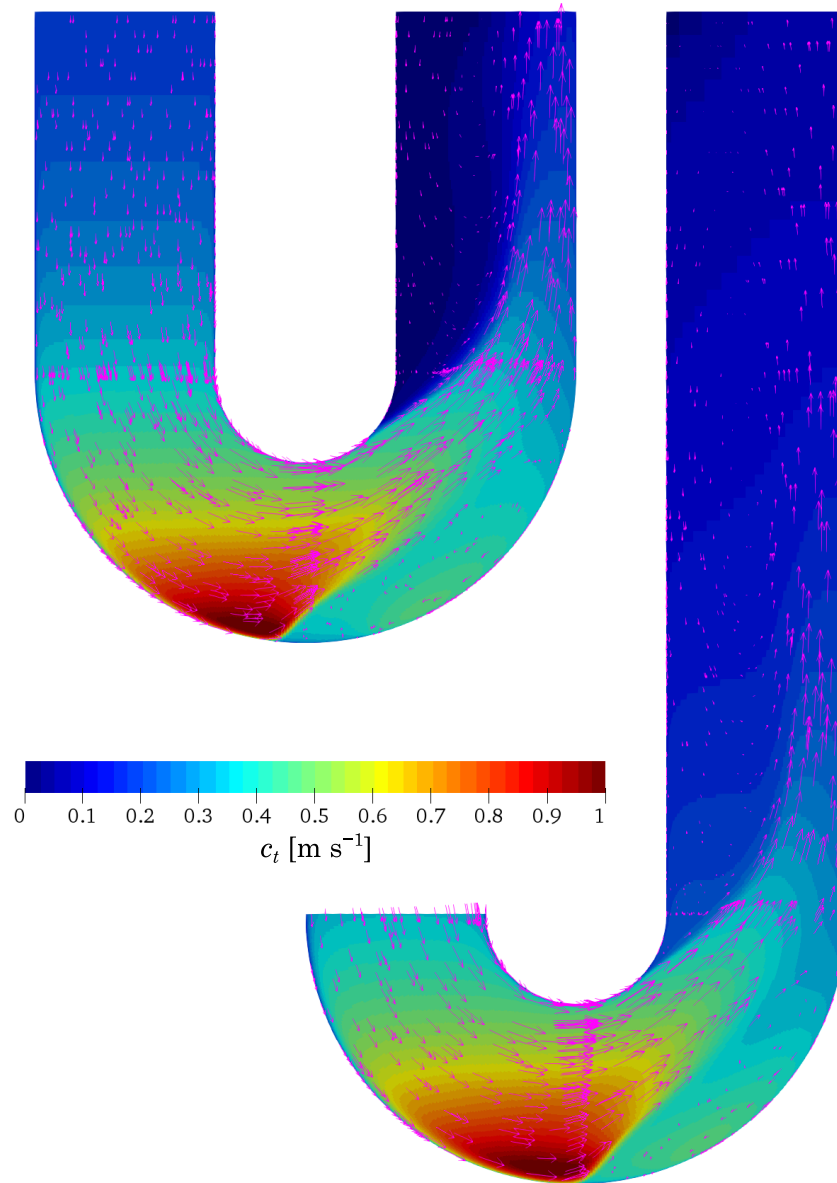
Figure 3.16: The long and short channel comparison via vectors of the axi-radial velocity and contours of the tangential velocity. The inlet part of the long channel is not displayed.

recirculation starts to occur when $\alpha_I > 40°$. For $R_a = 1, R_t = 1$ the value of the critical flow swirl angle derived at the end of subsection 3.1.1 is confirmed.

A similar recirculation zone is present in the aft part of the bend at the shroud wall in all of the cases discussed here. It probably does not have a significant relation to the flow in a real machine as it happens in the region far inside the impeller where the velocity field

University of West Bohemia, Faculty of Mech. Engineering   Dissertation thesis 2022/23

Department of Power Systems Engineering   Ing. Lukáš Hurda

will be significantly different. It does, however, influence the reattachment to the hub wall, as it directs the separated flow towards this wall.
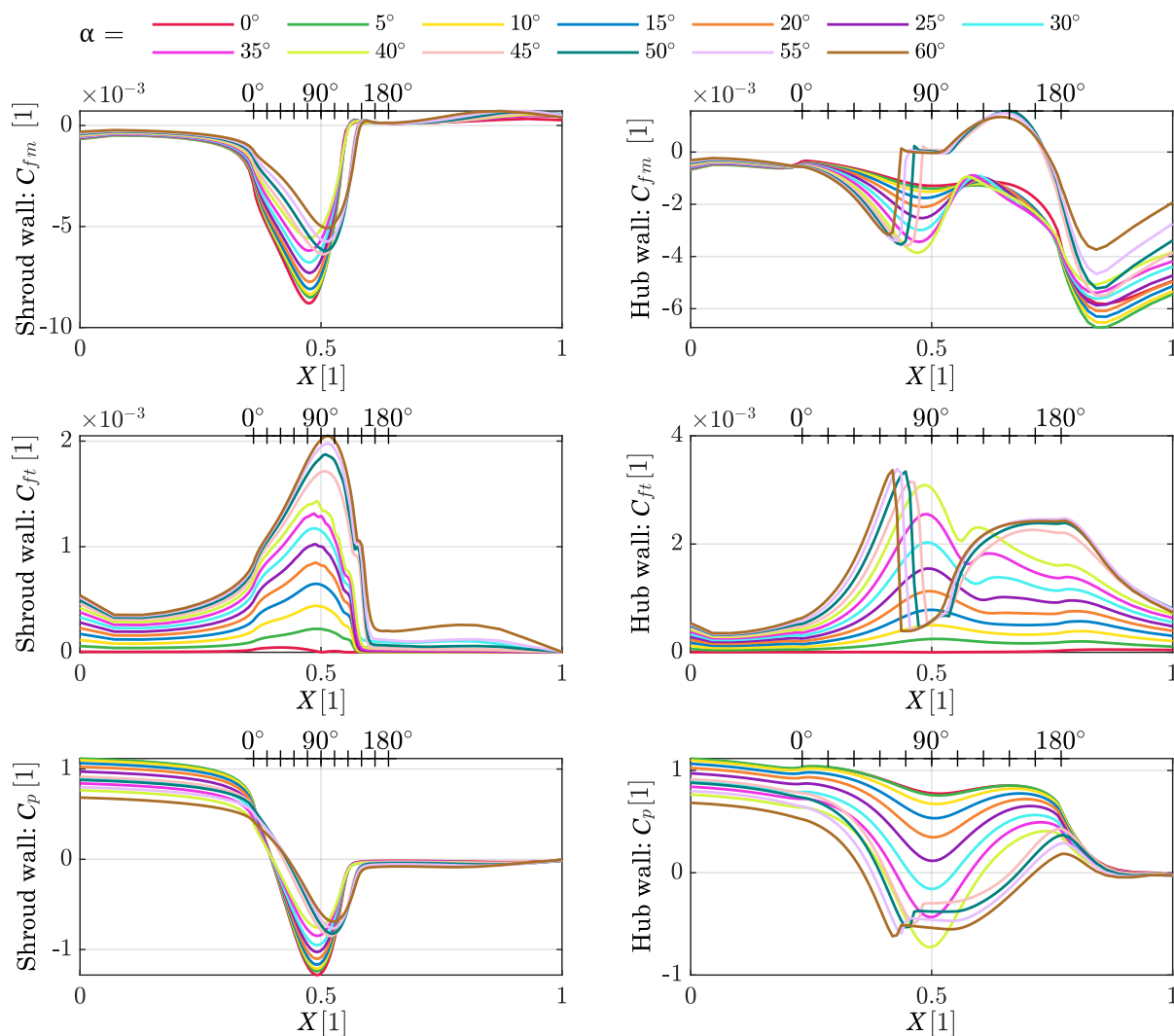
Figure 3.17: Coefficients of friction (meridional and tangential) and pressure at the channel walls for a variable flow swirl angle.

The sign change in the friction coefficient clearly indicates the location of the separation. Only the meridional component exhibits such behaviour. The tangential part drops significantly, but the flow never reverses in the circumferential direction. The flow structure can be described as a ring vortex. The flow inside it rotates around a circular shaped axis. The location of the separation is shifted upstream with further increases of α_I above 45°.

The gradual loss of the stability of the boundary layer on the hub wall is characterised by an increase of the peak underpressure in the bend apex of the hub (seen at the bottom right of Figure 3.17). This local minimum does not shift its location with flow angle, up to

the limit of separation. As the pressure drop grows bigger, the absolute pressure gradient in the surrounding areas increases too.

When $\alpha_I > 20°$, a new local extremity arises in both of the components of the hub side C_f, somewhere between 110° to 130° of the channel bend. It becomes more pronounced with increasing α_I and it shifts upstream. As the local extremity marches upstream, it reaches the location of the steepest adverse gradient, which makes the flow more prone to separation. Comparing the curves of hub C_{fm} for the separated flow with the lower swirl angle curves allows linking of the discussed extremity to the point where the intense backflow reaches. The more pronounced local minimum of hub-side C_{fm} in front of the bend apex is similarly linked to the factual location of boundary layer separation. The flow region nearby this point is rather stagnant, as verified by the curves for cut number 8 in Figure 3.18. The intense recirculation is pictured in cuts 10 and 12.

The less important situation on the shroud side is different. The location of the pressure minima is changed slightly when the flow changes from attached to separated, but within these two variants, the extreme point of pressure does not move. The centrifugal forces have exactly the opposite effect to the flow compared to the hub side. The rotation in the tangential (circumferential) direction stabilizes the shroud wall boundary layer and the turning along the curved meridian causes the separation. The separation is determined much more clearly as the axial curvature of the shroud is always significantly larger. Therefore the adverse pressure gradient in the aft part of the bend is severe.

In Figure 3.18, two cases nearest to the switch in the flow are compared. Some interesting features can be observed. The meridional velocity profile development shows a local maximum near the hub at cut 6 for both inlet angles. It is also present at cut 8 for the $\alpha_I = 40°$ case. Otherwise, the whole profile follows the expected evolution with a gradual velocity increase near the shroud side. This hub-side local maximum is probably associated with the intense flow area contraction at the hub-side. The centrifugal force caused by the axial bend of the channel supports this evolution as it suppresses the transversal redistribution of the mass flux. At the beginning of the bend, this body force is stronger than the tangential centrifugal force.

The low intensity flow redistribution is visible in the flow angle plots in Figure 3.19: the transverse angle is low, but consistently positive, which means there is gradual flux redistribution towards the shroud.

Figure 3.19 also shows the neutral centre of the recirculation zones. They are indicated by steep shifts between the limiting values of γ.

The value of the swirl angle at cut 10 rises above 90° for the case with the hub side separation. Linking this finding to the tangential velocity at the same location for the same case yields an interesting conclusion: as the tangential velocity does not drop substantially across the channel width, the tangential momentum is not suppressed in the aft part of the recirculation zone, but only in the front of it (at cut 8).

University of West Bohemia, Faculty of Mech. Engineering   Dissertation thesis 2022/23

Department of Power Systems Engineering   Ing. Lukáš Hurda
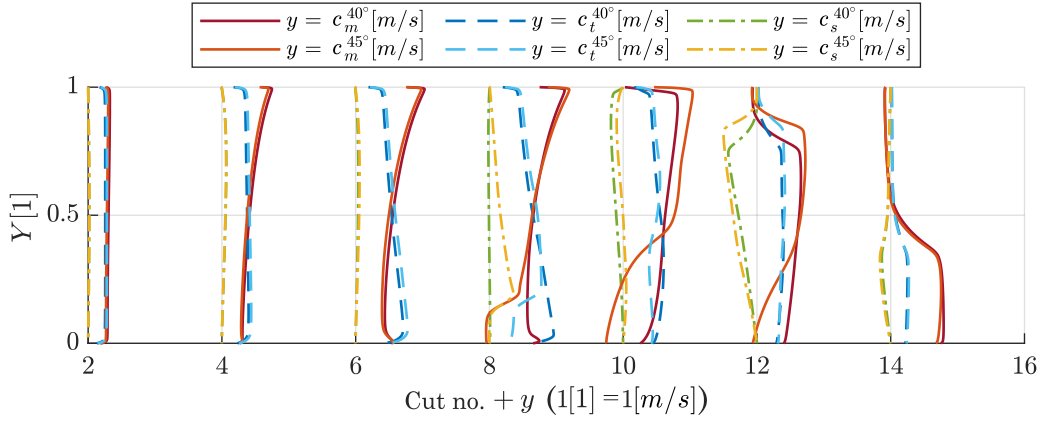
Figure 3.18: Flow velocity component profiles in the channel cuts for $\alpha_I = 40°$ and $45°$ cases.
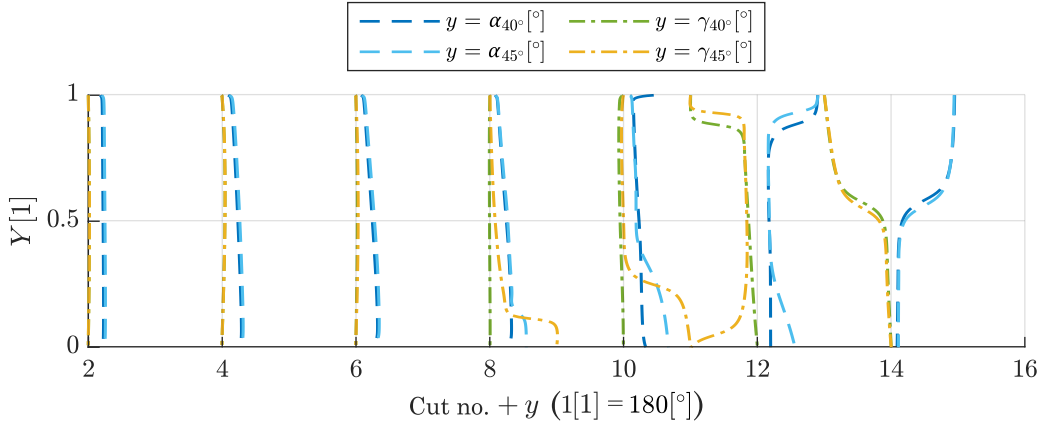
Figure 3.19: Flow angles in the channel cuts for $\alpha_I = 40°$ and $45°$ cases.

3.4.2.5 Study of the influence of geometrical parameters

The geometrical parameters R_a and R_t were adjusted together. Values of 0.8, 1, and 1.2 were permuted to produce 9 cases. From the results of the previous study, the value of α_I was fixed to $45°$ and the influence of the geometry adjustments to the flow separation from the hub wall were observed. Figure 3.20 shows the produced channel shapes. Note the machine axis position too (dash-dotted line). The scale is uniform, as well as the channel width.

The pressure and friction coefficient results are shown in Figure 3.21, and the complementary graph of the meridional velocity profiles is in Figure 3.22. Due to the variable absolute length of the bends, the straight radial parts were cut off the graphs and the remains of the curves were fitted into the polar coordinate system of the bend.

Results show that the discussed changes in the geometry did suppress the recirculation at the hub side in one of the cases: $R_a = 1, R_t = 1.2$ plotted in orange.

$R_t = 1.2$

$R_t = 1$

$R_t = 0.8$ $R_a = 1.2$ $R_a = 1$ $R_a = 0.8$
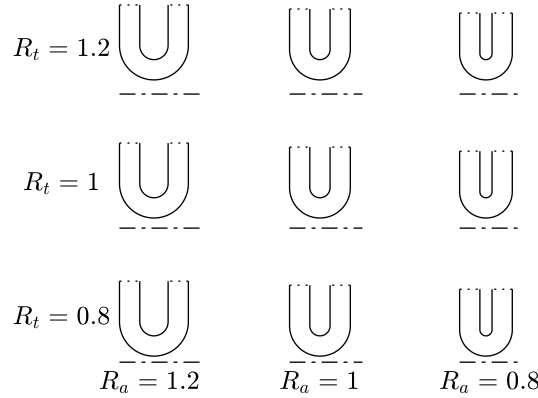
Figure 3.20: Illustration of the modified channel geometries.

Lower R_a causes earlier separation from the shroud wall. The earlier separation of the shroud boundary layer later causes earlier reattachment of the flow on the hub side. The reattachment is supported by the fast stream of the fluid deflected against the hub wall.

The value of R_t dominates the hub side boundary layer. The higher centrifugal force from tangential rotation at the lower R_t causes a sooner hub side separation. As the separation is moved far in front of the bend apex in the $R_t = 0.8$ cases, it is clear that the pressure gradient is not a very important factor here - if the separation did not take place, the gradient would be favourable in front of the apex (as confirmed by the result of C_p at the hub for the only case without the hub separation).

The strength of the pressure gradient also does not seem crucial for the existence of the hub side separation in the high R_t cases. More precisely, the pressure gradient can be predicted by the evaluation of the flow area contraction in the channel bend. The ratio of the flow area at the beginning of the bend to the flow area in its apex is equal to $1 + R_a/R_t$. This means the acceleration of the fluid in the first half of the bend and the deceleration in the second half is more intense for lower values of R_t and higher values of R_a (see Table 3). The streamwise pressure gradient follows the mean velocity trend, as confirmed by the bottom right graph in Figure 3.21. This does not apply to the bottom left graph for the shroud side C_p, as the inertial effects of the axial flow turn overpower the flow area contraction.

The concept of the critical flow angle binds together the R_a and R_t and describes the centrifugal force balance. It is a counterpart to the flow area ratio, which describes only the pressure gradient effects. Looking at Table 2, it is clear that separation in the $R_a = R_t = 1.2$ (red) case should actually be expected at 45° of the inlet swirl. On the other hand, all the cases where $R_a < R_t$ (orange, pink, the lightest green) should not feature the hub side separation based on the critical angle predictions. Nevertheless, the margins at the critical angle are all very low and should not be considered decisive.
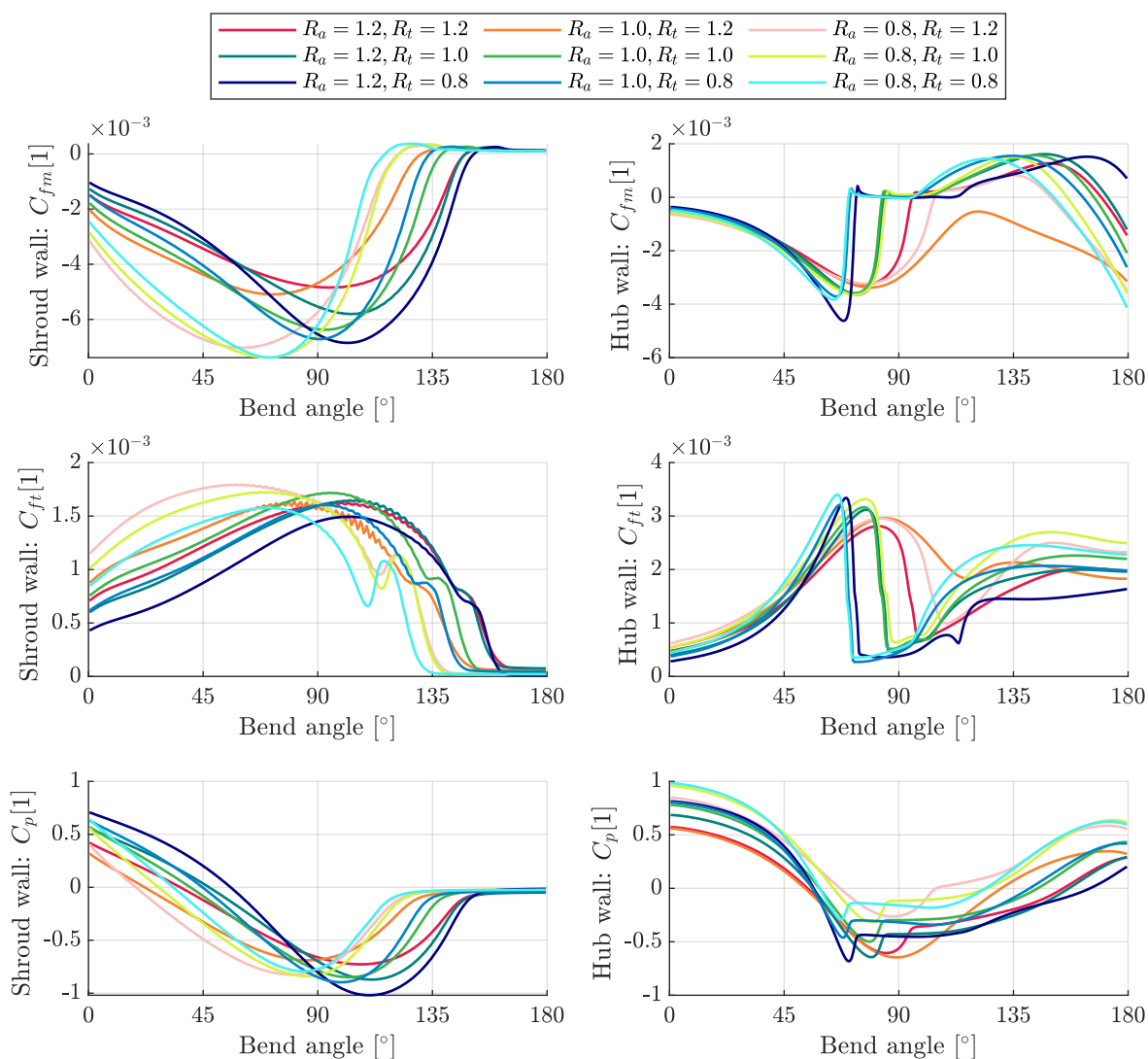
Figure 3.21: Coefficients of friction (meridional and tangential) and pressure at the channel walls for variable channel geometry.

Table 2: The critical inlet flow swirl angle α_{Icrit} for the modified geometries.

$R_a =$	1.2	1.0	0.8
$R_t = 1.2$	45.00°	47.61°	50.77°
$R_t = 1.0$	42.39°	45.00°	48.19°
$R_t = 0.8$	39.23°	41.81°	45.00°

Table 3: The ratio of the mean velocity magnitudes at the bend start to the bend apex.

$R_a =$	1.2	1.0	0.8
$R_t = 1.2$	2.00	1.8$\bar{3}$	1.6$\bar{6}$
$R_t = 1.0$	2.20	2.00	1.80
$R_t = 0.8$	2.50	2.25	2.00
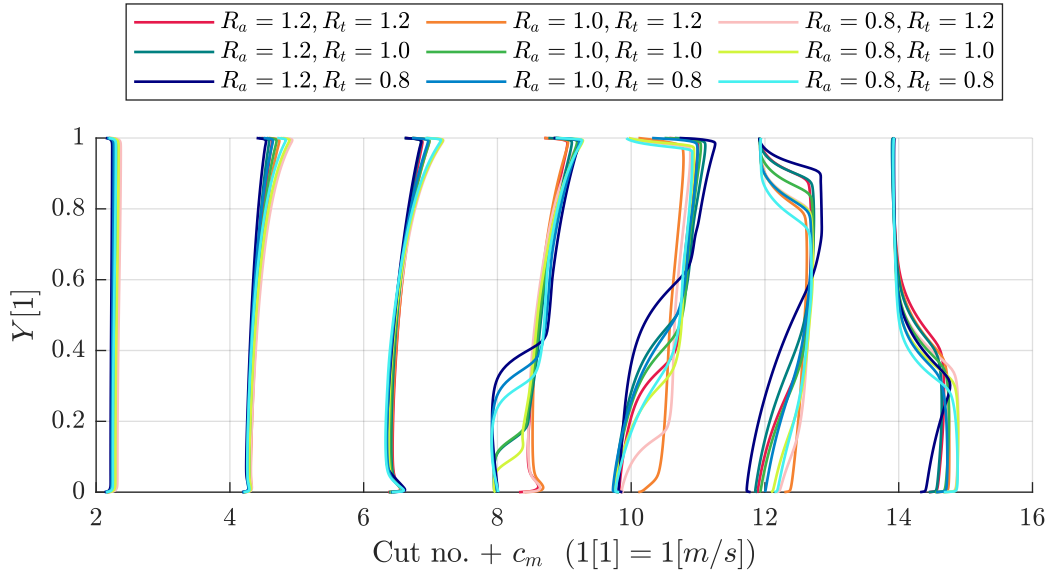
Figure 3.22: Meridional flow velocity profiles in channel cuts for variable channel geometry.

It is startling that the only case without hub side separation is one of the three $R_a < R_t$ cases, which has the lowest critical angle and also the highest predicted pressure gradient - the most unfavourable constellation of the three. The reason why the hub side boundary layer does not separate clearly must be an effect of the higher R_a compared to the two other cases. In the top left graph of Figure 3.21, a later flow separation from the shroud wall is observed (at $\approx 130°$ compared to $\approx 125°$ for the others involved). As well as in the different cases the location of the shroud side separation affects the hub side reattachment, in the case of $R_a = 1, R_t = 1.2$ the fast stream directed against the hub wall suppresses the late hub side separation.

Another interesting comparison is found amongst the three cases where $R_a = R_t$ (red, mid-deep green, cyan). Although the critical angle and the pressure gradient predictions allow the assessment of the phenomena concurrently influencing the flow field, they fail to distinguish between the absolute values of the geometrical simplexes. All three compared cases take on the same values of α_{Icrit} and the flow area contraction ratio, but their behaviour is significantly different.

The finer resolution of the horizontal axis of Figure 3.21 compared to Figure 3.17 allows to distinguish the dispersion of the tangential friction at the beginning of the shroud side recirculation zones. This might be an effect of the counteracting forces of the adverse pressure gradient versus the tangential rotation centrifugal force. This is probably the zone where maximum solution residuals occur. Comparing the different geometries, it is clear that the dispersion is the strongest in cases where both R_t and R_a are high.

Lastly, some conclusions can be drawn from the real stage geometry approximates.

The s2 stage is on the side of high R_t, low R_a, which could result in an abrupt shroud side separation (at least in the bladeless channel) but the hub side boundary layer should be resistant to separation up to very high swirl angles.

The s4 stage possesses very high values for both of the geometrical simplexes (the result of a narrow channel). This could help to shift the possible boundary layer separations further streamwise. As the values of the simplexes are not far apart, the critical swirl angle is actually in between the $R_a = 0.8, R_t \in \{1, 1.2\}$ cases.

3.4.2.6 Study of the influence of the Reynolds number

The base value of the Reynolds number of 10^6 was supplemented with the values of 5×10^6 and 5×10^5. None of the cases exhibited a diminishing of the recirculating flow at the hub wall at $\alpha_I = 45°$. The friction and pressure coefficients are shown in Figure 3.23.

The higher Re caused minor quantitative changes compared to the original case. It narrowed the hub side recirculation in the streamwise direction. The velocity profiles are smoother and have gentler spanwise gradients, see Figure 3.24. All of these effects seem to be favourable for the compressor operation.

The lower Re caused an earlier separation of the flow from the shroud wall. It occurred near the bend apex, even without the support of the adverse pressure gradient present in the aft part of the channel. This leads to a much less favourable distribution of the tangential velocity across the channel right behind the apex, as seen in Figure 3.24. Overall, the velocity profiles are sharper and more uneven for the low Re. Due to the higher viscosity, the turbulent mixing (momentum diffusion) is less intensive.

The low Reynolds number is certainly an unwanted circumstance when the intensive flow separation is inevitable. The results presented in this paragraph do not mention the abilities to support or suppress the hub side separation. As the separation was confirmed to be driven by inertial, centrifugal forces, Re can actually act suppressively to the formation of separation.

3.4.3 Analyses of real compressor channel approximates

After conducting a general parametric study with a free choice of inputs, the geometry is now fixed to two cases. They resemble the shape of the real compressor stages s2 and s4. Lower swirl angles are omitted.

The Reynolds number proved to be an important parameter and it is the only parameter related to the real compressor flowrate. The number of its values is enlarged to 4. These are picked based on the results shown in subsection 3.3.2, Figure 3.7. This set of values relates to the operating points at Mach number values low enough for sensible incompressible calculations. Note that the Reynolds number is evaluated from the absolute flow

University of West Bohemia, Faculty of Mech. Engineering   Dissertation thesis 2022/23

Department of Power Systems Engineering   Ing. Lukáš Hurda
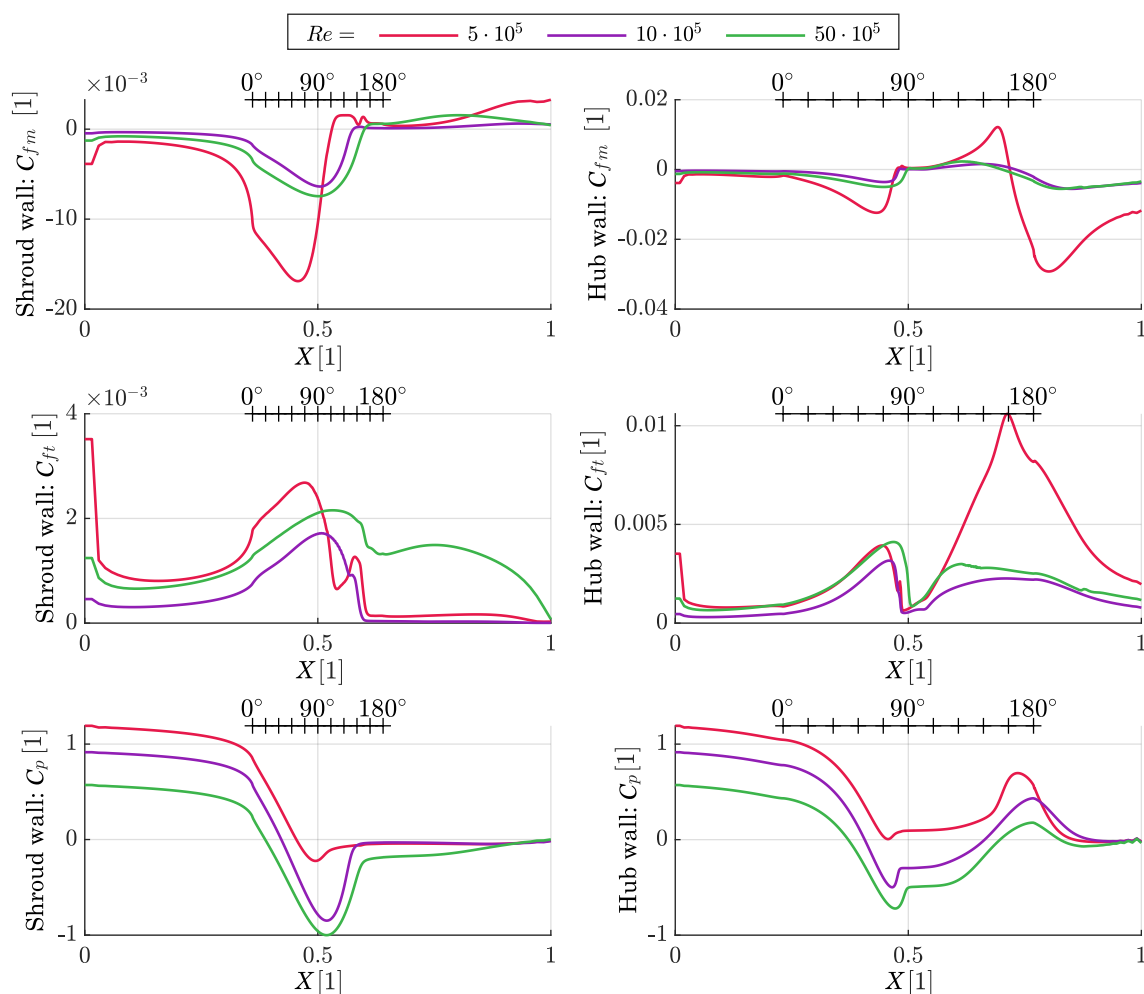
Figure 3.23: The coefficients of friction (meridional and tangential) and pressure at the channel walls for a variable mean Reynolds number in the bend apex.
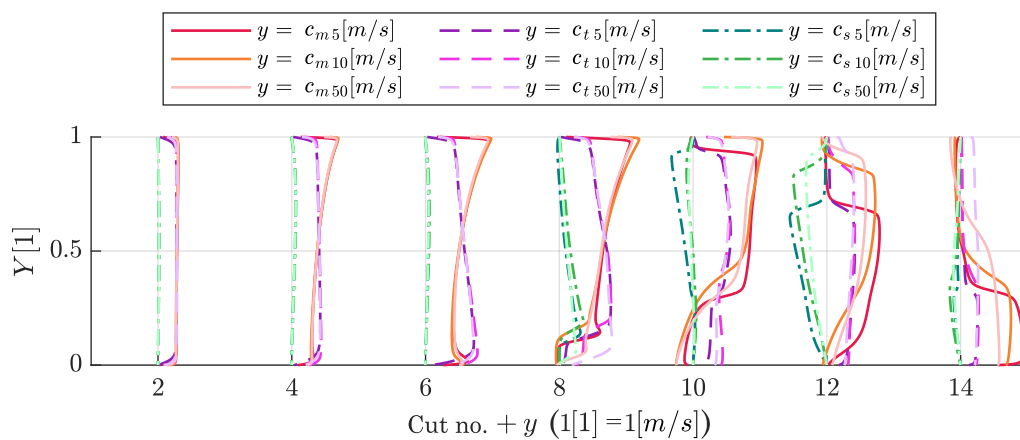

Figure 3.24: The velocity component profiles in the channel stations for the variable Reynolds number. (The number in the subscript of the legend entries equals $Re \times 10^{-5}$).

velocity magnitude, so the swirl angle has to be taken into account: $Re \cos \alpha_I$ is directly proportional to the compressor flowrate.

Figures 3.25 and 3.27 prove that the influence of the Reynolds number on the position of the hub side flow separation and the recirculation zone streamwise width is not uniform. The previous assessment of the Reynolds number influence, in paragraph 3.4.2.6, uses significantly higher values of Re. The effect of raising it seems favourable as it tends to make the hub side recirculation zone narrower and both of the wall separations begin farther downstream.

However, in the s4 stage geometry (Figure 3.27), the lowest simulated $Re = 3 \times 10^4$ eliminates the hub side separation altogether. It does not even feature the shroud side separation for either of the swirl angles (see Figure 3.28). As the Re grows above this value, the hub side separation emerges at $\alpha_I > 45°$. The position and width of the recirculation zone show only a weak dependence on the Re. The shroud side separation is present at all except the lowest Re at all of the swirl angles. It consistently shifts downstream with increasing angle and Re, but is nearly identical for the cases at $\alpha_I \in \{40°, 45°\}$. The location ranges from 137° to 169° of the channel bend angle.

The s2 geometry (Figure 3.25) gives consistent results with respect to the swirl angles with just two outliers at the lowest Re. The shroud separation is always present - the shroud axial curvature is very high. The hub separation gets wider at a constant angle and a growing Re until the highest value, where the trend is reversed. The unexpected behaviour at $Re = 3 \times 10^4$ is that the flow separates from the hub at 50° and 60° of swirl, but not at 55°. The recirculation zones in both of these cases are barely noticeable in the channel cross section Figure 3.26. They have very low profiles and therefore it do not effectively block the flow. The alternation of the occurrence of separation here is only due to the intrinsic uncertainty of the numerical simulation.

The critical angle concept is more or less confirmed here - generally, the s2 features the hub side separation when $\alpha_I > 54.77°$ and for the s4 the criterion of $\alpha_I > 49.85°$ is valid, with the exception of the lowest studied Re.

3.4.3.1   An attempt at compressible flow simulation in the simplified channel

It is logical to continue the simplified bladeless channel analysis of the compressor operating points lying above the Mach number limit for the compressible flow. The dimensional analysis laid out in subsection 3.1.2 is used to extend the set up used earlier for that purpose. In `OpenFOAM`, the case is defined using this set of parameters via the `thermophysicalProperties` dictionary: `molWeight` as M, `Cp` as c_p, `mu` as μ, `Pr` as Pr. `p`, `T`, `U` (p, T, c) are defined via the inlet and outlet BCs. `rho` (ρ) is imposed using the initial condition throughout the domain. A fixed value is also referenced by the mass flow outlet. The inlet condition is defined by the direction of the velocity vector and a fixed static pressure.

University of West Bohemia, Faculty of Mech. Engineering   Dissertation thesis 2022/23

Department of Power Systems Engineering   Ing. Lukáš Hurda

Stage s2
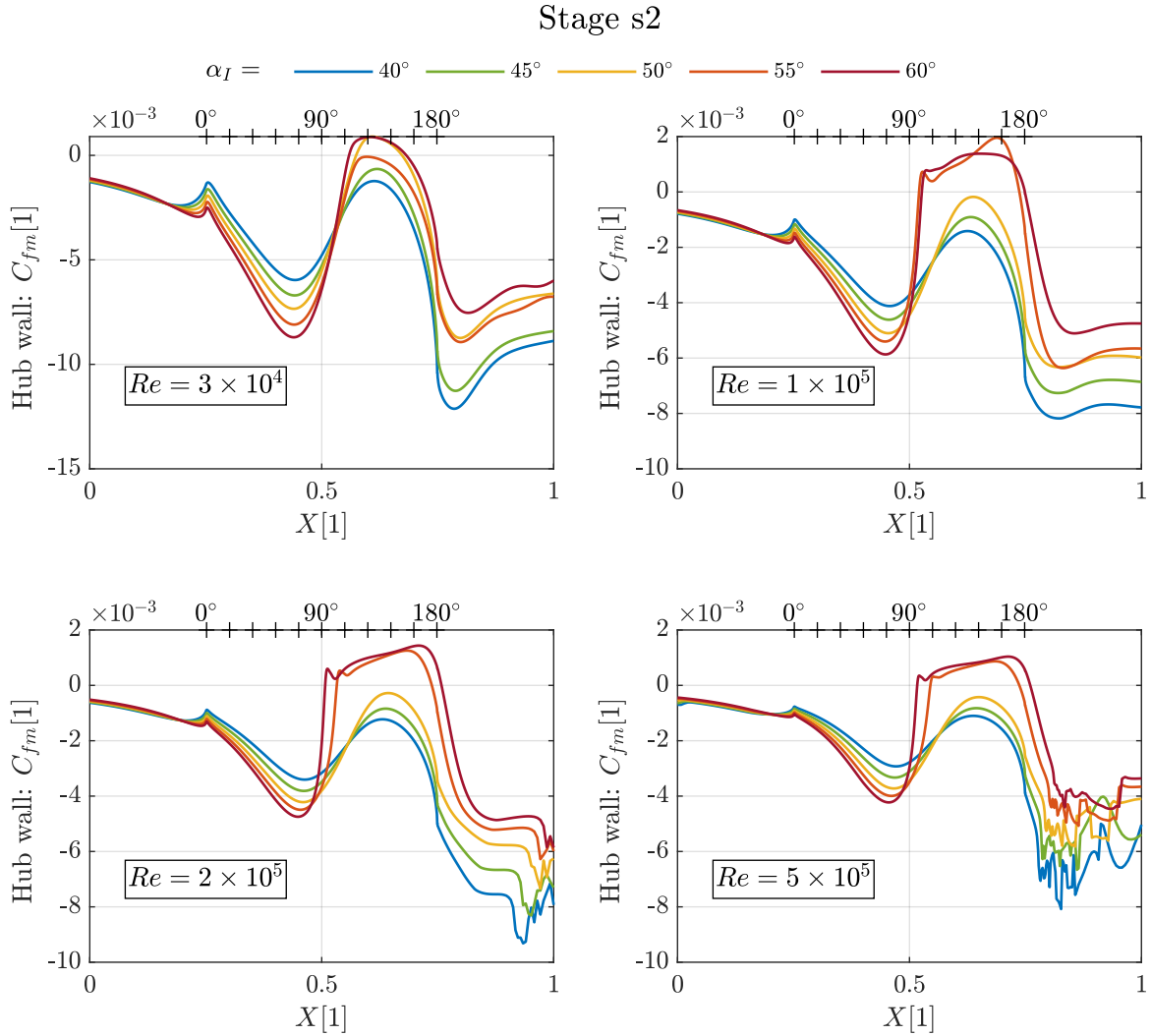
Figure 3.25: Coefficients of meridional friction at the hub channel wall for a variable bend apex Reynolds number and inlet swirl angle for the s2 stage.

To find the values of these mostly dimensioned parameters and keep the generalized format of the simulation ($c = 1\,\mathrm{m\,s^{-1}}, b = 1\,\mathrm{m}$) is much more complex than only tuning the Reynolds number with the kinematic viscosity. A set of equations, some nonlinear, is solved numerically. Common sense suggested, and experience has shown, that to find realistic values of the thermophysical and state parameters of the gas, the initial inputs must be adapted accordingly. The most sensible choice was to consider $c = 100\,\mathrm{m\,s^{-1}}$. `OpenFOAM` has the universal gas constant fixed internally to $R = 8314\,\mathrm{J\,kg^{-1}\,K^{-1}}$, so this value is also introduced in the author's calculations. Among other original non-dimensional

University of West Bohemia, Faculty of Mech. Engineering   Dissertation thesis 2022/23

Department of Power Systems Engineering   Ing. Lukáš Hurda
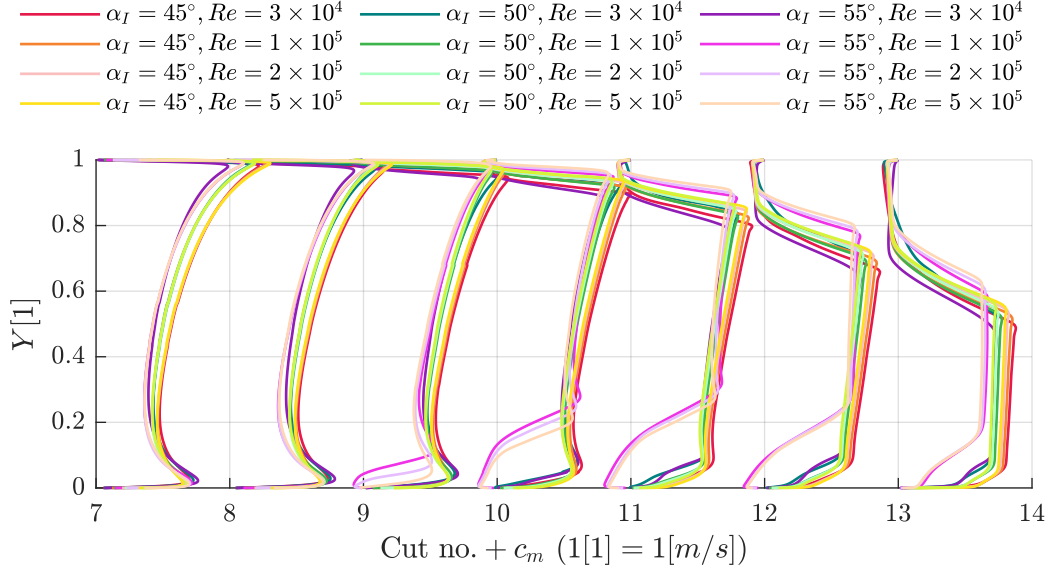
Figure 3.26: Selected meridional velocity profiles for variable bend apex Reynolds number and inlet swirl angle for the s2 stage.

criteria, Ma and κ are selected to be fixed and used to build the non-linear equations:

$$Ma = \frac{U}{\sqrt{\kappa R/MT}} \tag{3.17}$$

$$\kappa = \frac{-c_p M/R}{1 - c_p M/R} \tag{3.18}$$

Using these two equations together with initial estimates of p, T, M, c_p in `Matlab`'s `fsolve` function, the 4 estimated parameters are adjusted to conform to the desired Ma and κ. The density can then be evaluated from the perfect gas EoS. The dynamic viscosity μ is fixed by the desired Re and selected values of b and c.

All of these parameters are evaluated in the bend apex and need to be adjusted for their respective locations within the inlet or outlet BCs. This not only involves the velocity change due to flow area change as in the incompressible cases but also the change of gas state. Another non-linear equation is built and solved to obtain the inlet density (written in a form used for the numerical solution by minimizing the right hand side), at this point, only ρ_I is an unknown:

$$0 = c_p T_{apex}((\rho_{apex}/\rho_I)^{1-\kappa} - 1) - \frac{c_{apex}^2}{2} - \frac{1}{2}\left(\frac{A_{apex}c_{apex}\rho_{apex}}{A_I\rho_I}\right)^2 \tag{3.19}$$

When ρ_I is set, c_I, T_I, p_I can be expressed from the continuity equation, adiabatic state change relation and the EoS respectively. By similar means, the reference density at the outlet can be computed.

University of West Bohemia, Faculty of Mech. Engineering   Dissertation thesis 2022/23

Department of Power Systems Engineering   Ing. Lukáš Hurda

Stage s4
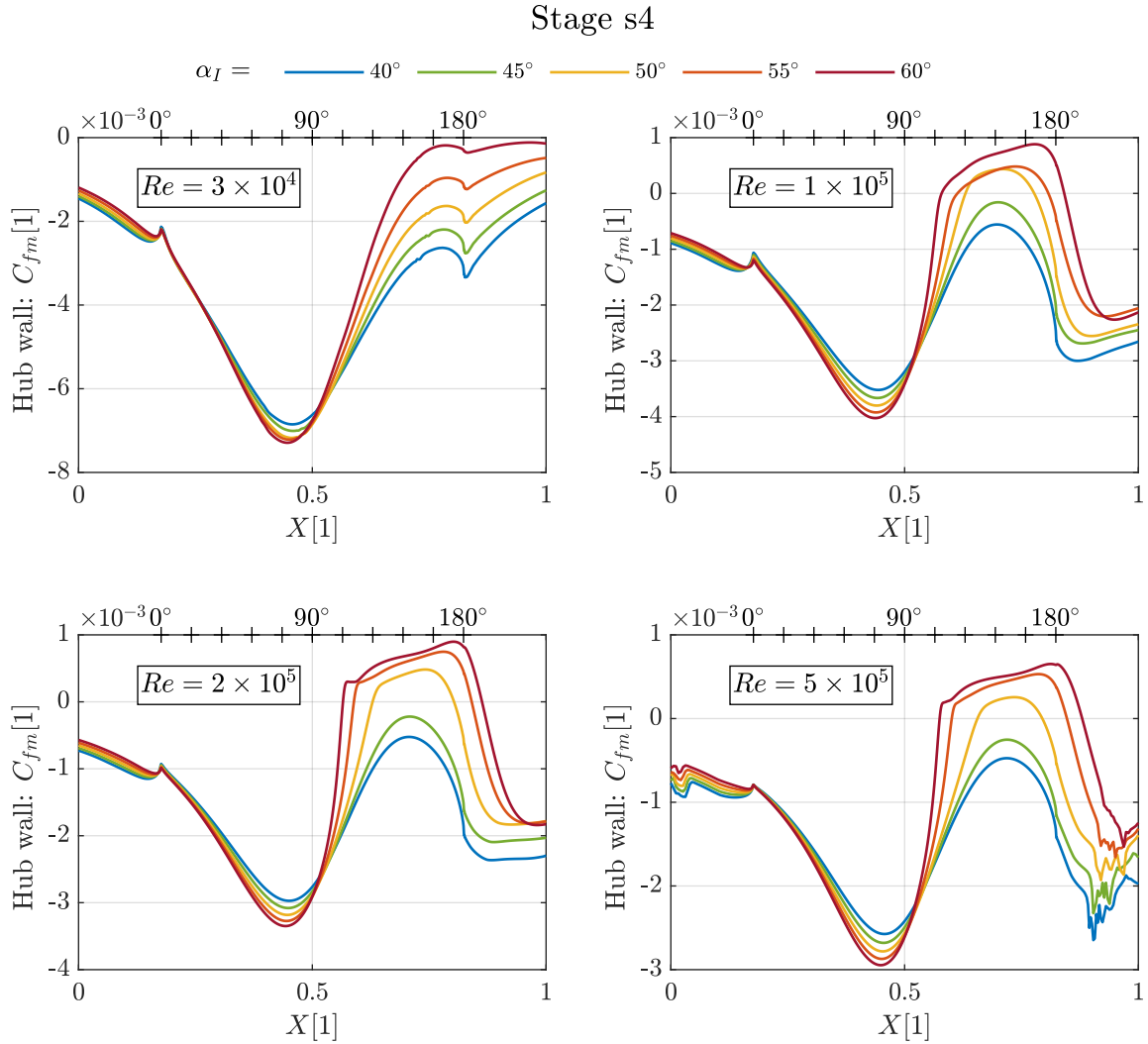
Figure 3.27: Coefficients of meridional friction at the hub channel wall for a variable bend apex Reynolds number and inlet swirl angle for the s4 stage.

An example of the resulting constellation of bend apex parameters is given below for fixed $Ma = 0.2, Re = 2 \times 10^5, \kappa = 1.4, U = 100\,\mathrm{m\,s^{-1}}$ and the initial values of variables specified as $p = 10^5\,\mathrm{Pa}, T = 293.15\,\mathrm{K}, M = 29\,\mathrm{kg\,kmol^{-1}}, c_p = 1000\,\mathrm{J\,kg^{-1}\,K^{-1}}$:

Table 4: Calculated inputs of the compressible inlet channel flow analysis.

p [Pa]	T [K]	M [kg kmol^{-1}]	c_p [J kg^{-1} K^{-1}]	ρ [kg m^{-3}]	μ [m^2 s^{-2}]
10^5	567.43	26.419	1101.5	0.56	2.8×10^{-4}

University of West Bohemia, Faculty of Mech. Engineering   Dissertation thesis 2022/23

Department of Power Systems Engineering   Ing. Lukáš Hurda
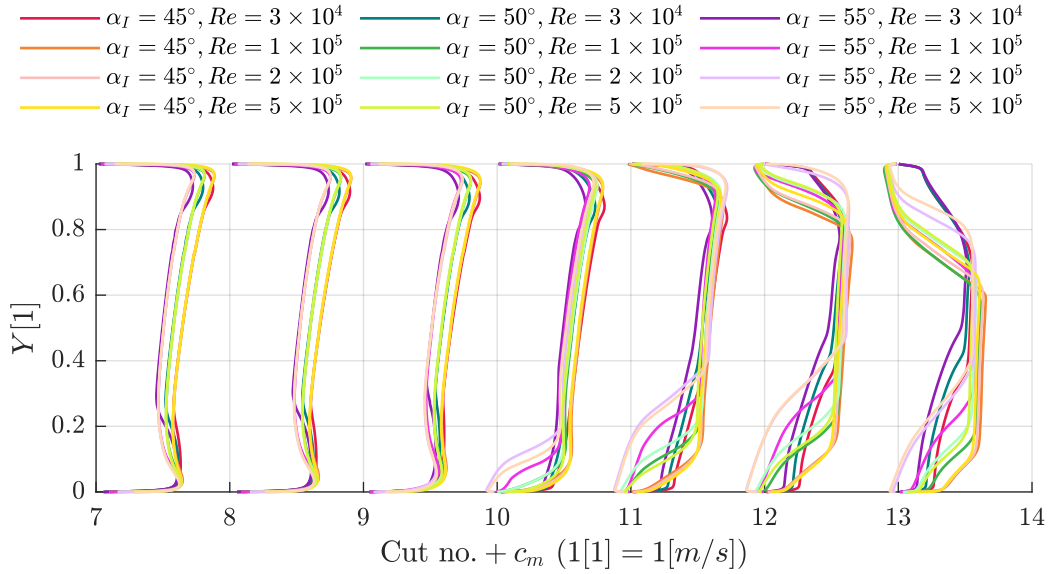
Figure 3.28: Selected meridional velocity profiles for variable bend apex Reynolds number and inlet swirl angle for the s4 stage.

The results presented in Table 4 are a reasonable compromise of keeping convenient values of dimensional and velocity scales while using quite realistic values of the thermo-physical properties and the state parameters.

Unfortunately, the compressible simulations within `OpenFOAM` were not successful. The computations were not stable - the large adverse pressure gradient area in the second half of the bladeless channel model is believed to cause this instability. When the domain was shortened down to the end of the channel bend (the straight radial part of the channel was stripped on the outlet side only), the solution became stable and also showed an acceptable level of convergence. The segregated solvers featured in `OpenFOAM` toolbox may be less robust than the pressure-velocity coupled variants used in `Fluent` and other simulation software. It has not been tested whether a coupled solver would be capable of a convergent solution in these compressible cases.

The compressible analysis of the simplified bladeless channel was deemed unimportant in the context of the amount of useful information gained from the incompressible analysis and the outlook for the planned full turbomachine simulations.

3.4.4   Simplified bladeless channel model conclusions

A wide range of regimes of the swirling flow through the simplified bladeless channel was simulated and assessed.

It was confirmed that the flow swirl angle is a fundamentally important parameter. The concept of the critical swirl angle first introduced in subsection 3.1.1 bounds the hub side separation limit with the channel geometry criteria. The results confirm, that this could be a very direct and concise parameter for predicting the behaviour of certain channel geometry as the results are mostly in accordance with the critical angle predictions. Still, a flow criterion independent of geometry - the Reynolds number (as defined with variable R_t, R_a curvature simplexes and constant channel width b) introduces another degree of freedom into the system. There are, however certain differences between cases with identical critical angles but different values of the geometry parameters.

Low Reynolds numbers cause less intense mixing and momentum transfer across the channel and the boundary layers. It can suppress the separation, but once the flow is separated, the results do not show a clear or even uniform trend in the various indicators of the flow field uniformity. These various counteracting effects, including flow blockage by the recirculation zone or its location, may be the key uncertainty resulting in the unpredictable nature of the compressor instabilities.

The incompressible analysis provided the basis for all of these findings. The laborious implementation of the compressible model within the laid out framework is not worth the small amount of additional information acquired. It is not crucial to study the compressible effects on the simplified model when it is clear that it will never fully correspond to the real machine geometry.

As stated in section 3.3, the s2 stage did not suffer from any significant unforeseen performance loss anywhere in the compressor map. Besides the formation of the hub side separation at higher flow swirl angles, the bladeless channel equivalent of this stage does not behave any better than the s4 stage bladeless channel. It may even be worse in terms of the shroud side separation intensity. It becomes clear that the interaction of the inlet flow with the impeller is crucial to finding the source of the instabilities. The s2 impeller is capable of handling the inlet channel geometry prone to adverse flow effects, while the s4 impeller is not.

3.5 IGVs CFD model

The operation of the IGVs alone is assessed below. Only the s4 stage is selected for this analysis. The main goal is to determine the flow deviation angles at their trailing edge and the behaviour of the wake. The resulting exit angles are to be used in the boundary conditions of the compressor model excluding the IGVs. This helps to mitigate the complexity of the workflow by only resetting BCs instead of using different geometries and meshes for each IGVs stagger angle.

Modifications to the basic model are applied: First, the effect of decreased vane thickness is examined and then the rotation of the hub and shroud wall in the region of the impeller placement is studied.

3.5.1   Model description

The simulations were carried out in `Fluent`. The geometry is based on the hub and shroud curves digitized from the blueprints of the actual s4 stage. The NACA 0012 profile curves were generated at a proper scale, orientation and location via a `Matlab` script. The initial variant (incorporating the real machine geometry) uses the default profile thickness to chord ratio of 0.12. The blueprints also specify the radius of the rounded trailing edge (TE). The NACA profile is defined with a perfectly sharp TE. Such an original profile is modified by the script to incorporate the round TE and not alter the total chord of the airfoil profile.

The fixed diameter TE circle placement is found by searching for a point at which a tangential connection with the blade profile is achieved. The profile points located behind this connection are then deleted, as well as the portion of the circle located inside the profile. The whole profile is then rescaled to meet the original chord length. The difference in the chords before and after the implementation of the TE circle is small, therefore a correction of the profile thickness is not applied after the scaling.

The hub, shroud, hub-profile and shroud-profile curves were imported into `TurboGrid`. 3D geometry and a mesh were generated. The geometry omits any clearance between the adjustable vanes and channel walls as well as all the other fine geometry features. These include the inside corner rounding in the area where the vane joins its pivot and the notch in the vane face around the pivot.

The tangential domain bounds are determined automatically by `TurboGrid` in order to help generate a smooth and orthogonal mesh. A section containing just one of the 20 vanes is meshed. As the periodic boundaries are conformal, the meshing settings can easily be modified to produce more consecutive interblade channels.

The resolution of the mesh is determined by the desired y^+ at the predefined Reynolds number. The global mesh size parameter is increased above 1 to allow for nuances in the definition of the Re prescription.

The flow is considered compressible for consistency with the models of the entire compressor. Although the Mach numbers in the centripetal channel will be low, the domain extends down to the channel bend apex (and behind it). There, higher Mach numbers are expected.

The measured operational points of the real machine were examined to determine the setting of boundary conditions. The full set of the stagger angle settings was reduced to 15°, 30°, 45°, 60°. Obviously, the compressor reaches different flowrates at different IGVs settings. The ratio of the flowrate to the nominal value is shifted by steps of 0.15 between 0.25 to 1.45. At the lowest flowrates, a 0.05 step is adopted - between 0.05 and 0.20 of the nominal flowrate ratio.

University of West Bohemia, Faculty of Mech. Engineering   Dissertation thesis 2022/23

Department of Power Systems Engineering   Ing. Lukáš Hurda
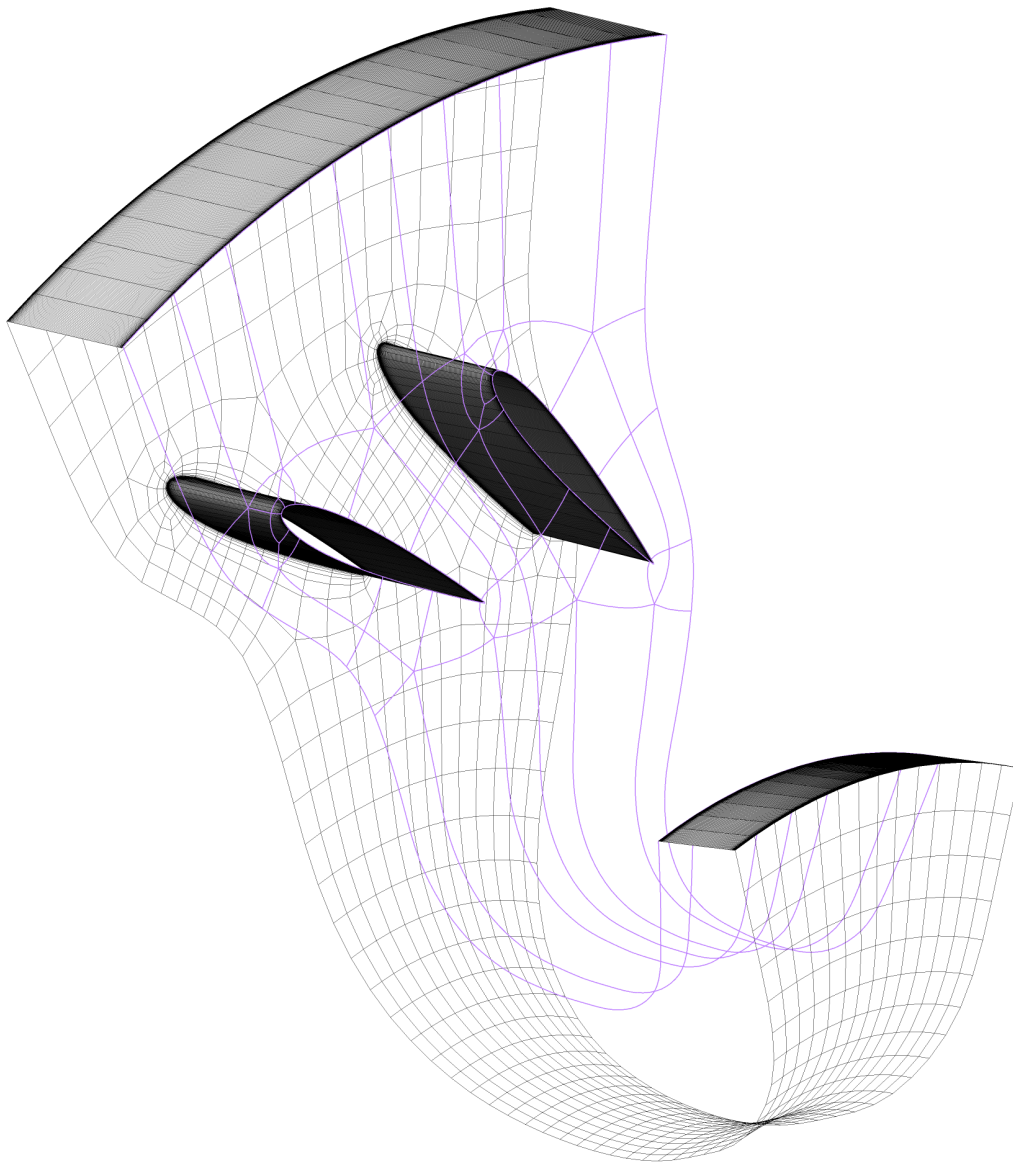
Figure 3.29: IGVs model at 45° stagger: computational domain (including one periodic duplicate), mesh blocks topology and mesh illustration (coarsened for clarity).

It is worth noting that this setup is partly different from the approach used in the previous section 3.4. While comparing cases with the same flowrates and different stagger angles, the Reynolds number is not equal. It is defined based on the expected absolute velocity in the bend apex, but the flowrate directly controls the meridional component of velocity only. At an identical flowrate, Re gets higher with increasing flow swirl/IGVs stagger angle. Ma exhibits similar behaviour.

The boundary conditions were set to (total) pressure inlet - mass flow inlet combination. Most of the cases of the base geometry were stable and rapidly convergent in this setup. In some of them, a Mach number close to 1 was caused by the outlet condition, which resulted in some solution limiting by the solver. Two of the cases diverged due to this problem. A solution to this instability was to switch the BCs to a mass flow inlet - (static) pressure outlet pair. This requires a determination of the outlet pressure, which should ideally yield a similar total pressure at the inlet as the initially specified value. An approximation was made by neglecting the flow compressibility. The final value of static pressure to be prescribed at the outlet was evaluated by expressing the dynamic pressure change and also interpolating the total pressure loss from the successfully converged solutions of the other cases. The dynamic pressure change is an effect of the flow area change in the assumed undisturbed flow from the inlet to the outlet.

All the thin blade simulations were run using the mass flow inlet - pressure outlet combination, reusing the outlet static pressures simulated in the base case. A different pressure loss is expected, but the magnitude of the difference should not influence the close approach to the desired inlet pressure.

3.5.2   Post-processing techniques

The flow angles, Reynolds and Mach numbers were sampled and mass-flow-averaged at two locations. The first is the (cylindrical) iso-surface of the radial coordinate designated "$2IGV$" at which the TE is located for $\vartheta = 0°$. This is also the location at which the deviation angle δ is evaluated. The second location is in the bend apex (planar iso-surface of the axial coordinate).

A planar surface slicing through the centripetal channel part involving IGVs is constructed normal to the machine axis. The radial velocity is sampled on this plane to show the possible boundary layer separation from the guide vane surface and also to indicate the length, shape and intensity of the wake of the IGVs, see Figure 3.32 along with the comments below. In the centripetal channel, the radial velocity values are mainly negative with the exception of the region near LE in the cases with a high angle of attack. Everywhere else, the positive value means backflow. The scales are clipped at $0\,\mathrm{m\,s^{-1}}$ to identify recirculation zones adjacent to the vane skin. The value of the minimum clip is adjusted arbitrarily to show the propagation of the wake through the flow field downstream of the TE with proper contrast. The blue-bound cropped regions do not have any special meaning.

The data plotted directly from the 3D CFD model use a periodic duplicate to show the flow field in a more continuous manner.

3.5.3   Results

All the deviation angles remain low due to the high cascade density, see Figures 3.30 and 3.31. Most of the studied cases are fairly independent of Re, but exceptions occur. At 60° stagger, the flowrate is so low that the Re is low enough to accentuate its own influence. Also, the thin IGVs show very low deviation angles at 45° of stagger. At all flowrates, the "Thin 45°" data subset does not follow the otherwise steady trend of the deviation increase along with the stagger angle. The deviation is also significantly lower than for the thick vanes at an equal stagger. This behaviour is justified by the suction side separation, whose behaviour can be observed in Figure 3.32. This figure shows six cases at an identical flowrate.

Amongst the six presented, all three thin IGVs cases (right) feature a suction side separation, while the base case only allows it at 45° of the stagger angle (mid-left). At this angle, the separation is especially large for the thin vanes, but the boundary layer still manages to reattach relatively soon, around mid-chord. This recirculation zone effectively decreases the deviation.

The small suction surface recirculation at the base vane ($\vartheta = 45°$) may diminish or enlarge at different flowrates. This uncertainty can cause the lower subjective smoothness of the deviation angle curve in Figure 3.30.

The flow swirl angle average (secondary vertical axis in Figures 3.30 and 3.31) increases between the IGVs TE and the bend apex stations in most cases. The trend is exactly the opposite for $\vartheta = 60°$ and for the largest of flowrates at 45°, regardless of the type of the IGV profile. The flow angle difference between the stations has a magnitude comparable to the deviation angle. The change in the swirl angle is a result of flow area and density changes as described by equation (3.11) (valid in the same form for any pair of stations). Density is always decreasing as the static pressure drops with flow area contraction towards the bend apex. Another phenomenon accentuating this is the total pressure drop due to friction. The channel width ratio between the two stations exhibits an opposite trend and it is a constant for a given stage. At 45° stagger and 145 % of the nominal flowrate, the pressure loss due to friction is high enough for the density ratio to overpower the influence of the channel width ratio.

The study of the vane wakes is limited to observations possible from Figure 3.32. None of the cases which are not shown in Figure 3.32 behave significantly differently considering the vane wake. The ever-present reattachment of any boundary layer separated from the vane skin excludes the possibility of a massive turbulent wake pattern typical for a stalled flow around isolated airfoils. Despite that, the inevitable velocity drop in the wake is clearly distinguished in the radial velocity contours. Since the flow in the vaneless channel was proven unstable, even a moderate wake can alter the behaviour of the hub side separation. It is apparent from the contour plots that the diffusion of the wake happens gradually along the streamlines. Therefore the magnitudes of the velocity drop across the wake observed

University of West Bohemia, Faculty of Mech. Engineering   Dissertation thesis 2022/23

Department of Power Systems Engineering   Ing. Lukáš Hurda
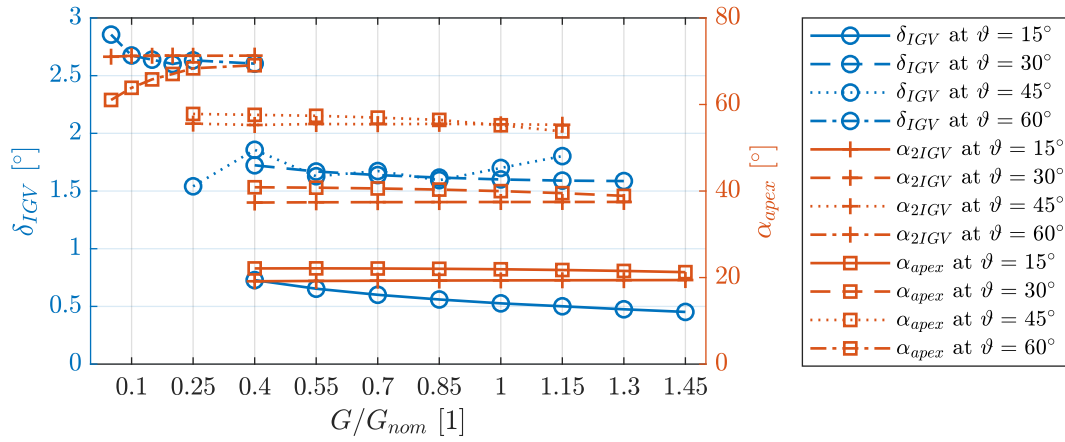
Figure 3.30: Results of the flow deviation and absolute angles in the base IGVs model.
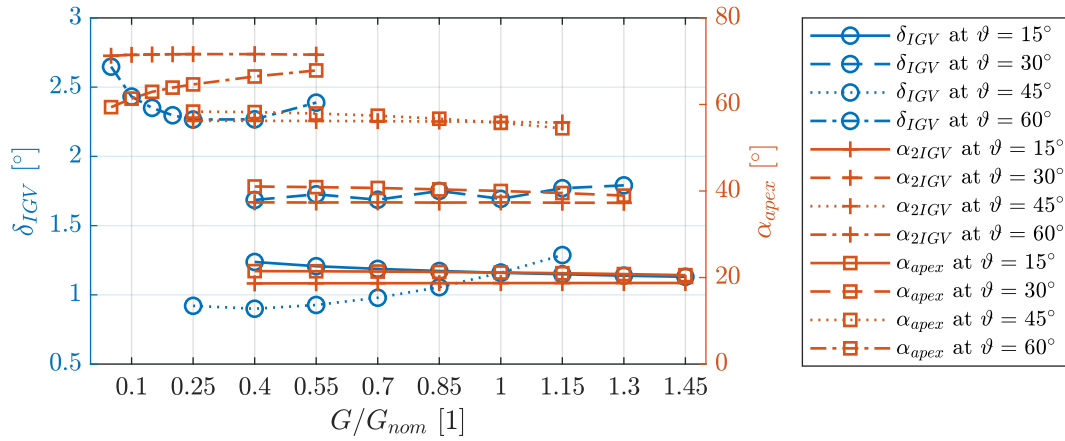
Figure 3.31: Results of the flow deviation and absolute angles in the thin IGVs model.

in the bend apex are much lower at high swirl angles. The bend apex Reynolds number (a measure of the absolute velocity magnitude) is shown in Figure 3.35 for the base IGVs, but the diminishing of the wake at 60° stagger is also obvious from Figure 3.32. The apex contours of Re show that this flow field profile is strongly affected by the possible IGVs wakes as well as the hub side separation position and intensity.

Generally, the flow pattern in the channel bend is controlled by the stagger angle with minor discrepancies amongst different flowrate instances. 15° causes relatively small, low blockage recirculation zones at both channel walls in the aft-most part of the domain. At 30°, a massive separation from the aft part of the shroud emerges. At 45°, a massive hub side separation is present, but the onset point is well behind the bend apex. At 60°, the hub separation starts in front of the bend apex and it blocks most of the channel flow area. That is the reason for the mean flow angle decrease between the stations $2IGV$ and $apex$. The velocity field can be further examined in appendix A.

University of West Bohemia, Faculty of Mech. Engineering   Dissertation thesis 2022/23

Department of Power Systems Engineering   Ing. Lukáš Hurda
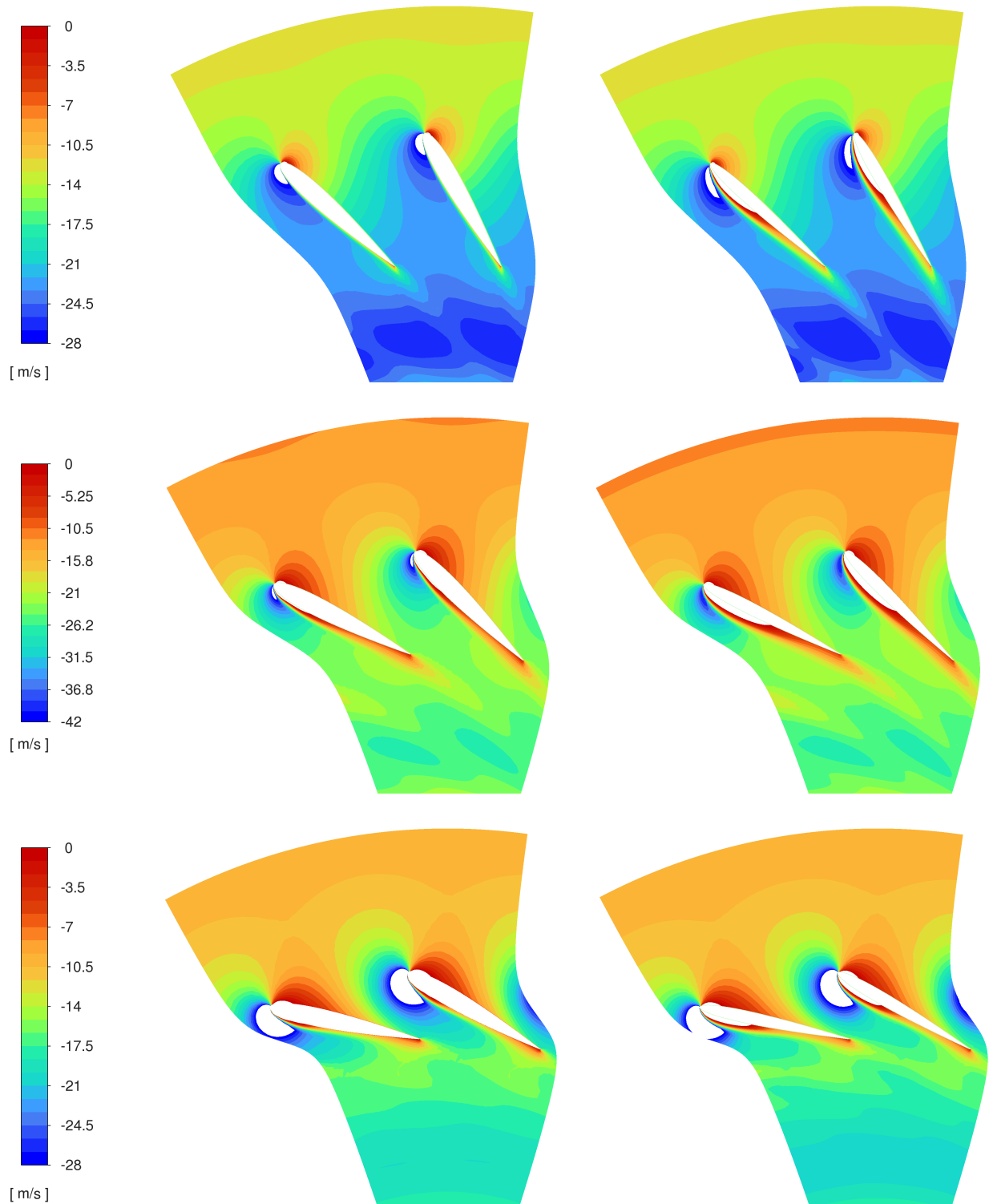
Figure 3.32: Radial velocity contours for $G/G_{nom} = 0.4$ at the centripetal channel mid-span. Left: base IGVs. Right: thin IGVs. Top to bottom: 30, 45, 60° stagger angle.

University of West Bohemia, Faculty of Mech. Engineering   Dissertation thesis 2022/23

Department of Power Systems Engineering   Ing. Lukáš Hurda

The pressure losses overview is given in Figure 3.33. It shows the thin vane profile is only beneficial at low stagger - at 30° and above, the losses of the base vanes are lower.

The pressures of the earlier selected six cases at $G/G_{nom} = 0.4$ are examined in detail, see Table 5. The table is compared with the radial velocity contour plots. It is apparent that the flow blockage caused by the vane itself plus the thickness of the eventual recirculation zone is the key factor in the determination of the resulting pressure loss. The relatively large abnormal difference between the base and thin vane cases at 45° stagger may be enhanced by this effect as the lower deviation increases the swirl angle. The increase in the absolute total pressure loss Δp_t in the base to thin vane profile comparison is by far the highest at 45°. The higher the swirl angle, the higher the absolute distance along which a flow particle travelling along the wall experiences the friction force. In other cases of base to thin vane comparison, where deviation of the base vanes is lower than the thin ones, this effect is marginal and does not cancel out the higher flow blockage effects from the separated flow along the thin vane suction side.

Another observation in Table 5 is the departure of the resulting inlet total pressure p_{tI} from 10^5 Pa in the thin vane cases. It is caused by the setting of the outlet pressure BC based on the respective base vane simulations. The discrepancies are negligible for 30° and 45° and acceptable for 60° stagger angle.
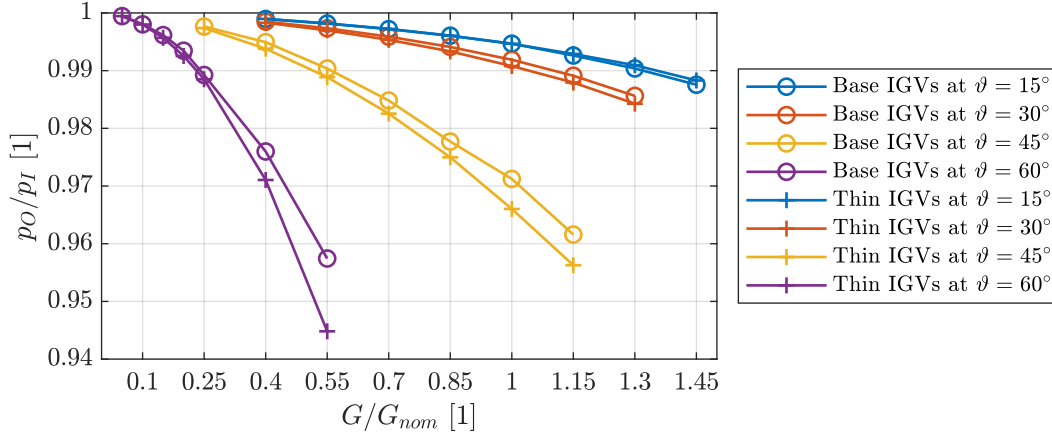
Figure 3.33: Results of the total pressure ratios.

Besides the parameters of the IGVs, some observations can be made here to compare the results obtained in previous analyses - be it the measured data, the mean flow calculations or the simplified channel analysis. It may be simpler to draw some of the conclusions here, where the impeller is still not considered, so its rotational speed does not present another parameter of the study. Only the base IGVs cases are shown, as there is no significant difference in the data from the thin variant. The flow criteria evaluated in the bend apex are plotted in Figure 3.34. It can be compared with Figure 3.7: The CFD values are generally lower than those estimated from the measurement. Mach number

University of West Bohemia, Faculty of Mech. Engineering   Dissertation thesis 2022/23

Department of Power Systems Engineering   Ing. Lukáš Hurda

Table 5: IGVs relative and absolute total pressure losses at 40 % of nominal mass flow rate.

	30° Base	30° Thin	45° Base	45° Thin	60° Base	60° Thin
p_{tO}/p_{tI} [1]	0.998	0.998	0.995	0.994	0.976	0.971
p_{tO} [Pa]	99 849	99 886	99 493	99 609	97 599	95 167
p_{tI} [Pa]	100 000	100 056	100 000	100 230	100 000	98 004
Δp_t [Pa]	150.8	170.1	506.2	621.5	2401	2837
$\Delta p_{tBase}/\Delta p_{tThin}$ [1]	...	1.128	...	1.228	...	1.182

estimations seem to be more precise than the Reynolds number. There is no alarmingly high discrepancy, which would render the measurement estimation useless. There is an interesting trend in the CFD data for Re_{apex} - at higher IGVs stagger angles, the curve is concave, while the measurement data always form a convex shape. This is probably due to the limited precision of the estimations made in the measurement evaluation, which cannot correctly describe the mean flow without considering the complex flow field generated in CFD. This is especially pronounced in cases with massive hub side separation and higher absolute velocities. It is still a question whether the flow pattern will be similar in the apex station when a rotating impeller is introduced.
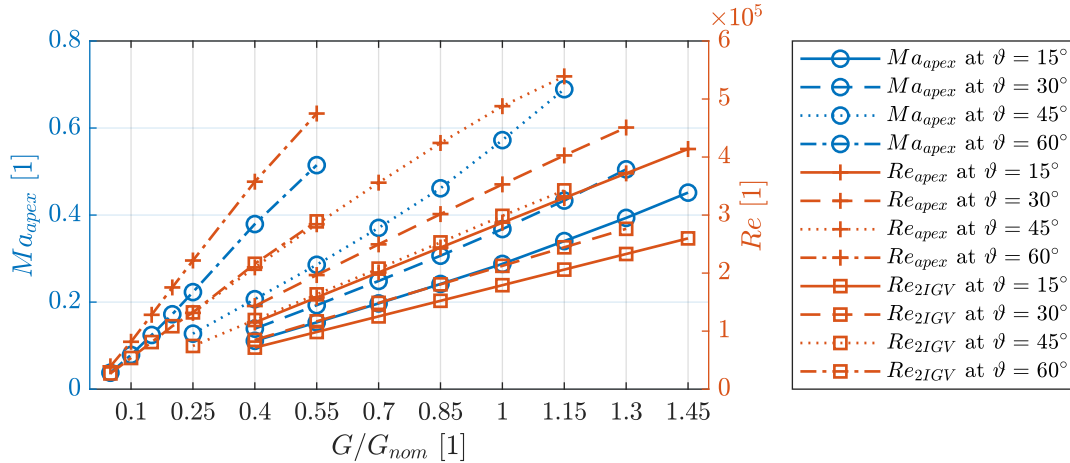
Figure 3.34: Results of the flow criteria from the base IGVs cases.

The Figure 3.35 has already been mentioned, but the reason why the Reynolds number was specifically plotted is to discuss the relation of the mean values from Figure 3.34 with the spatial distribution of this quantity.

An indirect comparison is performed between the IGVs model and the simplified channel model. Besides the compressibility or the vane stagger versus the actual flow swirl angle, the most notable difference between the models is the shape of the channel. In the real compressor channel used in the IGVs model, the aft part of the bend is narrowed. This

University of West Bohemia, Faculty of Mech. Engineering   Dissertation thesis 2022/23

Department of Power Systems Engineering   Ing. Lukáš Hurda
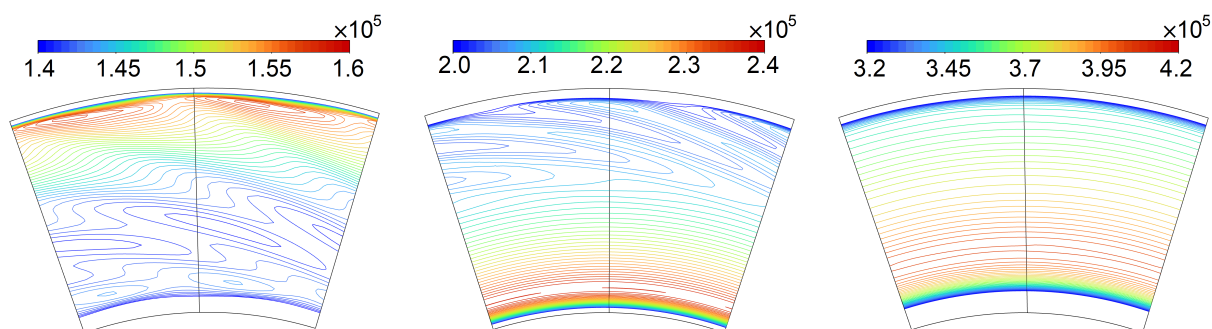
Figure 3.35: Reynolds number in the bend apex for base IGVs at $G/G_{nom} = 0.4$. Left to right: 30, 45, 60° stagger angle.

should help relieve the adverse pressure gradient effects. The shape of the shroud allows for later separation from there. From the observations made in section 3.4 it is deduced that the late separation from shroud can cause larger and sooner detachment of the hub side boundary layer.

3.5.4   Conclusions from the IGVs model

The computation of the IGVs exit angles was crucial for setting up the compressor model, which involves just one row of blades - the rotating impeller ones (subsection 3.6.2). The solution does not omit the flow rate influence - the whole compressor operating range is analysed. At a constant viscosity, the flowrate is the parameter determining the Reynolds number.

The specific IGVs setup proved to be an effective and robust way to introduce swirl. The thick vanes from the real machine design performed better than the proposed design modification. The thin blades only exhibit a superior performance at low stagger angles. They still succeed in turning the flow at higher stagger, but the pressure losses become larger compared to the original NACA profile.

The doubts about the possible detrimental effects of the wake of the IGVs were refuted. None of the full range of operating conditions has caused a stall. The irregularity of the mean flow parameters in the channel bend apex is then assessed. The IGVs wakes introduce defects of moderate amplitude to the mean flow, but they might be enough to destabilize the fragile force balance in the bend apex.

University of West Bohemia, Faculty of Mech. Engineering   Dissertation thesis 2022/23

Department of Power Systems Engineering   Ing. Lukáš Hurda

3.6 Full compressor CFD models

3.6.1 Design of a substitute of the real impeller

The geometry was available only via blueprints, without comprehensive detail of the more complex shapes of the channel and the impeller blading. The approach of compressor redesign based on the nominal operating point and most of the geometry characteristics was embraced. The main reason for the redesign approach instead of blueprint data digitization is the doubt about the smoothness of the digitized curves. Even though the resolution of the blueprint is high enough and the manual digitization could be made very precisely, the discrete points would not form a continuous smooth curve whether piece-wise linear connections or higher order curves such as splines were applied. The sets of points would require complex treatment to achieve smoothness and on top of that, the resulting 2D blade profile data would require various complex scaling, projecting to hub and shroud surfaces etc.

The turbomachinery design software tool `multall-open` was provided with the design surface coordinates and the meridional velocity development. At this surface, the user sets the LE and TE radial and axial coordinates, the absolute flow angles at the stage inlet and exit and flow and power coefficients. The flow coefficient needs to be evaluated at the rotor LE. The rotational velocity of the rotor and the absolute flowrate are needed as well as an estimate of the thermodynamic isentropic efficiency. The hub wall is selected as the design surface and the meridional velocity distribution coefficients corresponding to the individual hub points are tuned to produce a shroud curve roughly of the same shape as the real compressor.

The inlet absolute flow angle for the design point is zero, the LE incidence angle is adjusted to a small positive value of $\tilde{2}.5°$ to line up the calculated inlet velocity triangle with the relative metal angle measured from the blueprint. The stage exit absolute angle (at the diffuser discharge) is calculated from the measured power, pressure ratio and mass flow rate.

There is no option to design a stage with a vaneless diffuser in `multall-open`, one can just exclude the vanes from the program output. The incidence and deviation of the diffuser vanes are kept at 0° and the radial chord of the vanes is set to a very short distance. The short chord results in a very low flow turning angle of the diffuser vanes. The low turning angle enables the linking of the rotor absolute exit angle to the stage exit angle. The deviation angle of the impeller blading is used to tune the meanline flow design calculation. A few iterations of the calculation lead to a deviation value which satisfies both the stage exit angle and the exit metal angle of the impeller blade.

The meanline calculation performed by `meangen` (a part of `multall-open`) produces a set of specific geometry parameters such as the blade camber angle and the thickness distribution, the LE and TE shape description and many others. This is an input to the

`stagen` program, which outputs the general 3D coordinates of the machine geometry in a cylindrical coordinate system. These data are processed by a custom `Matlab` script to generate the curve files for `TurboGrid`.

The rotation of the hub and shroud walls is specified to begin in the bend apex. This is consistently applied to both impellers used in the full compressor models. It does not correspond to the real s4 stage geometry, it is set up this way for the sake of consistency between the different impellers. However, it is common for the 2D-bladed rotors to extend the impeller hub and shroud relatively far in front of the blade LE.

The model omits all the secondary geometry features: blade to hub and shroud disc rounded corners, rotor seals and all the cavities between the stator and rotor. The hub and shroud surfaces are smooth in the models and in the real machine as well. This is not usual in many centrifugal compressors, but Howden ČKD decided to machine the hub and shroud to the same surface roughness as the blade surface in all their compressors.

The blade shape generated within `multall-open` has identical inlet and exit metal angles and diameters to the original s4 stage impeller, see Figure 3.36. The wrapping angle of the substitute impeller is slightly larger (circa 39.0° vs. 34.5°) and therefore the camber angle distribution is different too. The thickness is very similar (the inconsistent graphics methods used to draw the Figure may be misleading the viewer) and the cut-off TE is adopted as well.
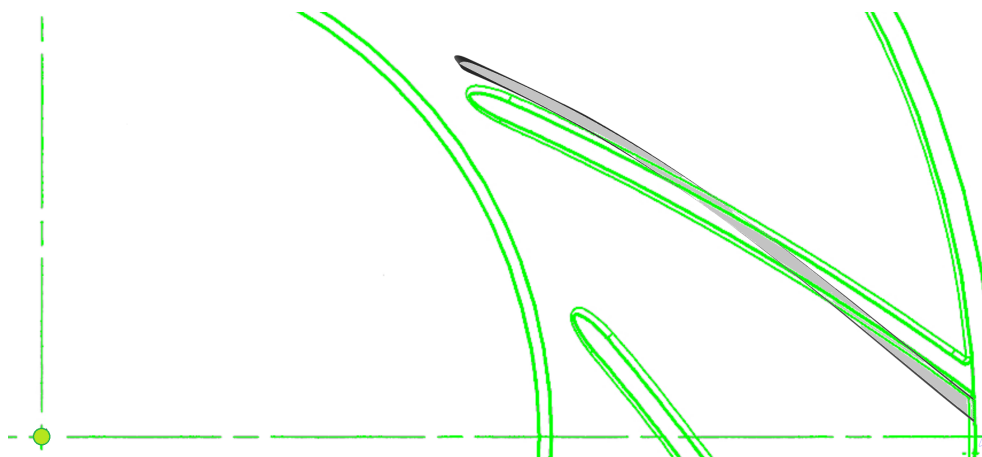

Figure 3.36: Original (green) and redesigned (black/grey) impeller blade profiles.

Two model variants are prepared:

- A model including no IGVs. The inlet flow swirl is introduced by the inlet BC.

- An entire model incorporating the IGVs.

3.6.2 Compressor model without IGVs

Three fluid domains are created: a static inlet channel (still fully extended upstream), a rotating impeller and a static diffuser, see Figure 3.37. Both domain interfaces are conformal, i.e. matching, no generalized turbo interfaces are necessary. The only numerical error possible at these interfaces is the transfer of the information from the static reference frame of the inlet channel to the MRF in the rotor and from the rotor to the stationary diffuser. The interface between the rotor and the diffuser is shifted to a slightly larger radius than the location of the trailing edge to avoid contact of the interface with the wall edges and faces of the TE itself. This is a common modification within turbomachinery simulations.

Uniform total pressure inlet and static pressure outlet with backflow prevention are set up. Reverse flow is allowed through the inlet, which helps with a stable settling of the initial conditions. The estimates of the outlet pressure are derived from the measurements - from station 4 which is the nearest to the CFD model outlet location. The "target mass flow rate" algorithm for the outlet is employed, so evenly distributed compressor map points can be simulated regardless of the accuracy of the initial outlet pressure estimate. This convenience also adds to the stability of the computation, but it slows down the convergence of the solution and it can cause the outlet pressure to get stuck in an endless loop of outlet pressure adjustments.

The pressure inlet does not specify the velocity magnitude, but the direction of the velocity vector is fixed. As the results from subsection 3.5.3 show a low variance of the deviation angle with respect to the flowrate, an average of the IGVs exit angle across the flowrate range is used as a fixed input for the specification of the inlet direction. The inlet is located at a radius higher than the IGVs LE, but since the channel has a constant width in the centripetal part and the local Mach number is low, the same angle is imposed on the inlet as computed earlier for the IGVs exit station. The reasoning is based on the general applicability of equation (3.11).

Identical mathematical models are applied as in the IGVs model (section 3.5). Steady compressible turbulent flow is simulated, modelled by the k-ω SST with `Fluent`'s hybrid wall function for the appropriately fine block-structured hexahedral mesh. For improved convergence and possible benefits in stability at the beginning of the simulation, the limits of the solved quantities are set relatively tight to their expected ranges. Considering the atmospheric inlet with total parameters of $293.15\,\mathrm{K}$, $10^5\,\mathrm{Pa}$, ranges of $\langle 190, 500\rangle$ K and $\langle 20000, 400000\rangle$ Pa are enforced.

3.6.3 Compressor model including IGVs

The preparation of this model is more difficult due to the `TurboGrid`'s incapability to process more than one blade row. The IGVs domain and the remaining compressor stage

domains are not joined until loaded into `Fluent`. This intrinsic property of `TurboGrid` is imposed by the lack of the implementation of the non-conformal mesh interfaces. The blade numbers of the consecutive blade rows are most often purposely coprime (their greatest common divisor = 1), therefore the only possible conformal interface would be a full circle. Although Bézout's identity guarantees that there is always a pair of integer cell numbers across both of the interblade channels to produce an identical number of cells around the circumference for both sides of the interface, other constraints still render this approach practically useless.

`TurboGrid` shapes the inlet, outlet and periodic BC surfaces arbitrarily as it optimizes the mesh orthogonality and smoothness. The inlet and outlet can only be constrained by radial and axial coordinate specifications, but the tangential coordinates are always unbound. The radial and axial location of the interface is manually synchronized between the IGVs domain and the compressor domain.

The mesh size is around 2.5×10^6 of the finite volume cells for the three compressor parts combined and around 0.4×10^6 per one IGV. The size, the topology and the cell size distribution are very similar to the model described in subsection 3.6.5. Therefore the right part of Figure 3.39 can illustrate the mesh of this model as well.

The mixing plane non-conformal generalized turbomachinery interface type would perfectly diffuse the IGVs wakes, so it is not used. The no-pitch scale interface definition seems to be the most physically accurate, but it showed some adverse behaviour in the testing: When the pitch of the connected domains is decreasing streamwise, it can generate a non-realistic swirling flow across the interface and adjacent periodic boundaries. This was experienced on a stator-to-rotor interface, but to confidently avoid this phenomenon, a countermeasure was also used for the concerned stator-to-stator interface.

With respect to the above mentioned experience with the testing of the `Turbo Workflow` recently introduced to `Fluent` (version 2022R2), it was decided to split the compressor domain into three parts, as pictured in the right part of Figure 3.37. Besides the necessary rotor and diffuser domains, an extra stator domain is extended through a part of the inlet channel. This distributes the functions of the non-conformal rotor-stator interface to the conformal interface between the rotor and the stationary inlet domain (itfc to MRF) and the fully stationary non-conformal interface between the IGVs and the compressor side of the inlet channel (no-pitch itfc).

The pitch *is* decreasing for 1 IGV to 1 rotor blade domain interface as the number of the IVGs is 20 and there are 14 rotor blades. (The greatest common divisor is actually 2 in this case.) When two interblade channels of the IGVs are used, the outlet of their domain can cover the whole inlet patch of the compressor inlet channel domain. These two patches can be connected by the no-pitch scale interface reliably. The penalty of the larger mesh size is small as the IGVs domain is now very short and the mesh can be relatively coarse at the higher radius where low velocities occur.

University of West Bohemia, Faculty of Mech. Engineering   Dissertation thesis 2022/23

Department of Power Systems Engineering   Ing. Lukáš Hurda
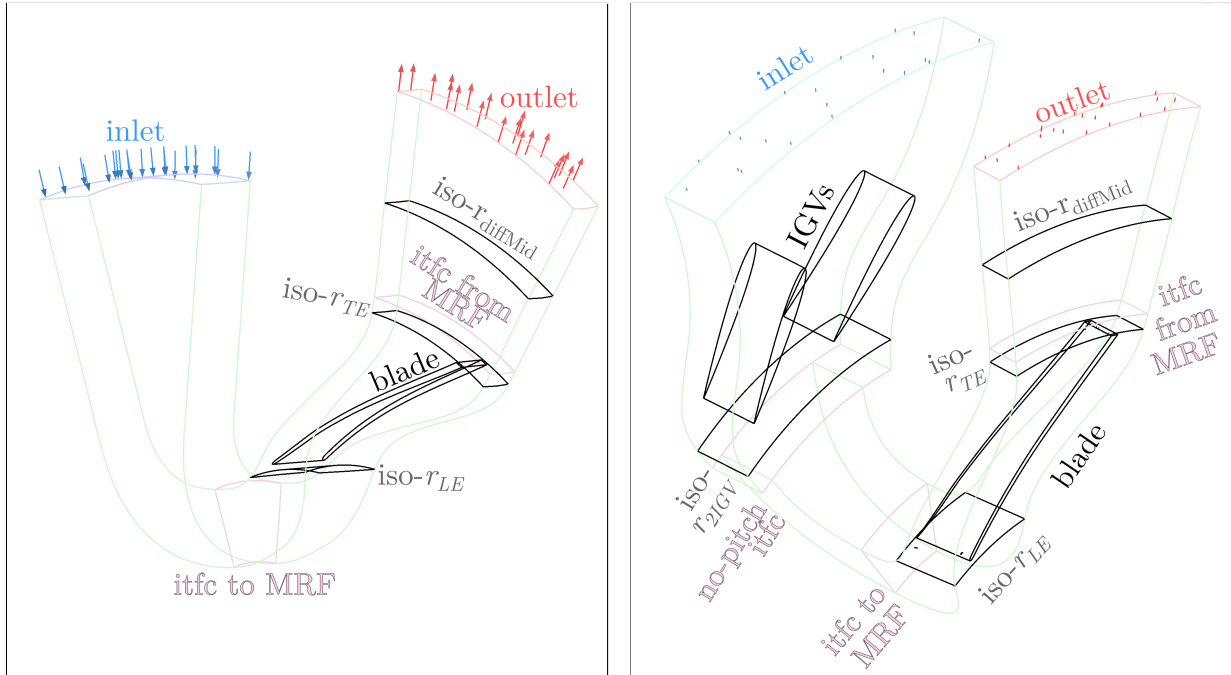
Figure 3.37: Boundary surfaces and post-processing surfaces in the s4 stage CFD model excluding (left) and including IGVs (right).

Unlike the simple editing of the inlet velocity direction prescription, it is necessary to build the whole `Fluent` case from scratch with different IGVs geometry and mesh for each of the concerned values of the IGVs stagger angle. Within `Fluent`, the domains are manually rotated around the machine axis to ensure a complete overlap of the compressor side of the non-conformal interface with the IGVs domain outlet patch.

The prevention of the pressure outlet backflow was switched off to enhance the stability of the simulations. This allowed more cases to converge to a solution. A fixed total temperature is prescribed for the flow entering the domain via the backflow portion of the outlet, so the efficiency evaluations may deteriorate. This is an acceptable drawback for this analysis.

3.6.4   New impeller design

The new impeller was designed with the intention to produce a compressor stage with very similar characteristics to the original stage, but with a rotor leading edge shifted upstream, far inside the aft part of the inlet channel bend.

To make this stage operate as desired, an inducer had to be designed i.e. the blading could not remain prismatic. A fully axial inlet is difficult to achieve in such low span-to-chord ratio blading. Instead, the leading edge is declined by approximately 60° down the channel bend, upstream from the original location near the end of the bend. According to

this inducer extension angle, the new stage is designated as "s4i60". The two impellers are compared in Figure 3.38.
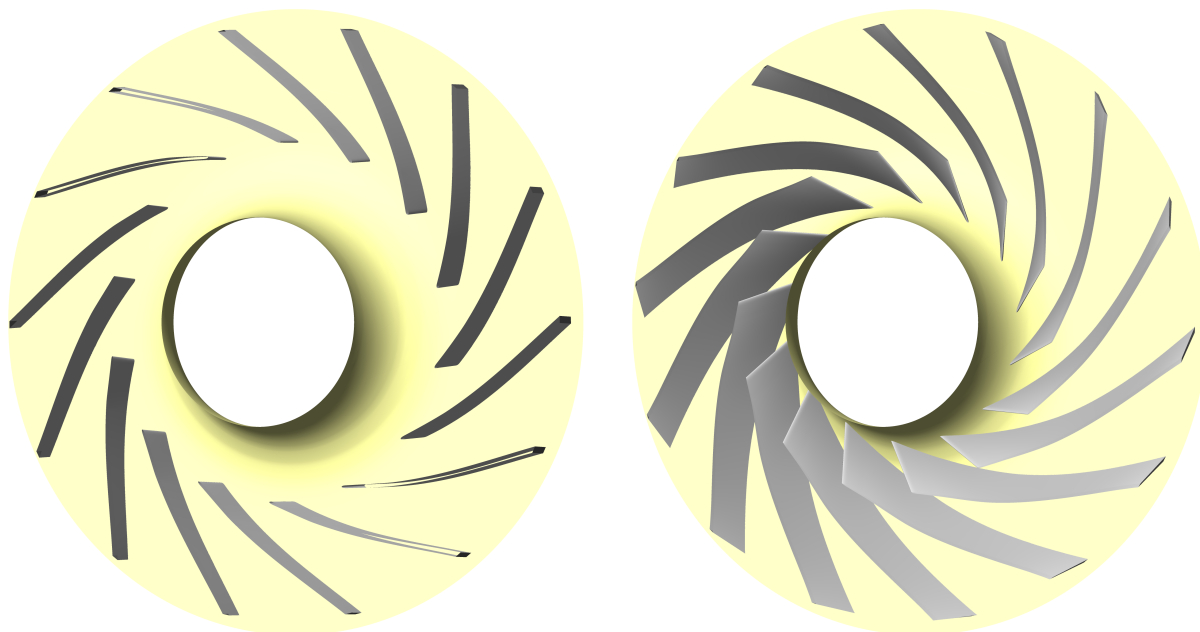
Figure 3.38: 3D view of hub and blading of the impeller of the s4 stage (left) and the s4i60 stage (right).

This approach to the impeller design aims to suppress the occurrence of the massive hub side boundary layer separation. The blading is extended upstream to the typical location of the ring vortex. It should dramatically alter the flow field conditions by physically splitting the fluid region with blades and introducing a strong source of momentum.

The original hub design surface description for `meangen` is kept intact as well as the blade count. The evolution of the meridional velocity is slightly adjusted in the region of the highest curvature of the shroud profile to avoid a sharp turn inside the blade row.

The flow coefficient and loading coefficient are rescaled to the lower radius of the hub tip of the LE:

- Flow coefficient at the LE hub tip -   s4: 0.4523;   s4i60: 0.7650.

- Loading coefficient at the LE hub tip -   s4: 1.8122;   s4i60: 4.0590.

The resulting shape of the blade can be intuitively described as "twisted". This perception comes from the 3D curvature of the blade and the fact that both the LE and TE are pitchwise-inclined. There is no purpose in the inclinations alone, it is just a result of the compromises made to position the hub and shroud blade profiles relative to each other ideally. Thanks to the free vortex flow design assumption, the shroud profile has a significantly lower camber than its hub side counterpart. Aligning either of the blade's

University of West Bohemia, Faculty of Mech. Engineering   Dissertation thesis 2022/23

Department of Power Systems Engineering   Ing. Lukáš Hurda

edges with an axi-radial plane would cause an excessive elongation of the other edge and a creation of a sharp corner between the blade and the impeller discs.

3.6.5   Full compressor model with the new impeller

The CFD model of the s4i60 stage is mostly analogous to the s4 stage model including the IGVs (subsection 3.6.3). It is not modelled and simulated without them. The only notable exception is that the number of modelled IGVs was further extended to three to cover the compressor side of the no-pitch scale interface. Because for this impeller, it has a warped shape and therefore it pitches across an extended angle. See the left part of Figure 3.39.
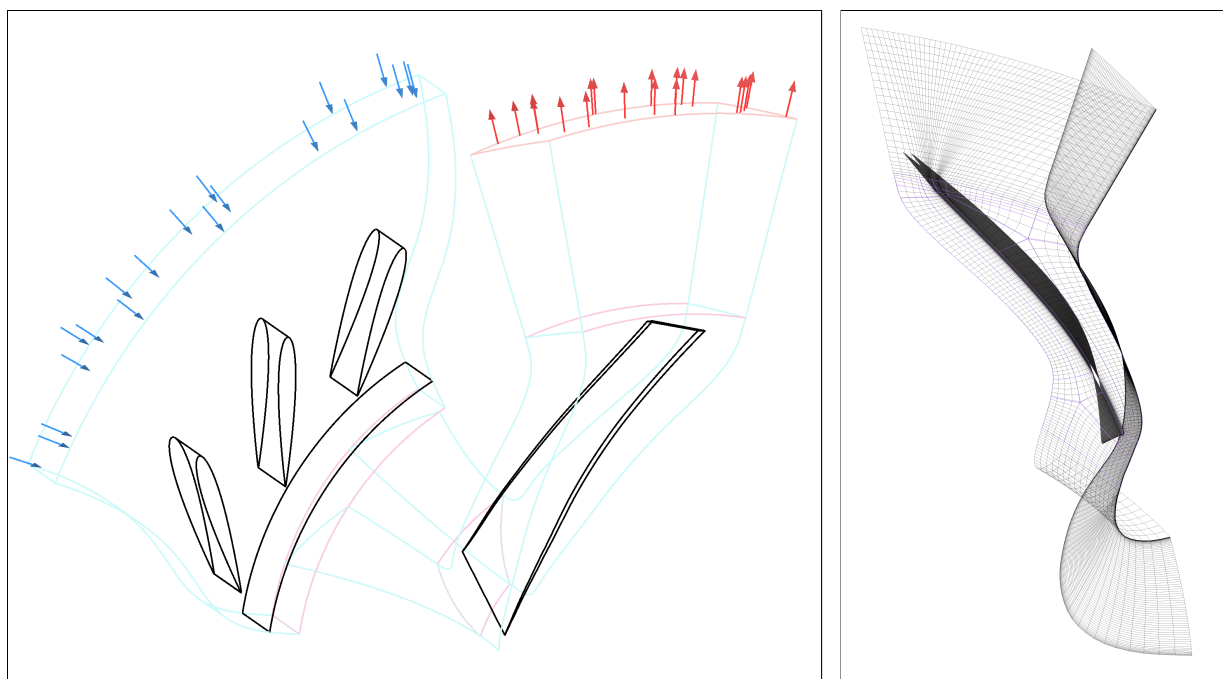
Figure 3.39: Boundary surfaces in the s4i60 stage CFD model (left) and compressor part coarsened mesh illustration (right).

3.6.6   Results of the full compressor CFD models

The results of all three full compressor CFD models are discussed in this subsection as they are meant to be directly compared. The integral characteristics are evaluated first. The speedlines are presented in the diagrams of the total pressure ratio versus the normalized mass flow rate, see Figure 3.40. The measurement data are included - these were already shown in Figure 3.7. The measurement was not carried out for $\vartheta = 30°$. The CFD cases which produce $\Pi < 1$ are still used to plot the speedlines, but the axes limits are trimmed to only show the useful range of values.

University of West Bohemia, Faculty of Mech. Engineering   Dissertation thesis 2022/23

Department of Power Systems Engineering   Ing. Lukáš Hurda
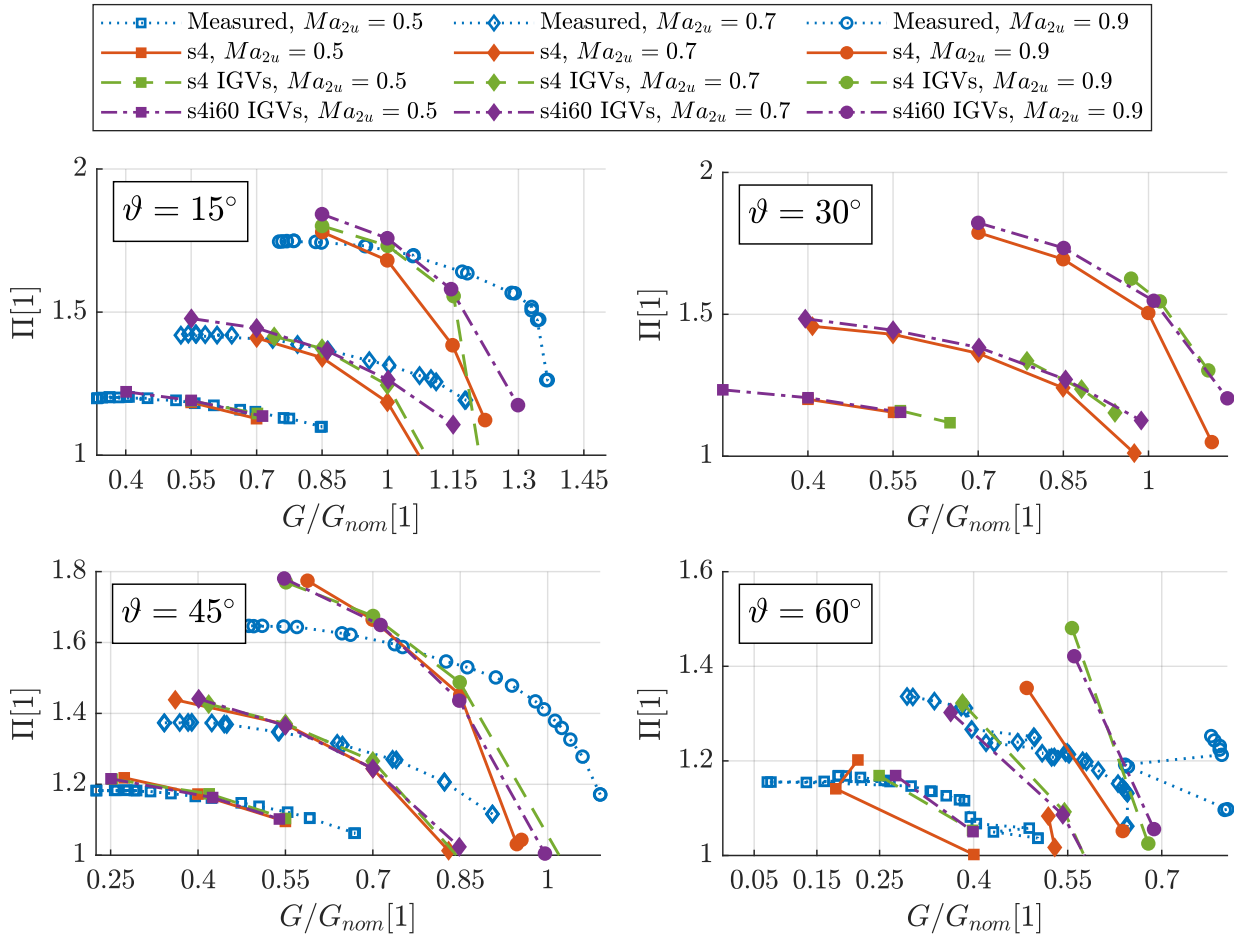
Figure 3.40: Compressor maps simulated in the full compressor CFD models and corresponding measurement data.

For further reference, the individual cases of the operating points are code-named as:

`"s4 ∩ s4IGVs ∩ s4i60IGVs / ϑ in [°] / target G/Gnom / Ma2u".`

The occasional **reverse flow through the outlet** is not treated in any special way. This may present a caveat in the setup. A revision of the solver reports of the mass flow rate through the outlet versus through the rotor exit station reveals that the discrepancies are tolerable. Most of the cases show around 0.1 % mass flow deviation. A limited number of the cases, including the ones discarded from further post-processing, show deviations < 5 %. The fluid which enters through the outlet leaves through the outlet after a short distance traveled. Therefore the influence on the total flow rate is cancelled out as long as the solver assigns positive and negative flowrate values to the respective directions through the mesh faces of the outlet.

There is a significant offset of the **speedlines measured** in the real stage and the characteristics produced by the CFD computations. Of course, this is an effect of all

University of West Bohemia, Faculty of Mech. Engineering   Dissertation thesis 2022/23

Department of Power Systems Engineering   Ing. Lukáš Hurda

the uncertainty involved in the stage re-design process, at least for the most part. The higher camber and overall length of the s4 stage impeller substitute may allow better flow guidance and slightly higher flow blockage. This is in agreement with the speedlines, which are steeper, and reach higher discharge pressure at low flowrates, but experience the choking condition sooner - at lower flowrates.

Criteria are set for the computational cases to determine the sufficiency of their **level of convergence**. The values of the pressure ratio and the mass flow rate are reported from every iteration of the steady state calculation procedure which was set to run for at least 5000 iterations. These values are gathered from the last 500 iterations of the solver and if the absolute range of the mass flow rate is $> 10\,\%$ of the nominal flowrate or if the pressure ratio oscillates by $> 20\,\%$ of its mean value, the case is excluded from the graph. The negative mass flow rate results are discarded as well.

Very few of the cases are filtered out, but the most interesting set involves the cases of `s4IGVs` **at 30° stagger and low normalized target mass flow rates** (TMF). The speedlines of this model variant are significantly reduced from the left compared to the remaining models. Even the converged points experience a massive mass flow increment from the target value - for example, the lowest blade Mach number cases for TMF of 0.4 and 0.55 both have an actual normalized flowrate value above 0.55.

For a deeper insight, **axial velocity contour plots** are produced to view the flow field on the periodic boundary surface in the channel bend. The value range clipped at the minimum of $0\,\mathrm{m\,s^{-1}}$ allows to show the recirculation regions expected at the hub wall. All of the contour plots from the cases that deserve commentary are gathered in appendix B. Note that the axial velocity ceases to carry valuable information when the flow direction is close to radial. The maximum of the clipped range of $150\,\mathrm{m\,s^{-1}}$ is arbitrary, the red-bound empty regions do not have a special meaning. The impeller is always on the right side of the pictured channel.

`Fluent` treats the periodic boundary as one surface containing both sides of the boundary. Due to the complex geometry of the domains, finding a simple iso-clip operation using some of the coordinates is not trivial. Therefore an attempt to view just one side of the boundary is made via the camera positioning. Some pictures may contain graphical artefacts from the other side of the boundary. With enough care, they can be safely identified by the viewer.

A comparison of the contour plots with the results of the simplified channel model shown in subsection 3.4.3 reveals that the more complex channel shape is more stable and that even the original s4 impeller has a favourable influence on the flow field in the inlet channel bend. According to the expectations, the impeller does not allow the development of a large shroud side recirculation zone.

Unfortunately, the contour plots mentioned above do not provide any interesting information about the instability of the `s4IGVs/30/...` cases. There is no notable difference between the plots of the last stable operating points of the unstable speedlines and their

counterparts built upon the `s4` model. The model without the IGVs neither features any interesting flow structure in the cases analogous to the unstable ones from the model incorporating IGVs. These contour plots are not worth involving in the mentioned appendix.

Another phenomenon is yet clearly observable in the axial velocity contour plots (appendix B): The **hub side flow separation** in the $\vartheta = 45°$ operational points. Only the `s4IGVs` model allows the hub side separation, which yields two separate conclusions:

1. The design modification of the s4i60 stage impeller effectively suppresses the separation or at least it does not allow it to develop into a larger spanwise dimension and cause a major flow blockage or a directional deflection.

2. The presence of the IGVs and the wake they generate is able to destabilize the boundary layer because, in some of the otherwise identical cases with the swirl induced by the inlet BC, the separation does not occur in contrast to the case with the IGVs.

Ad 1.: At 45° stagger, the range of the speedlines of the `s4IGVs` model is not reduced despite the facts mentioned above. The recirculation zones shown in Figure B.1 are not extremely large, but they may predict a possible unsteady behaviour in the real machine. Here, the most important finding is the rapid induction of the reattachment of the separated boundary layer in the `s4i60IGVs` cases. It is exactly the intention of the particular s4i60 stage design.
At a higher stagger - 60° - the speedlines are too short for a sensible assessment of the situation. (Typically only 2 valuable operating points are computed.) The differences notable amongst the prismatic impeller and the 3D impeller in the axial velocity are immense, see Figure B.2:
At TMF of 0.25, the massive separation shown in `s4IGVs` does not take place in the `s4i60Igvs` at all. At higher flow rates and rotational speeds, the separation affects both compared models, but in the `s4i60Igvs`, the recirculation zone is disturbed by the rotor LE and a certain degree of a favourable velocity profile re-distribution takes place.

Ad 2.: As mentioned, there is no disturbance in the 30° cases without the IGVs for which the simulations diverged in the model with the IGVs. For 45° however, pairs of detached and attached boundary layers in the analogous cases with and without IGVs are shown in Figure B.3. At 60° and the extremely low TMF = 0.25, a large recirculation zone takes place in the `s4` model too, but the flow blockage is still lower than in the `s4IGVs` by a small margin.

3.6.7 Conclusions from the full compressor models

The full compressor models logically follow the previous analyses. It allows us to put the generalized conclusions into the context of a real-world machine and compare the results with the measurement.

The redesign of the original impeller uses an identical shape of the hub and shroud walls and most of the impeller characteristics are equal to the original s4 impeller. The higher wrapping angle of the blading causes a slight difference in the compressor maps derived from the measurement and the CFD simulations with the substitute impeller. However, the compressor operating range is matched sufficiently - especially the mass flow rate range is practically identical with respect to the chosen resolution of the speedlines. Of course, completely concordant results of measurement and simulation can not be expected even if the stage geometry was perfectly matched.

The introduced design of the new s4i60 stage with an upstream-shifted rotor blade leading edge complies with the requirement of a very similar operational characteristic to the s4 stage.

A full operating range of the test bed compressor was subject to modelling. The steady state simulations were conducted including a single interblade channel of the 14 total. A BCs combination of pressure inlet and outlet and a thoughtful configuration of the mesh domain interfaces was used. Such models proved to be sufficiently detailed to capture the flow features observed in the earlier simplified geometry simulations. The target mass flow rate algorithm for the pressure outlet BC helped to produce simulation results which are easily compared across the different models.

Both of the hypotheses which have motivated the computations discussed above were confirmed:
The IGVs wake has a non-negligible influence on the stability of the hub side boundary layer. To model the phenomenon accurately in the future, IGVs should always be physically included in the computational domain.
The new design of the s4i60 stage has proved to be less prone to the impeller inlet flow blockage. The inducer actively supports the reattachment of the boundary layer at the hub wall.

The accuracy of the model could be improved by adding the outlet channel bend behind the diffuser and possibly also the de-swirl blades (sections between stations 4-5 and 5-6 or 7 as shown in Figure 2.2) into the model. The outlet BC at the current position allows the reverse flow which is not ideal for the compressor duty assessment and it can influence the flow in the diffuser. However, it has no effect on the flow in the inlet channel and the impeller. The target mass flow rate function for the outlet proved to be an effective tool to produce evenly distributed operational points. At the less stable points, this less important requirement of even TMF intervals is not met, but the simulations still result in useful convergent solutions.

University of West Bohemia, Faculty of Mech. Engineering   Dissertation thesis 2022/23

Department of Power Systems Engineering   Ing. Lukáš Hurda

4   Conclusions

The problem of the unstable operation of the centrifugal compressor is introduced in chapter 1. The availability of extensive measurement data opens the door to a thorough analysis of the specific test bed compressor. Generalizations were made for the wide applicability of the results.

Chapter 2 presents a summary of the widely used standard methods for dimensional analysis and CFD, the fundamental theory of centrifugal compressors as well as the more specific methods of measurement data evaluation which has been developed by the author.

The initial modelling of the problem by means of the dimensional analysis (section 3.1) provided a stable foundation for further progress. The need to separate the inlet channel flow from the compressor duty is emphasized. The basic set of parameters of the key phenomena is defined.

The important relation of the inlet channel flow to the compressor stage duty is discussed within section 3.2. A simple but crucial evaluation of the IGVs exit metal angle is provided. The station-to-station 0D calculations allow the linking of the values of the local flow parameters to the integral characteristics of the compressor. The methodical approach allows clarification of the magnitude of the possible influences of the progressively increasing IGVs deviation angle, the compressibility effects and the total pressure loss. Results reveal an interesting, non-trivial relation between the rotor LE incidence angle and the relative flow Mach number to the flow coefficient at various swirl angles. It might explain the intermittent nature of the measured compressor map defects.

The measurement data evaluation in the first subsection of section 3.3 concludes that the operational defects are not defined by the compressor duty parameters. The second subsection is dedicated to the evaluation of the flow criteria in the two stages used for computational analyses. It also links the parameters of the inlet flow to the operational defects.

A methodical, generalized, dimensional-analysis-based set of simulations is presented in section 3.4. The inlet channel flow without the presence of the impeller is modelled. The results of the parametric studies show a comprehensive overview of the influence of the individual parameters on the flow field in the inlet channel. The hub side boundary layer separation in the channel bend is given the most attention. The inlet flow swirl angle is proved to be the most important parameter determining the flow separation. While the geometry parameters and Reynolds number have a significant influence, they do not allow for avoiding the hub side separation at a high enough swirl angle. The results of the simplified compressor channel geometries related to the real s2 and s4 stages also suggest

University of West Bohemia, Faculty of Mech. Engineering   Dissertation thesis 2022/23

Department of Power Systems Engineering   Ing. Lukáš Hurda

that the impeller has a favourable influence on the flow field. This is later confirmed by the full compressor CFD models. Moreover, the equivalent of the s2 stage which was not problematic in the measurements also shows strong disturbances in the inlet channel flow field.

The CFD analyses of the real compressor geometries start with the determination of the IGVs simulations. The results of this model determine the deviation angles for the setup of the compressor model without the IGVs. The suspicion about an appropriate selection of the vane profile used in the real machine was declined by the results of the simulations conducted with vanes of a thinner profile. These performed worse at high stagger angles in terms of the pressure loss and the deviation angle. This model is also used for a limited assessment of the real channel shape behaviour in comparison to the simplified bladeless channel model.

The full compressor models as the key final part provide the verification of the earlier simplified models and they analyze the interaction of the inlet channel flow with the impeller. The results are compared to the measurement data. The agreement is good with respect to the accuracy of the impeller redesign.

The IGVs wakes proved to play a role in the destabilization of the channel bend flow. The new impeller design is verified to suppress the hub side boundary layer separation.

4.1   Compressor design recommendations

Several approaches can be used to make the stage less susceptible to inlet flow blockage. Two of them can be described based on the previously obtained results: The inlet channel shape modifications and the impeller blading adjustments.

4.1.1   Inlet channel shape modifications

A common turbomachinery design procedure starts with the creation of a design surface (a profile curve in the axi-radial plane) and the shaping of the channel based on the meridional flow velocity evolution along this curve. 1D mean flow calculations are used to determine the sequence of the states of the working fluid along the design surface. There are very few reasons not to keep the meridional velocity constant away from the sections involved in the primary energy transfer like the compressor rotor and the diffuser.

In the case of the inlet channel flow, the meridional velocity distribution can be altered to control the streamwise pressure gradient. If the meridional velocity keeps increasing throughout the channel bend, the effect of the flow separation due to the centrifugal forces can be delayed. In the front part of the channel, an increasing velocity can be achieved even with the increasing channel width, as long as the decrease of the mean radius has

University of West Bohemia, Faculty of Mech. Engineering   Dissertation thesis 2022/23

Department of Power Systems Engineering   Ing. Lukáš Hurda

a stronger effect on the flow area change. In the aft part, the radius is increasing and therefore the width needs to increase rapidly to keep a steady velocity increase.

However, a narrow entry to the impeller would reduce the operating range of the machine due to the increase in the inlet relative flow Mach number. Making the centripetal part of the channel extremely wide would decrease the Reynolds number of the flow through the IGVs. It can theoretically lead to a more intense suction side separation on the IGVs surface or even an unstable flow in the IGVs. In light of the results from subsection 3.5.3, the margin to the IGVs cascade stall could be relatively large, so a high centripetal channel width can be a useful starting point for the modifications.

Another feature of the swirling flow generated by the radial IGVs is the high tangential velocity near the hub wall. It is a result of the axial bend centrifugal force. A careful control of the hub curvature may help alleviate the tangential velocity profile skewness. Such a task is not trivial - an iterative process with the aid of a simple CFD model is inevitable. Lowering the axial curvature in the front part of the bend might be a good starting point for the optimization. A significantly higher curvature can be introduced in the aft part of the bend to use the increase of the axial bending centrifugal force to suppress the hub side separation caused by the tangential bending centrifugal force.

The results of paragraph 3.4.2.5 suggest enlarging the bend apex radius. For the impellers with a constant radius LE, it should be possible to some extent.

A summary of the suggestions for the channel shape design: Make the centripetal channel very wide (but check the stable operation of the IGVs) and gradually narrow it throughout the bend to produce a constantly increasing mean meridional flow velocity. Keep the axial curvature low in the front part and make the bend sharper in the aft part. The channel width decrease should also be concentrated in the aft part. If possible, bring the bend apex to a higher radius.

Although these modifications were derived from the thorough analyses of the 2D and 3D simulated flow fields, most of them can be observed when comparing the simplified bladeless channel model of the s4 stage with the IGVs model based on the real compressor geometry. The IGVs model performed better at the same conditions defined by Re, Ma, and the flow swirl angle.

4.1.2   Impeller blading modifications

The impeller modifications have already been applied successfully within the CFD models. The design process is described in subsection 3.6.4. Results of the flow simulations are summarized in subsection 3.6.6.

The recommendation is to leave the prismatic blading with the constant radius LE and move the LE far upstream inside the channel bend, where the hub side recirculation zone

might be located. The impeller blading should disallow the existence of this flow feature, like the s4i60 impeller.

It is possible to design such an impeller with a characteristic very similar to an existing 2D bladed one. The feasibility of such a design with a more complex geometry can be questionable in some cases. The aerodynamic design was conducted, but the real impeller must also meet the requirements of the structural strength including rotor dynamics and the production technology. A narrow channel, shrouded impeller with 3D blading is likely to be impossible to manufacture with reasonable costs.

4.2   Future work

Some parts of this work would deserve a refined methodology or some further extensions. Firstly, a matter that has not been discussed yet is brought up: The axial IGVs do not cause similar problems to the radial IGVs. They also introduce swirl to the flow and the swirl also passes through the channel bend part earlier described as the aft part. It may not be clear why they are not problematic as well. It can be the fact that due to the strongly constrained geometry, they provide less flow guidance at the hub side, where vane profiles with a shorter chord need to be used. This yields a tangential velocity profile similar to the rotating rigid body circumferential speed - tangential velocity is low at the hub. Also, the proximity of the vanes to the impeller may provide a more stable behaviour on its own. A certain amount of effort is worth investing in the verification of this hypothesis.

The measurement apparatus is complete and fully functional, so in terms of the main goal of this analysis, there is no need to invest additional effort into it. It is however *ready* to be exploited and broadened to a much wider sort of applications in measurements of compressible fluid flows. The most promising application is the multistage machines' production tests. It would require heat exchanger evaluations for the intercoolers and side loads and bleeds implementation. The only present weakness of the evaluation algorithm is the polytropic compression evaluation, which is on the level of the industry standard, but it is not sufficiently accurate for the far-off design conditions.

An additional effort can be usefully spent on a more solid linkage of the dimensional analysis and measurement results to the simulation results of the full compressor models. Evaluation of the mean Reynolds and Mach numbers in the important stations and an analysis of the irregularity of the CFD flow field would help to link the measured instability regions to the simulated operating point precisely. A precise geometry model of the measured stages would be required as a starting point for this matter.

The full compressor models are really simple and small in terms of the present CFD capabilities. There is a relatively large margin for the feasibility of more complex simulations, which could possibly produce more accurate results. More interblade channels or even a full impeller could be included in the computational domain as well as longer inlet and discharge channels (including the de-swirl vanes), secondary flow paths through

the rotor seals and the dead volume of the associated cavities could be incorporated as well. Transient simulations and more progressive turbulence models would also increase the fidelity of the computational models.

A modest first iteration of the refinements would be a transient simulation of the full compressor with the inlet at an unchanged position and the outlet at station 6 or 7. The domain might include 2-4 blades of the rotor and a corresponding number of IGVs. Further analysis should leave the whole range of parametric studies of the machine operating range. It should focus on the cases where the hub side recirculation zone is present or even the cases whose solution diverged in the single blade models. More degrees of freedom given to the flow by less-constraining domain periodicity and the transient description can produce results closer to reality, even at less favourable unstable conditions.

With the computational power provided by the graphics processing units and the emerging `Fluent` solver written for these graphical chips, it would not be a great problem to simulate a full circle compressor model. As the meshes are already relatively fine for the wall-resolved k-ω SST turbulence model, scale-resolving turbulence models could be employed and the meshes should still have a manageable size, probably $< 10^8$.

Such simulations should be used to verify the simpler model results and possibly reveal new findings within the extended range of regimes close to the defects shown in the compressor maps.

On the other hand, it is possible that the instability has a similar nature to the compressor surge, which is still very challenging to model in CFD. It requires a large inlet and outlet plenum to be included in the domain and it is a transient effect with a drastically lower frequency compared to the frequency of the impeller rotation. This leads to a need for tremendous amounts of fine timesteps for the solution of the problem.

There is probably no practical benefit in getting a thorough description of the unstable regime itself. For the operation of the machines, it is only important to avoid or reliably predict the instabilities.

4.3   Contributions to the field

The measurement evaluation program, although built upon very simple theoretical foundations, is a useful, practical tool. It is widely applicable and easily extensible to virtually any measurement of the compressible fluid flow by temperature and pressure probes. It combines the real gas EoS implementation with the well-thought-out spatial averaging of the multi-probe station data, the polytropic compression evaluation, and the corrections of the compressor operating conditions. Many compromises and simplifying assumptions commonly used in engineering calculations were ditched and a more methodical approach was developed instead.

According to the author's research, there is very little published knowledge about the operation of centrifugal compressors with radial IGVs. Some manufacturers resort to using axial IGVs despite the undeniable benefits of the former mentioned.

The analysis of the off-design conditions of such compressors is an original and innovative work. This is also the reason why efforts were spent on the generalization of the results.

From an academic point of view, the topologically simple arrangement of the specific toroidal channel is an interesting example of a flow governed by centrifugal forces. This flow is subjected to dimensional analysis and further analyzed by numerical methods at various operating conditions.

An interesting counter-intuitive relation of the rotor LE incidence angle and the relative flow Mach number to the flow coefficient at various swirl angles is revealed. It might explain the intermittent nature of the measured compressor map defects.

The operation of a radial IGVs cascade is described and an application of a modified blade profile is tested. The superiority of the thick symmetrical airfoil profiles for the specific purpose is concluded.

The source of the instabilities of the compressor operation was identified, and the interactions of the clearly separate flow and geometry features were analysed. The prismatic blading of the impeller was identified as the main weakness of the compressor design. Suggestions for a better design confirmed by the testing of the modifications were compiled.

The necessity to involve the IGVs in the simulations of the compressor was confirmed. The interaction of the IGVs wake with the hub side boundary layer cannot be omitted if the inlet channel flow stability is about to be assessed.

4.4   Final conclusion

All of the objectives set in section 1.4 were met.

The inlet channel flow hub side separation was confirmed to be the root cause of the compressor operation instabilities. The exact mechanism of the impeller's incapability to conform to the expected operational map due to the disturbed state at the blade leading edge is not known. It is clear, however, that the hub side recirculation zone is effectively blocking the flow into the impeller and it deteriorates the incidence angle, at least on a portion of the span.

The unstable regime itself is very challenging to describe by any fluid mechanics method. Indirect evidence is used to support the hypothesis: The computational cases which failed to converge are located on the speedlines where other surrounding simulated operating points feature the hub side separation.

University of West Bohemia, Faculty of Mech. Engineering   Dissertation thesis 2022/23

Department of Power Systems Engineering   Ing. Lukáš Hurda

The generalization of the results is achieved by dimensional analysis, mean flow 0D calculations, and computational parametric studies. The CFD is used to go through a whole range of the operating conditions of the test bed compressor and also some convenient selection of the set of parameters for a generalized study.

The measurement evaluation program including the real gas EoS is written and used to analyze a vast database of the measurement data. It is also extended to allow the expression of the estimations of the flow criteria in the non-standard measurement stations.

Full compressor models are built and used for numerical analysis of the flow. The general conclusions of the earlier parametric studies are confirmed. A more comprehensive post-processing of the full compressor simulation results would be needed to link the analyzed operational points to the measurement points and parametric study cases exactly. Either way, the geometry discrepancies between the real compressor used in the measurements, the computational model for the full compressor simulations and the simplified geometries of the parametric studies do not allow a direct comparison.

A major modification of the original impeller is designed and later modelled in CFD with great success. The new impeller is less prone to allow the existence and growth of the hub side recirculation. Modifications to the channel shape are also suggested based on parametric studies and other computational models, but the verification of the effectiveness of these modifications is beyond the scope of this thesis.

References

[1] Jaroslav Levý. "Analýza jevů ovlivňujících měření teplot a dalších veličin na zkušebním radiálním kompresoru". [Analysis of the phenomena affecting the measurement of temperatures and other values on the test centrifugal compressor]. Master thesis. Pilsen: University of West Bohemia, Faculty of Mechanical Engineering, 2018. [Original language: Czech].

[2] Lukáš Hurda and Richard Matas. "Uncertainty analysis of thermal quantities measurement in a centrifugal compressor". In: *AIP Conference Proceedings* 1889.1 (2017). ISSN: 0094-243X. DOI: 10.1063/1.5004346. URL: https://pubs.aip.org/aip/acp/article/792342 (visited on 08/02/2023).

[3] Tomáš Syka. "Vliv geometrických úprav na účinnost kompresorového stupně". [Geometrical modifications influence on the compressor stage efficiency]. Dissertaion thesis. Pilsen: University of West Bohemia, Faculty of Mechanical Engineering, 2015. [Original language: Czech].

[4] Zuzana Linhartová. "Numerické simulace proudění v ucpávce kompresoru". [Numerical simulations of flow in a compressor seal]. Master thesis. Prague: Czech Technical University in Prague, 2019. [Original language: Czech].

[5] F.M. White. *Fluid Mechanics*. 7th ed. McGraw-Hill series in mechanical engineering. McGraw Hill, 2011. ISBN: 978-0-07-352934-9. URL: https://books.google.cz/books?id=egk8SQAACAAJ.

[6] S. Larry Dixon and Cesare. A. Hall. *Fluid mechanics and thermodynamics of turbomachinery*. Seventh edition. Boston: Elsevier, 2014. ISBN: 978-0-12-415954-9.

[7] Seppo A. Korpela. *Principles of turbomachinery*. 1st ed. Hoboken (New Jersey): Wiley, 2011. ISBN: 978-0-470-53672-8.

[8] Shuichi Yamashita. "Multistage Centrifugal Compressor". Pat. US 10077778 B2. Mitsubishi Heavy Industries Compressor Corp. 2018. URL: https://patents.google.com/patent/US10077778B2/en (visited on 08/02/2023).

[9] Howden ČKD. "Internal documentaion".

[10] Lukáš Hurda and Richard Matas. "Radial compressor test data processing with real gas equation of state". In: *AIP Conference Proceedings* 2189.1 (2019). ISSN: 0094-243X. DOI: 10.1063/1.5138621. URL: https://pubs.aip.org/aip/acp/article/791606 (visited on 08/02/2023).

[11] *Multall: An Open Source, CFD Based, Turbomachinery Design System*. Vol. 2B: Turbomachinery. Turbo Expo: Power for Land, Sea, and Air. June 2017, V02BT41A027. DOI: 10.1115/GT2017-63993. URL: https://doi.org/10.1115/GT2017-63993.

University of West Bohemia, Faculty of Mech. Engineering   Dissertation thesis 2022/23

Department of Power Systems Engineering   Ing. Lukáš Hurda

[12]   John D. Denton. *multall-turbomachinery-design*. URL: `https://sites.google.com/view/multall-turbomachinery-design` (visited on 08/02/2023).

[13]   Andreas Weiß. "Private communication and Turbomachinery Design Workshop at University of West Bohemia, May 2023".

[14]   J. Oldřich, J. Novák, and A. Malijevský. "Adiabatický děj v technické praxi, [Adiabatic process in technical practice]". In: *Strojírenství* 40.2 (1990), pp. 69–76. [Original language: Czech].

[15]   *ISO 5167-2. Measurement of fluid flow by means of pressure differential devices inserted in circular cross-section conduits running full - Part 2: Orifice plate.* Second edition. International Organization for Standardization (ISO). Switzerland, 2022.

[16]   Václav Štěpina and Václav Veselý. *Lubricants and special fluids.* Amsterdam: Elsevier, 1992. ISBN: 04-449-8674-X.

[17]   L. M. Henderson, S. W. Ferris, and J. M. McIlvain. "Specific heats of mineral oils. Determined by a new method". In: *Industrial & Engineering Chemistry Analytical Edition* 1.3 (1929), pp. 148–151. ISSN: 0096-4484. DOI: `10.1021/ac50067a017`. URL: `https://pubs.acs.org/doi/abs/10.1021/ac50067a017`.

[18]   C. Antoine. "Tensions des vapeurs; nouvelle relation entre les tensions et les températures". [Vapor Pressure; a new relationship between pressure and temperature]. In: *Comptes Rendus des Séances de l'Académie des Sciences* 107 (1888), pp. 681–684, 778–780, 836–837. [Original language: French].

[19]   *PTC 10. Performance Test Code on Compressors and Exhausters.* 1997(R2014). American Society of Mechanical Engineers (ASME). 1997. ISBN: 978-0-7918-2450-4.

[20]   C. W. Tan. "Real Gas Vs. Ideal Gas". In: *CompressorTech2* 2016.August-September (2016), pp. 88–92. ISSN: 1085-2468.

[21]   M. Mallen and G. Saville. "Polytropic processes in the performance prediction of centrifugal compressors". In: *Proceedings of Institution of Mechanical Engineers* C183/77 (1977), pp. 89–96.

[22]   John M. Schultz. "The Polytropic Analysis of Centrifugal Compressors". In: *Journal of Engineering for Power* 84.1 (1962), pp. 69–82. ISSN: 0022-0825. DOI: `10.1115/1.3673381`. URL: `https://asmedigitalcollection.asme.org/gasturbinespower/article/84/1/69/405330/The-Polytropic-Analysis-of-Centrifugal-Compressors`.

[23]   Joel H. Ferziger and Milovan Perić. *Computational Methods for Fluid Dynamics.* Third edition. Berlin: Springer, 2012. ISBN: 978-3-642-56026-2.

[24]   Jaromír Příhoda and Petr Louda. *Matematické modelování turbulentního proudění.* [Mathematical modelling of turbulent flow]. Vyd. 1. Prague: Vydavatelství ČVUT, 2007. ISBN: 978-80-01-03623-5. [Original language: Czech].

[25] Tuncer Cebeci and A. M. O. Smith. *Analysis of Turbulent Boundary Layers.* 1st Edition. Berlin: Elsevier, 1974. ISBN: 978-0-121-64550-2.

[26] Florian Menter, M. Kuntz, and R. Langtry. "Ten years of industrial experience with the SST turbulence model". In: *Proceedings of the Fourth International Symposium on Turbulence, Heat and Mass Transfer, Antalya, Turkey, 12-17 October, 2003.* Ed. by K. Hanjalić, Y. Nagano, and M.J. Tummers. Vol. 4. Turbulence Heat and Mass Transfer Series. Begell House, 2003. ISBN: 978-1-567001-96-9. URL: `https://books.google.com/books?id=kmjdqi4-OHcC` (visited on 08/02/2023).

[27] Hermann Schlichting and Klaus Gersten. *Boundary-Layer Theory.* 9th ed. Berlin: Springer, 2016. ISBN: 978-3-662-52917-1. DOI: `10.1007/978-3-662-52919-5`.

[28] Christopher Greenshields. *OpenFOAM v7 User Guide.* London, UK: The OpenFOAM Foundation, 2019. URL: `https://doc.cfd.direct/openfoam/user-guide-v7` (visited on 08/02/2023).

[29] Ansys, Inc. *Ansys Fluent User's Guide.* Release 2022 R2. Canonsburg, July 2022.

[30] Ansys, Inc. *Ansys Fluent Theory Guide.* Release 2022 R2. Canonsburg, July 2022.

[31] S. M. Gorlin and I. I. Slezinger. *Wind Tunnels and Their Instrumentation.* (Aeromekhanicheskie izmerenia. Metody i pribory). Trans. by P. Boltiansky. 346. Jerusalem: Israel Program for Scientific Translations, 1966. URL: `https://play.google.com/store/books/details?id=JksjAAAAMAAJ` (visited on 08/02/2023).

University of West Bohemia, Faculty of Mech. Engineering   Dissertation thesis 2022/23

Department of Power Systems Engineering   Ing. Lukáš Hurda

Author's publications and activities

.

Relevant to the thesis topic

The author is a part of the team of researchers carrying out the measurements and CFD simulations within the cooperative project of UWB NTC with Howden ČKD.

He completed an internship at Siemens Energy AG, Mülheim an der Ruhr, Germany (July to September 2021).

HURDA, L., MATAS, R.. Uncertainty Analysis of Thermal Quantities Measurement in a Centrifugal Compressor. In AIP Conference Proceedings 1889. Melville, NY, USA: American Institute of Physics, 2017. s.1-8. ISBN 978-0-7354-1572-0 , ISSN 0094-243X. doi:10.1063/1.5004346.
*Presented by L. Hurda at a joint conference on **Power System Engineering** and **Setkání kateder mechaniky tekutin a termomechaniky (Meeting of Faculty Departments of Fluid Mechanics and Thermomechanics) 2017**, Pilsen, Czech Republic.*

MATAS, R., SYKA, T., HURDA, L. Experimental investigation and numerical modelling of 3D radial compressor stage and influence of the technological holes on the working characteristics. In EPJ Web Conf. 180: EFM17 – Experimental Fluid Mechanics 2017. Les Ulis Cedex A: EDP Sciences, 2018. ISSN: 2101-6275. doi:10.1051/epjconf/201818002060.
*Presented by L. Hurda in a poster section of the conference on **Experimental Fluid Mechanics 2017**, Mikulov, Czech Republic*

LEVÝ J., MATAS, R., HURDA, L. Analysis of phenomena affecting thermal measurements on a test radial compressor. In AIP Conference Proceedings 2047, 020012. Melville, NY, USA: American Institute of Physics, 2018. doi:10.1063/1.5081645.
*Presented by L. Hurda at a conference on **Power System Engineering 2018**, Pilsen, Czech Republic.*

HURDA, L.., MATAS, R. Radial Compressor Test Data Processing with Real Gas Equation of State. In AIP Conference Proceedings 2189. Melville, NY, USA: American Institute of Physics Inc., 2019. ISBN 978-0-7354-1936-0 , ISSN 0094-243X. doi:10.1063/1.5138621.

University of West Bohemia, Faculty of Mech. Engineering   Dissertation thesis 2022/23

Department of Power Systems Engineering   Ing. Lukáš Hurda

*Presented by L. Hurda at a conference on **Power System Engineering 2019**, Pilsen, Czech Republic.*

MATAS, R., SYKA, T., HURDA, L., LINHARTOVÁ, Z. Numerical Modelling and Experimental Investigation of the Influence of Selected Geometric Elements on the Working Characteristics of Radial Compressor Stages with Prismatic Blades. In EPJ Web Conf. 269: EFM19 – Experimental Fluid Mechanics 2019. Les Ulis Cedex A: EDP Sciences, 2022, doi:10.1051/epjconf/202226901036.

*Presented by L. Hurda and R. Matas in a poster section of a conference on **Experimental Fluid Mechanics 2019**, Františkovy lázně, Czech Republic.*

Other activities

PAVLÍČEK, P., HURDA L. LINHART, J.. Výpočet některých re žimů dochlazovacího systému. In Sborník konference 35. SKMTaT, Bratislava, Slovakia: STUBa, 2016.

Presented by L. Hurda in Šamorín, Slovakia.

HURDA, L.. Využití turbulentních LES modelů při CFD výpočtech turbinových stupňů. In CAE FORUM 2016 - Sborník příspěvků. Praha: TechSim Engineering s.r.o., 2016.

Presented by L. Hurda in Benice, Czech Republic.

HURDA, L., MATAS, R.. Liquefied extinguishing agent discharge to an overpressure-sensitive enclosed volume. In MATEC Web Conf. 168, 2018: XXI. International Scientific Conference - The Application of Experimental and Numerical Methods in Fluid Mechanics and Energy 2018 (AEaNMiFMaE-2018). Les Ulis Cedex A: EDP Sciences, 2018. ISSN: 2261-236X. doi:10.1051/matecconf/201816807010.

Presented by L. Hurda in Rajecké Teplice, Slovakia.

HURDA, L. MATAS, R. REDMER, M. Analysis of room overpressure after launching an integrated extinguishing system. Mechanics & Industry 20, 706, 2019. Les Ulis Cedex A: EDP Sciences, 2019. doi:10.1051/meca/2019079.

HURDA, L.., MATAS, R.. Preliminary computational study of turbulent flow in the boundary layer of the suction side of an inclined plate. In EPJ Web Conf. 213, 2019: EFM18 – Experimental Fluid Mechanics 2018. Les Ulis Cedex A: EDP Sciences, 2019. s. 213-218. ISSN 2100-014X. doi:10.1051/epjconf/201921302029.

Presented in a poster section by L. Hurda in Prague, Czech Republic.

The Ph.D. candidate took a course on *Unsteady Simulations for Industrial Flows: LES, DES, hybrid LES/RANS and URANS* taught by Prof. Lars Davidson (November 2017, Göteborg, Sweden).

Appendix A   Velocity field in selected base IGVs cases
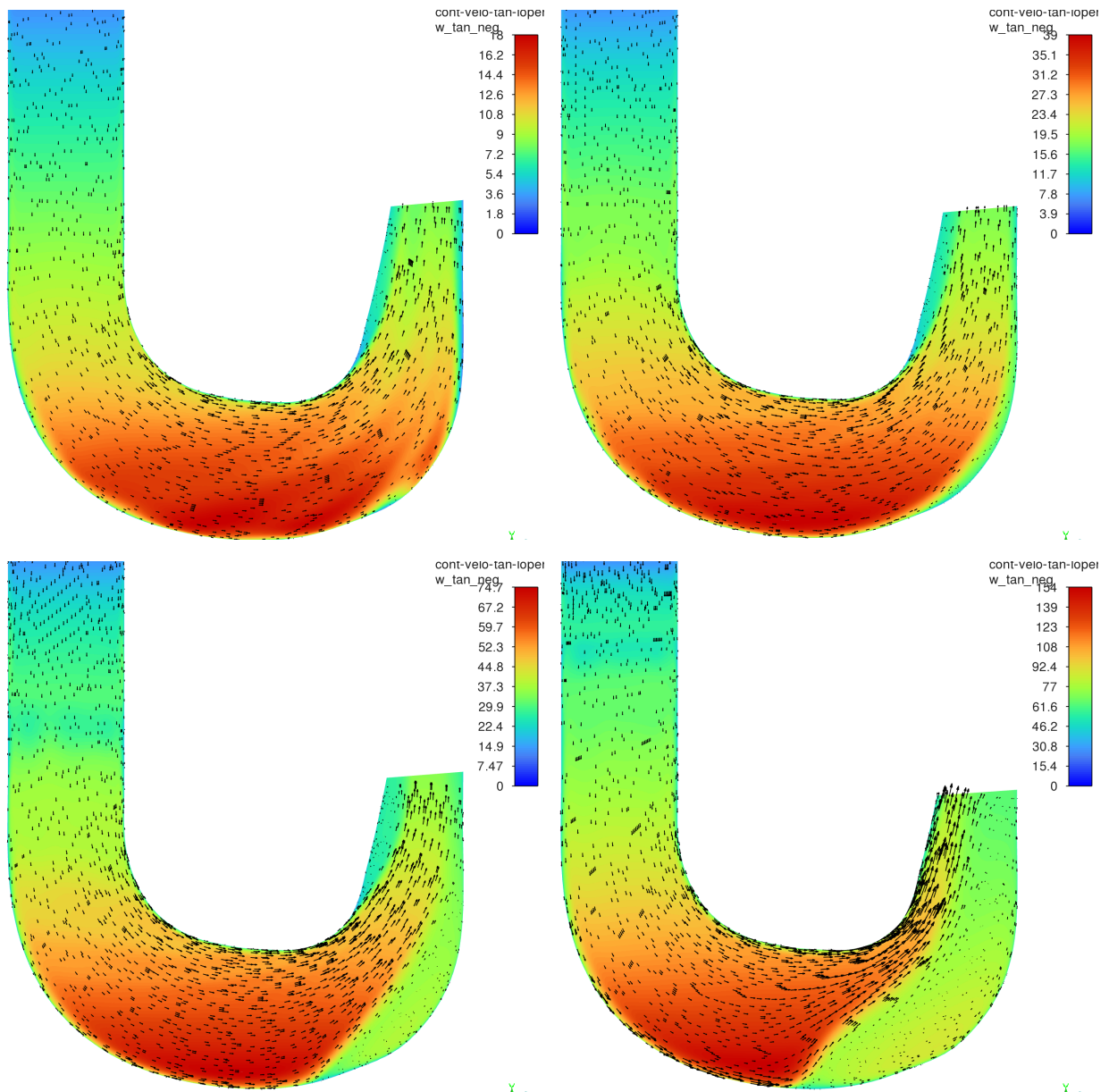
Figure A.1: Axi-radial velocity vectors plus tangential velocity contours. Top left to bottom right: $\vartheta = 15, 30, 45, 60°$.

Appendix B Selected axial velocity contour plots at the periodic boundary surface from the full compressor CFD models

(a) s4IGVs/45/0.55/0.5

(b) s4i60IGVs/45/0.55/0.5

(c) s4IGVs/45/0.85/0.7

(d) s4i60IGVs/45/0.85/0.7

(e) s4IGVs/45/1.00/0.9

(f) s4i60IGVs/45/1.00/0.9
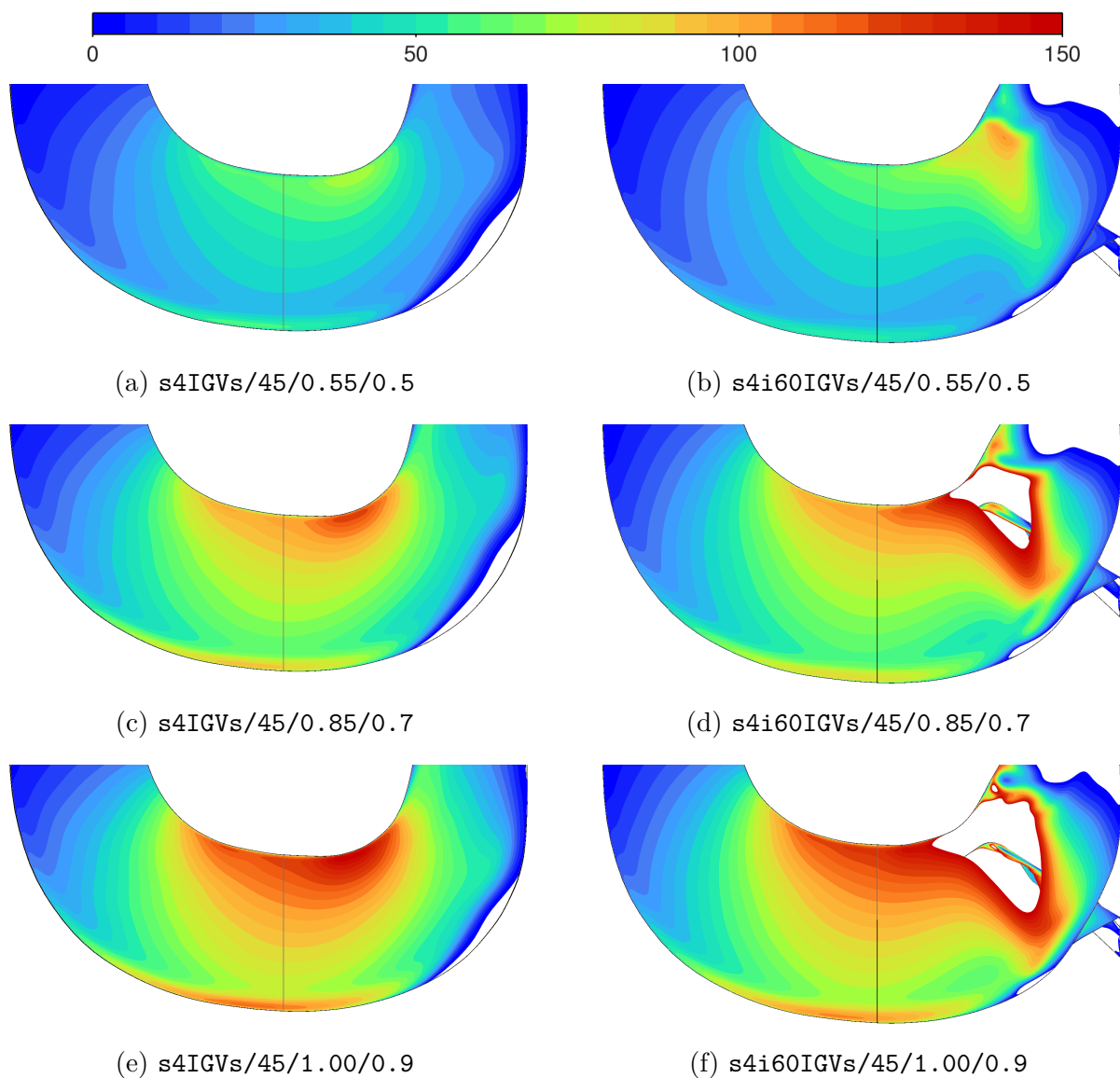
Figure B.1: Axial velocity $[\mathrm{m\,s^{-1}}]$. Comparison of the s4IGVs and s4i60IGVs models at $\vartheta = 45°$.

(a) s4IGVs/60/0.25/0.5

(b) s4i60IGVs/60/0.25/0.5

(c) s4IGVs/60/0.40/0.5

(d) s4i60IGVs/60/0.40/0.5

(e) s4IGVs/60/0.55/0.7

(f) s4i60IGVs/60/0.55/0.7

(g) s4IGVs/60/0.7/0.9

(h) s4i60IGVs/60/0.70/0.9
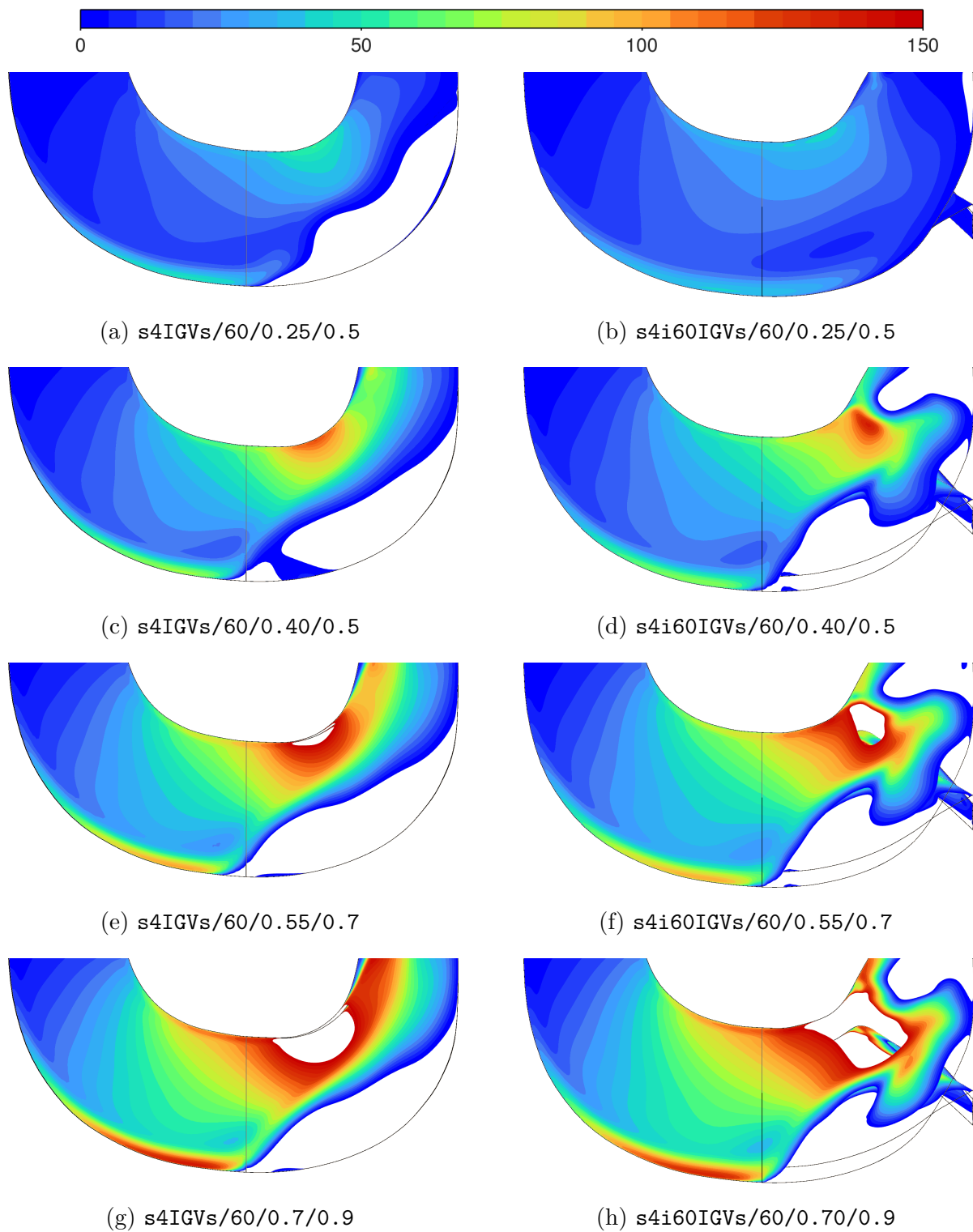
Figure B.2: Axial velocity $[\mathrm{m\,s^{-1}}]$. Comparison of the s4IGVs and s4i60IGVs models at $\vartheta = 60°$.

(a) s4/45/0.70/0.7

(b) s4IGVs/45/0.70/0.7

(c) s4/45/0.85/0.7

(d) s4IGVs/45/0.85/0.7

(e) s4/45/1.00/09

(f) s4IGVs/45/1.00/0.9

(g) s4/60/0.25/0.5

(h) s4IGVs/60/0.25/0.5
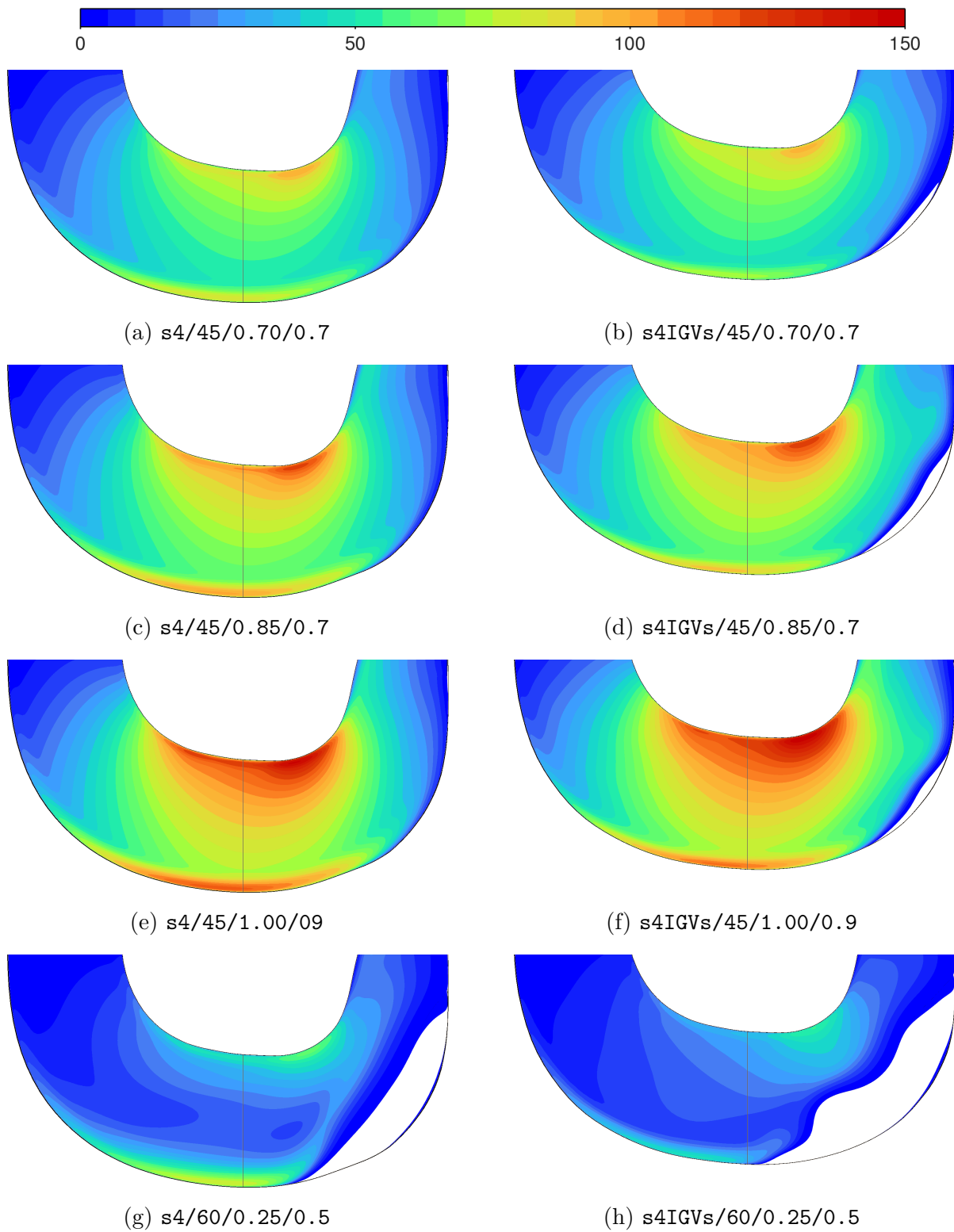
Figure B.3: Axial velocity $[\mathrm{m\,s^{-1}}]$. Comparison of the s4 and s4IGVs models at $\vartheta \in 45, 60°$.